Mechanical modelling of living systems: from cancer modelling to control in sports

by

Meghan Hall

A thesis submitted in partial fulfillment of the requirements for the degree of

Doctor of Philosophy

in

Applied Mathematics

Department of Mathematical and Statistical Sciences
University of Alberta

Abstract

From the mechanical processes that produce the convolutions in the human brain needed for complex thought, to the precise and controlled movements derived by intuitive calculations of body position in figure skating, mechanics plays a role in everything we do. In this thesis, we apply and examine the role of mechanics in models of glioma spread and figure skating.

In Chapter 1, we introduce the topic of glioma modelling and present our glioma spread model in 3D–a continuum model for the density of tumor cells coupled to a general momentum balance equation for the mechanical properties of the glioma and brain tissue. Glioma cells are highly invasive, with the tumors often having diffuse and irregular boundaries. It has been well established that tissue heterogeneity significantly affects glioma spread and tumor cell behavior. Recent work exploring the effects of mechanical properties has strengthened the idea that mechanics plays a large role in determining glioma spread patterns and invasiveness. We focus on modelling two aspects that affect glioma spread: Structural effects on tumor cell migration and the impact of mechanical interactions on tumor spread. The model includes the glioma population as a cell density that can proliferate, spread via fully anisotropic diffusion, and that is advected by the velocity generated by the growing tumor mass. The momentum balance equation determines the deformation caused by the growing tumor mass, with this deformation causing an advection velocity. Not only is this advection velocity coupled to the tumor cells, but it is also applied to material properties, which can include diffusion tensors and elastic-

ity parameters (i.e. shear modulus, bulk modulus). With the exact nature of brain tissue mechanics still being an open question, the form of the momentum balance equation is not specified for the 3D glioma model in Chapter 1, but rather is left in a general form allowing the 3D model to be used a framework for modelling glioma spread which can be used for any description of brain tissue mechanics.

In Chapter 2, we analyze a 1D version of the glioma model to identify, characterize, and simulate travelling waves. Within the 1D model, we consider three biological scenarios representing different stages of glioma development, with each biological scenario characterized by which material properties (elasticity parameters and or diffusion), vary over space and time. In addition to the biological scenarios, we also consider multiple mechanical models, including linear elasticity and the nonlinear one-term Ogden elasticity model, as well as viscoelastic versions of both. For each biological scenario, we compare how these mechanical models affect glioma spread, as well as the resulting deformation and stress. For every mechanical model, we found that travelling waves existed with the same minimal wave speed. However, the deformation and stress associated with each mechanical model differs significantly. The Ogden model results in deformation and stresses two and three orders of magnitude less than the linear model, respectively. We also present wave speed analysis for a generalized elasticity model, finding that the analytically determined wave speed is indeed conserved among such elasticity models.

In Chapter 3, we present a 2D version of the 3D glioma spread model with linear elasticity. We develop and implement a numerical framework for simulating the 2D model, which integrates imaging data for both the simulation

domain and diffusion tensors. We employ ExploreDTI to access and extract imaging data, including diffusion tensors and medical images. Diffusion tensor data is translated to cancer cell diffusion tensors and used to initialize the diffusion tensor in the glioma model simulations. Medical images are processed and used to define the simulation domain. Finally, the model is simulated using a finite element method. Through simulations, we are able to produce simulations with realistic rates of glioma spread and deformation levels. We also explore the effects of the model parameters using simulations. We show that the parameter scaling the body forces significantly affects the rate and shape of glioma spread, making it a desirable target for parameter fitting and further exploration.

Finally, in Chapter 4, we discuss the application of the Chaplygin sleigh as a model for a figure skate. A classical element in the sport of figure skating is reproducing specific patterns on the ice through very detailed, precise control of the skater's movements. We formalize this process using the Chaplygin sleigh as a model of the figure skate, with an added mass representing the skater's moving center of mass and acting as a control parameter for the system. Using a previous result on approximating piecewise curves with arcs, we present a modified form of the Chaplygin sleigh which is limited to producing circular arcs. Finally, we present a control algorithm based on minimization of the energy of control mass which successfully reproduces a prescribed pattern.

Preface

Chapter 2 has been published as Meghan E. Rhodes, Thomas Hillen, Vakhtang Putkaradze, Comparing the effects of linear and one-term Ogden elasticity in a model of glioblastoma invasion. Brain Multiphysics, 2022, 100050, ISSN 2666-5220, https://doi.org/10.1016/j.brain.2022.100050. M.R., T.H., and V.P. developed the model. M.R. carried out the calculations and analysis. M.R. implemented the model in the code and produced the figures. M.R., T.H., and V.P. wrote the manuscript. M.R., T.H., and V.P. read and approved the final manuscript.

Chapter 4 has been published as Meghan Rhodes, Vakhtang Putkaradze, Trajectory tracing in figure skating. Nonlinear Dynamics, 2022, https://doi.org/10.1007/s11071-022-07806-8. M.R. and V.P. carried out the calculations, developed the control procedure, and implemented it in the code. M.R. produced the figures. M.R. and V.P. wrote the manuscript. M.R. and V.P. read and approved the final manuscript.

Acknowledgements

I would like to thank my family for supporting me throughout my education. I cannot thank A.R. enough for his support, encouragement, and for keeping me laughing.

Table of Contents

List of Tables

List of Figures

Chapter 1

Glioma modelling background

1.1 Introduction

In this work, we explore the effects of mechanics on the spread of glioma. We begin by developing a 3-dimensional model of glioma spread which incorporates a data-driven model of cell movement coupled to the influence of the mechanical properties of tissue. Next, in Chapter 2 we limit ourselves to a corresponding 1-dimensional glioma model in order to study existence of travelling wave solutions and examine how the wave speed is affected by model parameters and choice of mechanical model. Building on our understanding of how mechanics affects glioma spread, in Chapter 3 we then present a 2-dimensional model of glioma spread which incorporates patient-specific data for both the simulation domain definition and diffusion tensor initialization.

1.2 Biological components of glioma spread

Before discussing details of mathematical models of glioma spread, we first introduce the core biological components of glioma spread. This discussion is of course limited, with a focus on the factors we will later incorporate into glioma model presented in Section 1.6.

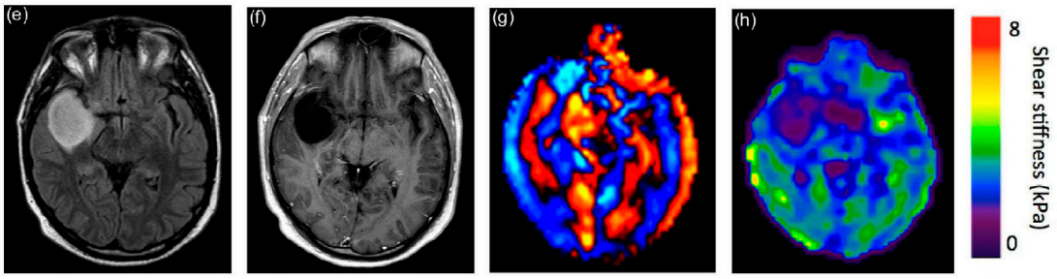

Figure 1.1: MRI and MRE images of glioma. *Left to right:* T2-weighted and; T1-weighted MRI highlighting the tumor and associated edema; MRE wave image; MRE elastogram showing stiffness. Adapted from [53].

Glioma. Gliomas are not homogeneous structures. Typically, a glioma will consist of a solid tumor with tumor cells extending in projections away from the main tumor [43]. The main solid tumor, known as the gross tumor volume (GTV) is also associated with a surrounding region of fluid known as edema [23]. Once the glioma has been well-established, the main tumor develops a necrotic core of cells as nutrients become limited in the center of the growing mass. Surrounding this necrotic core is a layer of proliferating, but largely stationary, cells. Finally, invasive cells are those tumor cells that are more prone to extend from and leave the tumor into the edema and surrounding tissue [127, 114, 43]. The different types of glioma cells can be visualized by employing different imaging techniques, such as T1, T2, and FLAIR (Fluid Attenuated Inversion Recovery), which are used to contrast the different properties (proliferating or dead cells, fluid, etc.) of these tumor regions [114, 91, 53]. Figure 1.1 shows how variations of MRI can enhance different tumor elements.

The main concern with respect to treatment is the diffuse extensions of glioma cells away from the GTV. Due to the low density of the extensions, current imaging techniques are unable to capture them. Uniform 2cm margins, known as the clinical target volume (CTV), around the visible tumor mass are used in treatment planning [23]. A typical example of the GTV and CTV are shown in Figure 1.2. However due to the irregular and diffuse nature of the extensions, the CTV is typically insufficient to capture all of the tumor cells with the remaining tumor cells often leading to further tumors as the leftover cells grow [43]. A further concern with this treatment approach is that

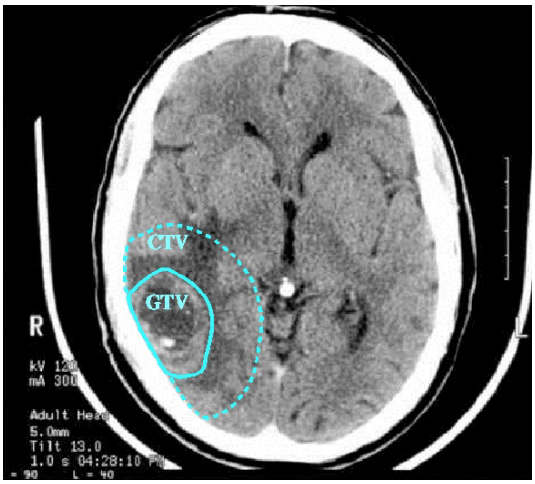

Figure 1.2: Gross tumor volume and associated clinical target volume for a glioma. Adapted from [23].

this CTV unnecessarily treats healthy tissue, worsening the patient outcomes. With a better understanding of the glioma tumor location, even at low tumor cell densities, it may be possible to improve treatment accuracy and hence treatment outcomes.

Brain structure. The brain can be broken down into different regions, structures, and tissue types. We will focus on a few key features that are important in the spread of glioma and the visualization of this spread. There are two main types of tissue that affect the spread of glioma, known as white matter and gray matter [2, 43, 119]. Generally, gray matter is a structurally homogeneous, isotropic material that forms the majority of the brain tissue. White matter fibers are directed tracts of tissue that spread throughout the gray matter. The difference in directionality between white and gray matter lead to differences in how molecules move throughout the brain, with these differences also being reflected in cell movement [43, 95, 91, 18]. The implications of this differential movement between gray and white matter are discussed in Section 1.3.

On a larger scale, the brain can be divided into regions or structures. These regions have varying properties, including different proportions of white and gray matter, as well as different mechanical properties [20, 18]. These differ-

ences in properties between brain structures makes them factors to consider when modelling glioma spread. The largest part of the brain is the cerebrum [2]. The gliomas we will discuss are located within the cerebrum, which is composed of gray matter with white matter tracts spread throughout. The cerebrum is divided into the left and right hemispheres which are connected by the corpus callosum, a relatively rigid, fibrous structure with a high density of white matter [2, 18]. Deep in the brain there are also fluid-filled structures known as the lateral ventricles [2]. Because the lateral ventricles are fluid-filled they are easily deformable, making them useful landmarks to visualize deformation caused by tumor growth. Figure 1.3 shows how the ventricle deformation can be clearly visualized using MRI.

Mass effect. The mechanical interplay of elements within the tumor microenvironment is becoming increasingly recognized as a major factor in determining the patterns of glioma spread [82, 89, 98]. The mechanical effects (pressure, deformation, etc.) of the brain tumor on healthy tissue are known as *mass effect* [91, 28, 114]. Because the skull provides a (mostly) rigid boundary for the brain, restricting movement and growth, the increase in the tumor mass and movement of cells causes pressure, resulting in the healthy tissue to be pushed and compressed. There are extreme cases where brain tumors cause deformation of the skull, but we will limit ourselves to the assumption that the skull remains undeformed. If the mass effect is substantial, it can significantly alter the brain structure and damage healthy tissue. MRIs showing the mass effect are shown in Figure 1.3, with the severity of the mass effect increasing from left to right.

As mass effect is driven by the mechanical forces of pressure and deformation of healthy tissue caused by a growing tumor, including the correct descriptions of mechanics in models of tumor growth is clearly important. The factors that affect how the tumor pushes on healthy tissue and the resulting changes are primarily determined by the mechanical properties of the healthy tissue (brain tissue, skull, etc), and the tumor. In a model of general tumor growth, [73] found that difference in stiffness between healthy tissue and the tumor can affect how the tumor spreads. If the growing tumor encounters

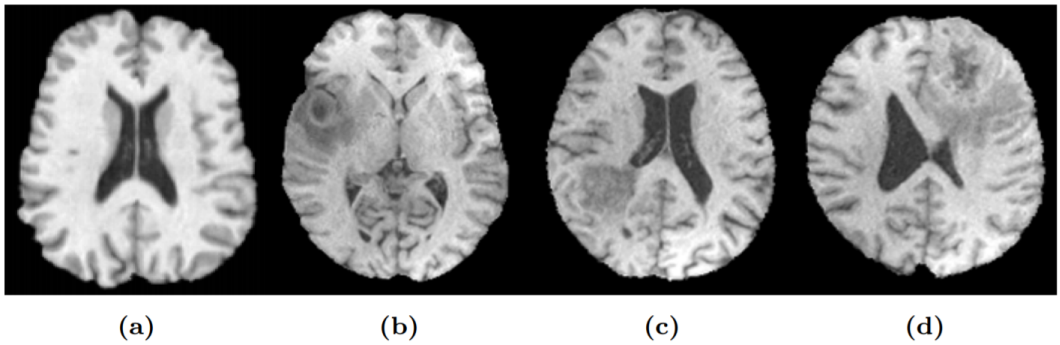

Figure 1.3: MRIs of mass effect caused by glioma. Moving from left to right, the images show an increasing level of deformation caused by mass effect. The effects are most clearly seen by examining the fluid-filled ventricles (in the center of the brain) as they are highly deformable. Adapted from [114].

stiff regions of the brain, it is less likely to be able to expand into that region compared to a softer region. With the relative mechanical properties playing a role in tissue dynamics, a result is that the location of the tumor will impact how and where it spreads which is seen in patients as well. For example, if a tumor originates near the skull, the tumor is not likely to invade or deform the stiff skull boundary but is able to spread in the other direction into the softer brain tissue [91]. Thus, the shape of spread is directed by the mechanical properties of the tumor and environment.

Another mechanical consideration is that as glioma develops, the tumor tissue may change. Reports as to how the tumor tissue evolves is under debate and may be affected by the specific type of tumor [53]. Some studies suggest glioma tissue stiffens with time, while others have found the tumor tissue to soften [53, 113]. Not only has magnetic resonance elastography indicated that necrotic and viable tumor cells vary in level of stiffness [110], but tumor stiffness has also been correlated to grading of glioma [89]. Thus, there is an evolution of the properties of the tumor tissue which likely affects how it interacts with the healthy tissue, and which may also be able to be used in determining disease progression. With these clear mechanical components involved in glioma spread and growth, the addition of mechanical models of the glioma more realistically reflects the reality of mass effects and tissue dynamics. A full discussion of the determination of mechanical properties of

the brain is given in Section 2.1.2.

1.3 Data and model validation

With the brain being a highly sensitive, critical organ, data collection related to the brain and glioma is a difficult process. With direct analysis, such as biopsies, etc, ruled out by being highly invasive, imaging is the main tool used during glioma diagnosis and treatment. MRI can be used to identify the central tumor, edema, and many structures in the brain [53, 28, 15, 91, 116]. Variations on MRI can be used to highlight certain structures, with particular versions highlighting fluid, proliferating cells, among others [15, 91].

A relatively recent advance in medical imaging is an MRI-based technique known as Magnetic Resonance Elastography (MRE) is able to test the mechanical properties of brain tissue and glioma *in vivo* [53]. MRE involves generating shear waves in the brain, either through external movement or by applying a focused-ultrasound-based (FUS-based) radiation force [53, 75]. MR images of the propagation of the shear waves are recorded and the images processed to produce images of tissue stiffness, as shown in Figure 1.1.

Using this technique, the mechanical parameters of *in vivo* tissue can be estimated. As this method does not require the removal of brain tissue, many of the downfalls associated with *ex vivo* testing are avoided with MRE. A further notable benefit with MRE being an *in vivo* imaging technique is that it has the possibility of providing patient-specific data. Theoretically, MRE could be used for each patient, their mechanical parameters estimated, and these parameters used to parameterize a patient-specific mechanical glioma model. Although MRE data is not used directly in this work, we do utilize particular insights into the mechanical properties of brain tissue and developing gliomas determined by MRE. We suggest that MRE is a largely unused source of data for future glioma models, which should be taken advantage of in future glioma modelling efforts.

Glioma imaging data. Both the sensitive location and the aggressiveness of glioma mean that data collection is restricted. The fast pace of glioma

progression is a hindrance as the short timespan from diagnosis to death limits the number of times data can be collected. Typically, each patient will only be imaged one or two times. Also limiting the number of temporal data points are the usual considerations of accessibility. Each scan not only requires the patient to be available, but also the resources required to carry out the test, both factors contributing to limited data being acquired. Thus, the number of time points is very limited in the available data.

Perhaps the biggest limitation in collecting glioma data is the anatomical location of interest. Because the brain cannot be easily and freely probed, the data collected on glioma is mainly limited to imaging techniques. Given its non-invasive nature, these imaging techniques are typically based on MRI. The basic forms of MRI can be used in various ways in glioma modelling.

First, an MRI can be used to specify a domain for the glioma model [116, 15, 28]. Most glioma models use a spatial domain meant to represent a human brain with the boundary being the skull. This involves specifying a brain domain that includes major structures of the brain, such as the corpus callosum, ventricles, etc. Typically this domain is based on an MRI of the brain which is then segmented, either manually or automatically, into regions for each of the major structures [116, 28, 54, 114]. The structures are then assigned mechanical properties and boundary conditions. For example, the skull is typically assumed to be static with tissue unable to deform or pass through the skull, while the fluid-filled ventricles are taken to be easily deformable [54, 114, 28, 15]. Following the specification of an initial brain domain and glioma density, a glioma model can then be solved on this domain in order to determine the evolution of both the tumor and its impact on the brain.

Second, a sequence of MRIs of a tumor can be used to give estimates of parameters such as growth rate and motility [119, 28]. By tracking the volume change of the tumor, certain models use this to derive an estimate for the proliferation rate of a tumor.

Third, the initial tumor density can be estimated form MRI data [116, 114, 28]. Either through manual or automatic tumor segmentation, the initial (visible) tumor region can be identified on an MRI image and used as the initial condition of the tumor cell density.

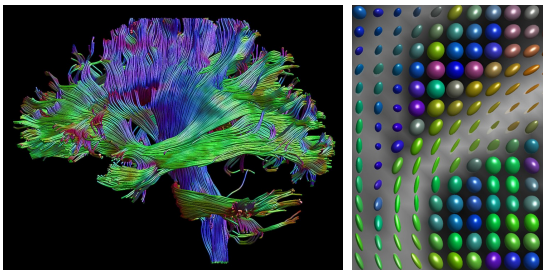

Figure 1.4: Visual representations of DTI data. *Left*: DTI showing white matter tracts. *Right*: Diffusion MRI tensors represented as ellipsoids. Color indicates principal direction of movement. Shape indicates level of anisotropy. Images from exploredti.com.

Finally, MR images are often used to compare model simulations to reality. The size and shape of the tumor can be compared, qualitatively or quantitatively, between simulated and real images [116, 28, 15]. When comparing model results to real patients quantitatively, a previously employed method is to calculate a Jaccard score which measures the amount of overlap between the modeled tumor and patient data [116, 83].

DTI data. Diffusion tensor imaging is a variation of MRI that tracks the diffusion of water molecules. Details of the physical basis of DTI are given in [67, 69, 3] and will not be discussed in depth here. In brief, water molecule dipoles are polarized and the water diffuses with this diffusion tracked using imaging. DTI is used to locate white matter fibers using the idea that there is higher diffusion in the directions parallel to white matter fibers. That is, areas with higher diffusivity indicate the presence of white matter. Figure 1.4 is a DT image clearly showing white matter fibers. DTI yields measurements for both rate and direction of movement for a certain spatial region (or voxel). These rates and directions of movement are then used to specify diffusion tensors. An illustration of tensors resulting from DTI is shown in figure 1.4. Thus, DTI data yields a "diffusion tensor map", with each 3D voxel in the domain having an associated diffusion tensor. The tensors can be visualized as ellipsoids where it has been observed that glioma cells also tend to travel along white matter fibers [43, 91]. Exploiting this observation, DTI data has been used in previous glioma models and has been shown to increase the accuracy of these models in

predicting tumor volume in systems with significant anisotropy [116, 55, 28]. However, it should be noted that the diffusion tensors obtained from DTI are based on water diffusion, not tumor cell diffusion. This means that a transformation of the DTI data from water diffusion to tumor cells diffusion should be applied before using the data in mathematical models. Methods for translating the DTI data to a cancer diffusion tensor vary in complexity, from a simple constant scaling of the data as in [28, 15, 63], to highly detailed methods based on cellular behavior [87, 116].

Although there is currently no consensus on how this data transformation should be carried out, the most common method is to employ a measure of anisotropy known as a diffusion anisotropy index (DAI). A DAI reflects the amount of anisotropy for a given tensor. The amount of anisotropy can be viewed as how spherical a diffusion ellipsoid is, with less spherical meaning a higher level of anisotropy. There are multiple forms of DAI which are detailed in [60], but we will limit our discussion to fractional anisotropy (FA) which we will use in Chapter 3.

FA can be determined from the eigenvalues of the diffusion tensor using the formula

$$\mathrm{FA} = \sqrt{\frac{3[(\lambda_1 - \bar{\lambda})^2 + (\lambda_2 - \bar{\lambda})^2 + (\lambda_3 - \bar{\lambda})^2]}{2(\lambda_1^2 + \lambda_2^2 + \lambda_3^2)}}, \tag{1.1}$$

where $\lambda_1, \lambda_2, \lambda_3$ are the principal values of the tensor, and $\bar{\lambda} = (\lambda_1 + \lambda_2 + \lambda_3)/3$ is the mean of the eigenvalues. The values of FA range from zero, representing isotropic diffusion, to 1, representing fully anisotropic diffusion. As FA only gives a measure of the amount of anisotropy, it is only a part of determining the diffusion tensor used in the model. The directionality and relative measure of tumor cell diffusion vs. water diffusion must also be considered. Mosayebi *et al.* [83] employed a scaling of FA, introducing a scaling factor to account for the difference in diffusion rates between tumor cells and water, and using the original DTI data to include the directionality of diffusion:

$$D(x) = \alpha \mathrm{FA(x)DT(x)} \tag{1.2}$$

where α is the scaling factor and DT is the tensor taken directly from the DTI data. This method gives the greatest diffusion along the main eigenvector of DT (i.e., in the direction of white matter fibers), accelerates diffusion along fibers, and maintains tensor shape.

Another method of translating DTI data into tumor cell diffusion rates was introduced in [87], and later used in [116]. In this method, the second moment of a turning distribution is used for the tumor cell diffusion tensor. In 3D, the turning distribution is taken to be a Fisher distribution with the distribution properties derived from the DTI data. The Fisher distribution takes the form

$$q(\boldsymbol{n}) = \frac{k}{8\pi \sinh(k)}(e^{k\boldsymbol{n}\cdot\boldsymbol{\gamma}} + e^{-k\boldsymbol{n}\cdot\boldsymbol{\gamma}}), \tag{1.3}$$

where $\boldsymbol{\gamma}$ is the dominant unit eigenvector taken from the DTI tensor. The presence of exponential terms with both positive and negative exponents results from the assumptions that travel in either direction of the main eigenvector, ie. up or down a white matter fiber, is equally likely. Thus, terms with both the $\boldsymbol{\gamma}$ and $-\boldsymbol{\gamma}$ direction must be included.

For each voxel's diffusion tensor, the peaks of the Fisher distribution are aligned to the principal eigenvector of the tensor. The height of the peaks of the Fisher Distribution which represent the level of anisotropy are determined by a concentration parameter, k, that is proportional to the fractional anisotropy of the tensor data. Thus, the concentration parameter is given by

$$k(x) = \kappa FA(x), \tag{1.4}$$

where κ is an anisotropy parameter. This concentration parameter $k(x)$ determines the width of the distribution, with higher values giving a sharper peak. By making $k(x)$ proportional to FA, areas with higher anisotropy are associated with Fisher distributions with sharper peaks. Thus, this relationship between k and FA preserves the levels of anisotropy during the translation between DTI data to tumor cells diffusion tensors.

The final translation from DTI data to tumor cell diffusion tensor is then

given by

$$D_c(\boldsymbol{x}) = \frac{1}{\mu} \int_V \boldsymbol{v}\boldsymbol{v}^T \boldsymbol{q}(\boldsymbol{x}, \boldsymbol{v}, k)\ dv, \tag{1.5}$$

where μ is a turning rate, $\boldsymbol{v}$ is the velocity, and $\boldsymbol{q}$ is the turning distribution. The benefit to this diffusion tensor translation method is that it introduces the parameters μ and κ which can be fit to an individual patient (see [116]). A 2D version of this translation is used in Chapter 3.

Data sources and processing. There are two commonly used sources for defining both the initial spatial domain and DTI maps of the brain. The first is a brain atlas [32, 28, 15]. An atlas represents a typical or average brain and is essentially a composite of many individual brains. Thus, an atlas is a reasonably realistic brain domain and DTI map, but does not represent a particular real brain and is not patient-specific [32, 28, 15]. The second commonly used data source is based on a particular patient's brain images. In this case, the initial brain domain and DTI map are taken directly from a single patient [116, 83]. The patient-specific data allows for direct comparison and validation of model results to the real patient [116, 83]. A useful table detailing the data sources used in previous glioma model studies is given in [116].

It should be noted that MRI and DTI data is pre-processed before being used in modelling. Pre-processing, including image registration, segmentation, filtering, etc., will not be explored further here. For information on and examples of the processing, usage, and integration of medical imaging into models of glioma, [44, 28, 111] are suggested references.

1.4 Mechanics

A large part of this thesis is devoted to mechanics. In particular, in Chapters 2 and 3 we explore how mechanics affects the dynamics of a model of glioma spread. Thus, we will now present a brief discussion of the key elements of mechanics that will be used later.

Reference frames. When using continuum mechanics, it is critical to keep track of which spatial frame of reference the equations are set in. The first consideration is the choice between spatial (Eulerian) coordinates or body (Lagrangian, material) coordinates. Each coordinate frame comes with an associated set of measures, derivatives, etc. The spatial coordinates are how an external observer would view the deformations and dynamics, while the body coordinates are how the body moves if viewed from/on the body. The context and components of the continuum problem determine the appropriate frame, with certain calculations arising more naturally in a particular coordinate system depending on the problem. A translation between the two frames is available so that the mathematics can be carried out in the preferred frame, with the results then translated to the other frame if necessary.

A simple illustration of the difference between spatial and body frames is a person walking in a bus. If we want to determine the change in location of this person, the spatial and body frames must account for different components of this movement. Consider a moving bus and walking along this bus, with the bus and its contents being the "body". Consider the problem of determining how far the person walks on the bus. The spatial frame would need to account for both the movement of the bus and also the movement of the person walking inside. The body frame would only consider the movement of the person since the movement is occurring on/in the body, making this problem simpler in body coordinates.

As glioma is a problem occurring in spatial coordinates where the data (MRI, DTI) comes from spatial coordinates, at the very least, the *results* of a glioma model should be in the spatial frame. However, it may be easier or more useful to model the tumor in the body frame as this often simplifies the mathematics, and then translate this back to the spatial frame. However, many models opt to work in the spatial frame throughout, avoiding the conversion from body to spatial coordinates. Following the lead of previous glioma modelling work, we will work purely in the spatial frame.

Deformation and displacement. The deformation/displacement defines how the tumor cell density and surrounding brain tissue deforms, making it a

very important factor when modelling the mechanics involved in tumor spread. Among the models discussed here, there are differences in both the form of the deformation gradient as well as the method of deriving the deformation gradient.

In models where mechanics is included by coupling a momentum conservation equation to a reaction-diffusion equation (for example [54, 114]), the deformation is derived by solving a momentum balance equation for the displacement. The momentum balance equation is derived by choosing a suitable equation for the stress tensor, which defines the type of elasticity of the tissue, as well as an equation for the external body forces which governs the impact of tumor cell presence.

In the other main class of models where the tumor volume only evolves according to some prescribed growth and the mechanical properties of the tissue, the deformation is often decomposed [4, 6, 5, 124, 112]. The deformation is represented by the deformation gradient, which is decomposed into an active component–representing the volume increase resulting from tumor proliferation–and a passive component–representing the elastic response that pushes back on the tumor after the growth phase. In this case, the growth component is typically prescribed to expand following a certain shape–typically isotropic/spherical–at a given rate which may or may not be fit to data. The elastic component of the deformation gradient is then derived by solving the momentum conservation equation. As this method relies on prescribing the effect of growth on deformation, this may be more useful if this aspect of tumor growth is well known and the main question is the mechanical response to, or affect on, this growth.

Constitutive models. The elasticity and mechanical properties of biological tissues are typically modeled using constitutive models. Different constitutive models encompass a variety of mechanical properties. The desired constitutive models are chosen to reflect the particular mechanical nature of the material, such as linearity of the elastic response, shear modulus, bulk modulus, and type of elasticity (viscoelastic, hyperelastic, etc.). Matching appropriate constitutive models to materials is typically carried out by sub-

jecting the material in question to mechanical testing, fitting candidate constitutive models, and determining the optimal model based on fit accuracy (see [80, 79, 20, 21, 18]).

A discussion of the constitutive models examined in the context of brain tissue is given in Section 2.1.2. Currently, there is no standard constitutive model used to model brain tissue and brain tumors. A summary of the constitutive models used in previous literature is shown in Table 1.1.

In Chapter 2 we consider the commonly used linear elasticity as well as the experimentally determined one-term Ogden elasticity. We also explore viscoelastic versions of these models. In Chapter 3, we employ linear elasticity.

Coupling mechanical and cell density models. Although this discussion focuses on mechanical modelling of glioma, it should be noted that the majority of glioma models couple the mechanical component with a reaction-diffusion model. Some of the first mathematical models of glioma were purely reaction-diffusion models [121, 22, 126, 29]. The diffusion represents the infiltration of the cancer cells, while the reaction term represents the proliferation of the tumor cells.

A mechanical model can be coupled to a reaction-diffusion equation, thus modelling the cellular dynamics and mechanical dynamics, and the connections between them. This connection typically introduces an advection term as the pressure from the mechanical system pushes the tissue. Growth of the tumor results in deformation, with this deformation likely affecting the subsequent spread and growth of the tumor.

Simpler early models had only one sided coupling between the mechanics and the diffusion equation [28]. In [28], the tumor proliferation causes a mass effect, but the mass effects did not feed back into the cell density evolution. Later models fully coupled the mechanical and diffusion equations so that the pressure created by the tumor proliferation affects pushes on the tissue and feeds back into the diffusion equation [54, 114].

Pressure terms. The mathematical representation of the pressures resulting from tumor growth are generally based on either Darcy's Law or a phe-

Table 1.1: Mathematical models of brain tissue used in rheological studies and glioma models.

Reference	Constitutive model(s) used
Rheological studies	
Mihai [80]	Neo-Hookean, Mooney-Rivlin, Fung, Gent, Ogden
Mihai [79]	Ogden (multiple forms)
Budday [18]	Neo-Hookean, Mooney-Rivlin, Demiray, Gent, One-term Ogden
Budday [20]	Ogden (multiple forms)
Budday [21]	Viscoelastic Ogden
Brain (tumor) models	
Kyriacou [66]	Neo-Hookean
Clatz [28]	Linear (no bulk modulus term)
Bondiau [15]	Linear (no bulk modulus term)
Hogea [54]	Linear
Angeli [6]	Neo-Hokean
Abler [1]	Linear
Subramanian [114]	Linear
Rhodes	Linear, Linear Viscoelastic, Incompressible Linear, One-term Ogden, Viscoelastic One-term Ogden

nomenological description. The method of incorporating the pressure terms is not chosen in isolation, but rather is influenced by the choice of either a mixture model vs. a continuum model. In mixture models where cells are represented as an incompressible fluid in a porous media, Darcy's law is used to model the physical interactions of the cells. When viewing cells as an incompressible fluid in a porous media, the choice of Darcy's law is a reasonable one as this is the classic model used for porous media. Examples of the use of Darcy's law to incorporate pressure into glioma and/or tumor models are [73, 6, 124].

In continuum models, the phases are not represented explicitly but rather the cells are seen as part of a tissue, where the elastic properties can be seen as implicitly representing the interplay between the solid and liquid phases. As the body forces are phenomenological, the specific forms vary among models. One example can be found in [54] where the pressure-like forces take the form of an exponential term dependent on the tumor cell density, scaled by the gradient of the tumor cell density. In later work building on the Hogea model, Subramanian *et al.* used a pressure term that replaced the exponential term with a hyperbolic tangent function of the cell density [114]. The specific forms of the body force function used in [54] and [114] are given in Section 2.2 and Section 3.2. Of note is that both models have similar characteristics. First, in the absence of tumor cells, there is no force. Secondly, the first component of the force (the exponential or hyperbolic tangent element) is maximized at the carrying capacity of the tumor (i.e., when $c(x,t) = 1$). Third, by including a scaling by the gradient of cancer cells, the force is proportional to differences in cancer density. Lastly, both models also have a parameter scaling the total body force. The larger this scaling is, the more significantly the presence of tumor cells deforms the surrounding tissue. As discussed in Chapter 3, the choice of this parameter is unclear.

We employ the exponential force model from [54] for the travelling wave analysis (see Chapter 2). However, a benefit of the hyperbolic tangent form from [114] is that it is defined at zero cell density, where the exponential model used by [54] is undefined and the limit value must be used. In Chapter 2, this causes minimal issues. However, when simulating the 2D model numerically

(see Chapter 3), the pressure term value at zero cell density became problematic, requiring the hyperbolic tangent form to be used.

1.5 Previous glioma models

For an overview of the previous work in glioma spread modelling, see Section 2.1.1. In addition to that overview, we discuss three of the models mentioned in Section 2.1.1 that are the most significant to the current work in further detail.

Swanson *et al.* 2000. Initial mathematical models of glioma considered the tumor as a cell density, where the tumor density could spread and proliferate [121, 126]. The core description of tumor cell proliferation and movement took the form of reaction-diffusion equations given by

$$c_t(\mathbf{x}, t) = D\nabla^2 c(\mathbf{x}, t) + \rho c(\mathbf{x}, t)\,, \tag{1.6}$$

where $\mathbf{x}$ is space, t is time, c is the tumor cell density, D is the diffusion coefficient, ρ is the proliferation rate. Other additions to this core model such as mutation and treatment effects were also included by [121, 126]. The spread of glioma cells were modelled by a Laplacian diffusion term with spatially dependent diffusion, while proliferation and treatment effects were included via exponential reaction terms. Examples of these models are [22, 29, 121, 126]. The boundary conditions were taken to be no flux, modelling the natural barrier of the skull. Variations on this core model were explored by considering different treatment models and cell types.

In 2000, a landmark paper from Swanson *et al.* [119] modified these initial models by considering a spatially heterogeneous diffusion coefficient. This model is termed the *Proliferation-Infiltration* (PI) model, referencing the two terms of the model, with the reaction and diffusion terms being representing the proliferation and migration of tumor cells, respectively. Here, the diffusion coefficient is allowed to vary in space, representing the differential diffusion

rates of cells in white vs. gray matter. The cell density is modelled in [119] as

$$c_t(\mathbf{x}, t) = \nabla \cdot (D(\mathbf{x})\nabla c(\mathbf{x}, t)) + \rho c(\mathbf{x}, t)\,, \tag{1.7}$$

with the diffusion coefficient given by

$$D(\mathbf{x}) = \begin{cases} D_g & \mathbf{x} \in \text{gray matter}, \\ D_w & \mathbf{x} \in \text{white matter}, \end{cases} \tag{1.8}$$

where $D_w = 5D_g$. The choice of a five-fold difference in diffusion rates was calculated in [119] from experimentally observed velocities from serial CT scans (as previously discussed in [121]) and assuming Fisher's approximation, which gives that $D \approx v^2/4\rho$.

In [119], they used this model to simulate tumors in three different locations with the underlying domain and locations of gray and white matter taken from an on-line database. They also considered the intrinsic properties of a growing glioma, varying the values of ρ and D to represent different grades of glioma. With a focus on detection, [119] found that the ratio ρ/D determined how accurately the boundaries of a tumor could be detected by medical imaging, with larger values corresponding to more accurate detection.

Swan *et al.* 2018. Building on the PI model, Swan *et al.* [116] modified the structure of both the diffusion and proliferation terms. Swan *et al.* also incorporated patient-specific data for both the simulation domain and diffusion coefficient. The model from [116] is as follows:

$$c_t(\mathbf{x}, t) = \nabla\nabla : (\mathbf{D}(\mathbf{x})c(\mathbf{x}, t)) + \rho c(\mathbf{x}, t)(1 - c(\mathbf{x}, t))\,. \tag{1.9}$$

The fully anisotropic diffusion term models tumor cell migration more realistically as it is derived from a mesoscopic description of cell movement along fibers [87], rather than assuming random movement as in Fickian diffusion. Furthermore, [87] showed that the derivation of the anisotropic diffusion model includes a method for the scaling of water diffusion tensors to cell diffusion tensors and introduces patient-specific parameters to match this scaling to each

patient's medical imaging data. Unlike Fickian diffusion, fully anisotropic diffusion applies two spatial derivatives to both the diffusion constant and the density. The notation $\nabla\nabla :$ is not to be confused with Δ or ∇^2 as it implies a double contraction with two derivatives:

$$c_t = \nabla\nabla : (Dc) = \sum_{i,j} \frac{\partial}{\partial_i} \frac{\partial}{\partial_j} (D_{ij} c) \,. \tag{1.10}$$

The diffusion tensor in [116] incorporates patient-specific DTI data. Unlike the discrete delineation of white and gray matter diffusion coefficients used in [119], the diffusion tensor in [116] is taken directly from the DTI data and translated using the scaling parameters mentioned above, resulting in a more continuous (although still technically discrete, as necessitated by the data) version of the diffusion coefficient/tensor.

The inclusion of a logistic growth term more accurately models the growth of a glioma than the exponential model. In contrast to the logistic model, the exponential growth model assumes there are no limiting resources for the growing tumor. In reality, gliomas typically experience blood flow and oxygen depletion limiting the growth of the tumor, making the logistic growth model a more appropriate choice in this context.

Crucially, [116] applied this anisotropic model to real patient data for 10 patients and compared the results to parallel simulations using the PI model. In [116], it was found that for tumors with high levels of anisotropy, the anisotropic diffusion term was better able to capture the irregular shapes of gliomas than the isotropic diffusion term in the PI model.

Hogea *et al.* 2008. The final glioma modelling work with a direct impact on the work in this thesis is that from Hogea *et al.* [54]. The most significant contribution from [54], in regards to the current work, is the connection of the cell density equation to an equation representing the mass effect. Hogea *et al.* included the mass effect by coupling a momentum balance equation to the mass balance equation for glioma cells through an advection velocity. The equations coupling cell evolution and tissue mechanics provides a framework to study the interplay between brain tissue mechanics and glioma spread, as

is explored in later sections. Unlike Swan *et al.* [116], Hogea maintain the Fickian diffusion term, as well as the discrete diffusion coefficient used by Swanson *et al.* [119], although they did include logistic growth. The model used in Hogea *et al.* is as follows. Space is denoted by x, time by t, spatial domain by Ω, and the time domain by $(0, T)$. The model variables include cell density, c, deformation, u, velocity, v, as well as the vector $\mathbf{m} = (D, \lambda, \mu)$, which includes the elastic material properties and diffusion coefficient. For $\mathbf{x} \in \Omega$ and $t \in (0, T)$

$$c_t(\mathbf{x}, t) - \nabla \cdot (D(\mathbf{x}, t)\nabla c(\mathbf{x}, t)) + \nabla \cdot (c(\mathbf{x}, t)\mathbf{v}(\mathbf{x}, t)) - \rho c(\mathbf{x}, t)(1 - c(\mathbf{x}, t)) = 0 \tag{1.11}$$

$$\nabla \cdot ((\lambda \nabla \cdot \mathbf{u}(\mathbf{x}, t)) + \mu(\nabla \mathbf{u}(\mathbf{x}, t) + \nabla \mathbf{u}(\mathbf{x}, t)^T)) - f(c(\mathbf{x}, t), \mathbf{p})\nabla c(\mathbf{x}, t) = 0 \tag{1.12}$$

$$\mathbf{v}(\mathbf{x}, t) = \mathbf{u}_t(\mathbf{x}, t) \tag{1.13}$$

$$\mathbf{m}_t(\mathbf{x}, t) + \nabla \mathbf{m}(\mathbf{x}, t)\mathbf{v}(\mathbf{x}, t) = \mathbf{0}\,, \tag{1.14}$$

where ρ is the tumor cell proliferation rate. The function f is a phenomenological expression that represents the forces created by the presence of tumor cells and is given by

$$f(c) = p_1 e^{-p_2/c(\mathbf{x},t)^s} e^{-p_2/(2-c(\mathbf{x},t))^s}\,, \tag{1.15}$$

where $\mathbf{p} = (p_1, p_2, s)$ is a parameter vector determining the strength and range of influence of the tumor cells. A more detailed explanation of this function is given in Section 2.2.

The momentum balance equation uses linearly elasticity to represent the mechanics of brain tissue. Linear elasticity is a commonly used constitutive model to represent brain tissue as it is tractable, but studies have suggested that it is too simplistic to accurately capture some of the more unique properties of biological tissues.

The boundary conditions are given by

$$\frac{\partial c(\mathbf{x},t)}{\partial \mathbf{n}} = 0 \qquad \text{on } \partial\Omega \times (0,T)\,, \tag{1.16}$$

$$\mathbf{u}(\mathbf{x},t) = 0 \qquad \text{on } \partial\Omega \times (0,T)\,, \tag{1.17}$$

which implies that

$$\mathbf{v}(\mathbf{x},t) = 0 \qquad \text{on } \partial\Omega \times (0,T)\,. \tag{1.18}$$

The initial conditions are

$$c(\mathbf{x},t=0) = c_0(\mathbf{x}) \qquad \text{prescribed on } \Omega\,, \tag{1.19}$$

$$\mathbf{u}(\mathbf{x},t=0) = 0, \mathbf{v}(\mathbf{x},t=0) = 0 \qquad \text{on } \Omega\,, \tag{1.20}$$

$$\mathbf{m} = (D,\lambda,\mu)(\mathbf{x},t=0) = \begin{cases} (D_w,\lambda_w,\mu_w)\,, & \mathbf{x} \text{ in white matter,} \\ (D_g,\lambda_g,\mu_g)\,, & \mathbf{x} \text{ in grey matter,} \\ (D_v,\lambda_v,\mu_v)\,, & \mathbf{x} \text{ in ventricles.} \end{cases} \tag{1.21}$$

The boundary conditions are from the assumption of no-flux of tumor cells and no displacement of the skull. The initial condition for $\mathbf{m}$ is determined by a segmented MRI. The material properties are taken to be heterogeneous, but still isotropic within each region.

With this model, [54] successfully produced simulations and determined a method to estimate parameters from patient data. In [114], Subramanian *et al.* expanded on [54] by including multiple species (including proliferating cells, invasive cells, necrotic cells) as well as nutrients. As discussed in Section 1.5, [114] also altered the body force function which we use in Chapter 3 as it provided more numerical stability than the previous version from [54]. Subramanian *et al.* [114] also presented simulations of glioma spread which were able to reproduce the characteristic projections of glioma and deformation of the ventricles.

Brief discussion of advection velocites. The modelling of the mechanics during glioma spread may or may not include the formation of an advection

velocity. As the tumor volume increases, a deformation of the tissue is formed which then leads to a displacement-associated velocity. We will refer to this velocity as an advection velocity. In simpler models, the tissue properties are kept static [28, 15, 55]. That is, the material is constant in time and not affected by the growing tumor or resulting advection velocity. In this case, the tumor grows and creates a deformation, but this deformation only affects the growth of the tumor, while the healthy tissue brain properties are unaffected. In such examples, the elastic nature of the brain was implemented through a momentum balance equation, but no advection velocity was included [28, 15].

In more complex models, the properties of the healthy brain tissue, such as diffusion and mechanical properties, are advected with the advection velocity derived from the deformation caused by the growing tumor [54, 114]. This process models how the material properties move with the underlying tissue that is being deformed by the growing tumor. As glioma is known to deform the surrounding healthy tissue, including this material property advection would seem to be a more realistic concept than holding the material properties constant. Hogea *et al.* [54] were one of the first groups to include the effects of deformation and advection on the brain properties and glioma cell movement. This is included by first calculating the displacement caused by the presence of tumor cells (via a momentum conservation equation), determining the advection velocity (by taking the time derivative of the displacement), with this velocity then applied to the diffusion coefficient map and the mechanical parameters of the brain by solving an advection equation for these properties (see equation 1.14 in the Section 1.5).

It should be noted that the form of advection used by [54] is a non-conservative, or scalar, advection. In later work extending [54], Subramanian *et al.* [114] changed the definition of the "material parameters", instead defining them based on tissue composition (tumor, white matter, gray matter). As in [54], these properties were advected. However, the advection operator used in [114] was a conservative form given by

$$\mathbf{m}_t(\mathbf{x}, t) + \nabla \cdot (\mathbf{m}(\mathbf{x}, t)\mathbf{v}(\mathbf{x}, t)) = \mathbf{0}\,. \tag{1.22}$$

As implied by the name, conservative advection conserves the advected quantity as a density. Thus, as the quantity is advected, it can become more or less concentrated. On the other hand, with the scalar advection given by equation (1.14), the quantity remains the same density, only being displaced by the advection. This is an important difference with respect to modelling the evolution of diffusion and elasticity properties. If one considers the physical nature of the elastic properties of structures in the brain, it is unlikely that they would move in a conservative fashion. The elastic properties modelled in [54] and [114] are associated with physical structures in the brain, such as the ventricles. The ventricles are much less stiff than the surrounding brain tissue and are often deformed in glioma cases. But, it is unlikely that the stiffness and viscosity of the ventricles is concentrated during this deformation. Thus, for the elasticity properties involved, it would seem that the non-conservative advection of (1.14) is likely the more realistic choice. However, when we consider advection of the diffusion tensors, conservative advection (see equation 1.22) may be more plausible. As mentioned previously, diffusion follows structures in the brain such as white matter fibers [91]. It could be reasoned that white matter fibers could be deformed and pushed together, increasing the density of white matter. With this increasing density of white matter, there could be an associated increase in diffusivity, which would be represented in the diffusion tensor. Therefore, it is not unreasonable to consider a conservative advection for the diffusion tensor.

Applications to current work. The model(s) developed and used in this work are based on the model from [54] with modifications made to certain elements.

- *Growth*: We keep the logistic growth reaction term used by [54] rather than the exponential form used in earlier work [119].
- *Diffusion operator*: With the promising results of [116], we include fully anisotropic diffusion in place of the Fickian form.
- *Advection operator*: In the majority of the work presented here, we follow [54] and assume non-conservative advection of both diffusion and elas-

ticity properties. However, in Chapter 2, we also consider conservative advection in some of the analysis.

- *Diffusion initial condition*: The form of the initial diffusion tensor varies between sections. In Chapter 2, we use an initial condition similar to that used by Hogea *et al.*, that is, we define regions of high and low diffusion representing white and gray matter regions. In Chapter 3, the initial diffusion is defined from brain atlas data following a scheme similar to that of [116].

- *Body force function*: In Chapter 2, we employ the body force function described in [54]. In Chapter 3, the body force function is taken from [114] as it was better suited to the numerical scheme.

- *Elasticity/Stress tensor*: In Chapter 2, we compare a variety of stress tensors, primarily comparing the linear elastic model used by [54] and [114], and the one-term Ogden model which was determined experimentally by [18] (see Section 2.1.2). In Chapter 3, we employ the linear elasticity model as the one-term Ogden model cannot be implemented in the software used (as discussed in Section 3.5). We also develop and implement viscoelastic version of the linear and one-term Ogden models in Chapter 2.

1.6 The 3D glioma model

With an understanding of the important biological components, previous mathematical models, and data types available, we present our 3D glioma model.

Let the spatial domain be $\Omega_{3\mathrm{D}} \subset \mathbf{R}^3$, and take time to be $t \in [0, \infty)$. Then the domain is $\mathcal{U}_{3\mathrm{D}} = \Omega_{3\mathrm{D}} \times [0, \infty)$. The tumor cell density (normalized) is denoted by c. The vector $\mathbf{m}$ denotes parameters associated with material properties of the tumor and healthy brain tissue, including diffusion $\mathbf{D}(\mathbf{x}, t)$, shear modulus $\mu(\mathbf{x}, t)$, and bulk modulus $\lambda(\mathbf{x}, t)$. The displacement and the velocity resulting from this displacement, are denoted by $\mathbf{u}(\mathbf{x}, t)$ and $\mathbf{v}(\mathbf{x}, t)$,

respectively. The system on $\mathcal{U}_{3\mathrm{D}}$ is then

$$c_t(\mathbf{x},t) = \nabla\nabla : (\mathbf{D}(\mathbf{x},\mathbf{t})c(\mathbf{x},t)) - \nabla\cdot(c(\mathbf{x},t)\mathbf{v}(\mathbf{x},t)) + \rho c(\mathbf{x},t)(1-c(\mathbf{x},t)) \tag{1.23}$$

$$\nabla\cdot\mathbf{T}\,(\mathbf{x},t,\nabla\mathbf{u}) = \mathbf{b}(c(\mathbf{x},t)) \tag{1.24}$$

$$\mathbf{v}(\mathbf{x},t) = \mathbf{u}_t(\mathbf{x},t) \tag{1.25}$$

$$\mathbf{m}_t(\mathbf{x},t) + \mathbf{v}(\mathbf{x},t)\nabla\mathbf{m}(\mathbf{x},t) = 0\,, \tag{1.26}$$

with initial conditions for $\mathbf{x}\in\Omega_{3\mathrm{D}}$

$$c(\mathbf{x},0) = c_0(\mathbf{x}), \qquad \mathbf{m}(\mathbf{x},0) = \mathbf{m}_0(\mathbf{x}), \qquad u(\mathbf{x},0) = u_0(\mathbf{x})\,. \tag{1.27}$$

The cell density has no-flux boundary conditions for $t\in[0,\infty)$ given by

$$\left[\nabla\cdot(\mathbf{D}(\mathbf{x},t)c(\mathbf{x},t)) - c(\mathbf{x},t)\mathbf{v}(\mathbf{x},t)\right]_{\partial\Omega_{3\mathrm{D}}} = 0\,. \tag{1.28}$$

For static boundaries of the spatial domain $\partial\Omega_{\mathrm{st}}$ (eg. skull), we have the boundary condition

$$\mathbf{u}(\mathbf{x},t)|_{\partial\Omega_{\mathrm{st}}} = \mathbf{0}\,. \tag{1.29}$$

On $\partial\Omega_{\mathrm{st}}$, it follows from equation (1.29) that

$$\mathbf{v}(\mathbf{x},t)|_{\partial\Omega_{\mathrm{st}}} = \mathbf{0}\,. \tag{1.30}$$

On the deformable boundaries $\partial\Omega_{\mathrm{def}}$ (eg. ventricles), we allow $\mathbf{u}(\mathbf{x},t)$ to be nonzero. Hence, $\mathbf{v}(\mathbf{x},t)$ can also be nonzero on such boundaries.

The key to closing the system is the expression of the stress tensor $\mathbf{T}$ as a function of the deformation gradient, $\nabla\mathbf{u}$, in (1.24). In this work, we explore different options for $\mathbf{T}$, such as linear elasticity or one-term Ogden elasticity, and leave the specification of $\mathbf{T}$ to later sections.

The body forces produced by the growing tumor are denoted by $\mathbf{b}$. As noted in Section 1.4, we use two forms for $\mathbf{b}$ which are detailed when introduced (see Sections 2.2 and 3.2).

Although we derive the full glioma model in 3D, we only analyze and simulate the 1D and 2D versions in Chapters 2 and 3, respectively. In Chapter 2, we reduce the model to 1D so that it is analytically tractable and we can compute invasion speeds. In Chapter 3, we simulate the 2D model as a stepping stone for a full 3D model (as discussed in Section 3.5).

Chapter 2

Comparing the effects of linear and one-term Ogden elasticity in a model of glioblastoma invasion

This chapter has been published as

[102] Meghan E. Rhodes, Thomas Hillen, Vakhtang Putkaradze, Comparing the effects of linear and one-term Ogden elasticity in a model of glioblastoma invasion. Brain Multiphysics, 2022, 100050, ISSN 2666-5220, https://doi.org/10.1016/j.brain.2022.100050.

Important background material relating to mechanical modelling of glioma and more details on the relevant literature were presented in Sections 1.2, 1.3, 1.4, and 1.5 in the Introduction chapter. Additional details of the numerics given in Sections 2.9.1, 2.9.2, and 2.9.3, as well as the methods to compute wave speed for more generalized elasticity models presented in Section 2.10, are new and not part of our paper.

Abstract

Our modelling of brain mechanics is based on observations of Budday and colleagues [18], who analyzed the elastic properties of human brain tissue samples under multiple loading modes. Using these data, Budday *et al.* determined a realistic constitutive model for brain tissue mechanics. In these studies, they found that compression and shear responses were best modelled by a non-linear one-term Ogden elasticity model, although other elasticity models are possible as well. Here we analyze the role of the elasticity model of brain tissue on the invasion speed of glioma and the resulting tissue deformation (mass effect). We present a one dimensional continuum model that couples cell dynamics to tissue mechanics. Since the mechanics of glioma-compromised brain tissue is not clear, for comprehensive studies, we incorporate both elastic and viscoelastic versions of two brain tissue elasticity models–the commonly employed linear model and the experimentally determined one-term Ogden model. For each elasticity model we identify travelling wave solutions in one dimension and calculate the corresponding invasion speeds. We find that the invasion speed is, in fact, independent of the chosen elasticity model. However, the deformations of the brain tissue, and resulting stress, between the linear and one-term Ogden models are drastically different: the Ogden model shows two orders of magnitude less deformation and three orders of magnitude less stress as compared to the linear model. Such a discrepancy might be relevant when looking at glioma-induced health complications.

2.1 Introduction

Cancers arising from glial cells, known as gliomas, form in the spine and the brain. Due to the complexity and critical functions of the brain, treatment of brain gliomas is an important and difficult task. Glioblastoma (GBM) is an aggressive form of glioma, with patients having an average life expectancy of 14 months using current treatment methods [116]. The spread of glioma is affected by many components, not only the tumor cells, but also normal cells, anatomical structures, blood circulation, and the immune response. Here we

focus on the role of tissue mechanics in this invasion process. Growing evidence shows that the structure and mechanical properties of brain tissue significantly affect the invasiveness of the glioma cells [122, 82]. Previous models of the tumor mass effect have employed a linear elasticity model. Based on brain mechanics measurements [90, 80, 18] we compare this linear model with a nonlinear one-term Ogden model. Our model focuses on the mechanics of the glioma and does not include many of the relevant clinical processes that are at play, such as immune response, angiogenesis, edema, blood flow, inflammation etc. Hence we are not attempting to develop a full glioma model, we rather like to understand the effect of cancer growth on the tissue deformation and invasion. We find that the type of elasticity model does not affect the invasion speed. This is expected in our model, since invasion is driven at the outskirts of the tumor, where the tumor density is very small, and mechanical effects are negligible. We also find that a viscous-component does not alter the response, since the glioma growth is so slow. However, we find that in the Ogden model, deformation and stress are much smaller than in the linear elasticity model. This gives an indication that mechanical stress can contribute to headaches or brain malfunctions, which are typically attributed to brain deformations and increased intracranial pressure, present only late in the disease.

2.1.1 Previous glioma models

The first and most influential diffusive model of glioma was developed by Swanson *et al.* [119], termed the *Proliferation-Invasion* (PI) model. In this model, tumor cells proliferate and invade the surrounding tissue by Fickian diffusion. The scalar diffusion coefficient varies between gray matter and white matter, where diffusion in white matter is faster. Even with this simple diffusion model, Swanson *et al.* [117, 118, 105] were able to compare model outputs to patient data with promising results. Jbabdi *et al.* [55] extended the PI model by replacing the scalar diffusion coefficient with an anisotropic diffusion tensor. Clatz *et al.* [28] built on the anisotropic PI model by including mass effect from a momentum balance equation. Bondiau *et al.* [15] expanded on Clatz *et al.* by including patient-specific mechanical parameters. The models

of Clatz, Bondiau and others [28, 15] divided the tumor cell population into a gross tumor volume 1 (GTV1) and a gross tumor volume 2 (GTV2). While the GTV2 has low density and is responsible for the diffusive invasion, the GTV1 is dense and the cause of deformations. These models use a linear elasticity model.

Ambrosi *et al.* [4] developed a full deformation theory for growing tissue. Their model was further developed by Preziosi *et al.* [24, 94] in a multiphase description of tissue growth and deformation. M. Resendiz [99] used the model with linear elasticity to analyze tumor invasion in one dimension, while Grenier [17] and Angeli *et al.* [6] considered viscoelastic multiphase models for a growing tumor.

A different approach to model tissue dynamics was taken by Lowengrub and collaborators [128, 73, 71] where deformations and cell adhesions were modelled through a suitable energy functional.

Painter and Hillen [52, 86, 87] focussed on the derivation of diffusion-type glioma models from a microscopic description of alignment of individual glioma cells with the environment. Through their framework, a fully anisotropic diffusion arose, where the diffusion tensor appears inside the two derivatives, much like in a Fokker-Planck formulation [104]. We denote such a model as fully anisotropic advection diffusion (FAAD) equation. This method works well to translate diffusion tensor imaging data (DTI) into a mathematical spread model for glioma [32, 116].

The glioma evolution models most relevant for our work are the models from G. Biros' group [54, 114]. Hogea *et al.* [54] built on the PI model by adding an advection term to the cell density evolution, which is then coupled to an equation modelling the mechanical properties of the tissue. The material properties included in this model include the diffusion tensor map and material elasticity parameters. Representing the heterogeneous diffusion, which exists biologically due to the presence of white matter, etc. in the brain, the diffusion tensor is spatially heterogeneous. Similarly, the elasticity parameters are taken to be spatially heterogeneous in order to account for the different mechanical properties of structures within the brain. The advection velocity applied to the cell density arises from a momentum balance equation which accounts for mass

effects. In [54], the brain tissue is modeled as a linearly elastic material, with forces produced by the growing tumor according to a phenomenological model dependent on both tumor cell density and gradient of the tumor cell density. Through the momentum balance equation, the forces generated by the tumor result in displacement of the tissue with an associated advection velocity. Not only is this advection velocity applied to the tumor cells, but also to the underlying tissue properties including the diffusion tensor map and elasticity parameters. In this way, Hogea *et al.* were able to capture and reproduce how glioma tumors impact brain tissue and also how this deformation can then alter the path of tumor spread. In 2019, Subramanian *et al.* [114] expanded on [54] by including multiple species (including proliferating cells, invasive cells, necrotic cells) as well as nutrients.

In our work, we modify the model from Hogea *et al.* [54] by altering both the diffusion and mechanical models. First, we employ FAAD rather than Fickian diffusion. Secondly, we not only consider linear elasticity, but also one-term Ogden elasticity, as well as viscoelastic versions of these models. We present the novel equations resulting from these assumptions, and compute the speed of propagation of a wave front modelling glioma invasion into an initially healthy tissue. We analyze how the introduction of these new factors into modelling affects both the speed and the mechanics of glioma invasion. Therefore, the new phenomena we introduce can play an important role in the prediction of glioma invasion, and, potentially, in the resulting treatment of patients.

2.1.2 Measurement of brain mechanics

The measurement of human brain mechanics is difficult. With the obvious restrictions on availability of human brain samples, most research on brain mechanics is actually done on animal tissue, including porcine, bovine, and rat brains [18, 81, 74, 123, 27, 80, 79, 90]. Studying animal brain tissue has helped to gain insights into brain tissue properties and behavior, but it is well known that the mechanical properties of human brain tissue differ significantly from other species [18, 93, 27, 19]. While comparing the mechanics of

human glioma and healthy mouse brain tissue, Pogoda *et al.* [90] observed an unusual characteristic known as *strain stiffening*, which describes the process where brain tissue becomes stiffer under strain. Strain stiffening in brain tissue has been attributed to the biphasic nature of brain tissue [19], although the mechanism is not fully understood. In an effort to determine a model of brain tissue mechanics that captured this strain stiffening property, Mihai *et al.* [80] considered the brain to be a homogeneous, isotropic, incompressible, hyperelastic material, and compared five different constitutive models with these properties. Of the five models considered, Mihai *et al.* found that the Ogden class of models was best able to fit experimental data and captured the strain stiffening behavior [80]. Furthermore, in 2017 Mihai *et al.* used experimental data from [18] to develop a family of isotropic, hyperelastic models based on the Ogden elasticity model capable of capturing brain tissue behavior under combined shear and compression/tension [79].

The study of Budday *et al.* [18] stands out as they have been able to work with human brain tissue from recently deceased individuals, tested the tissue under combined shear and compression/tension, and fit constitutive models to these experiments. Although each of these components had been explored previously, Budday *et al.* [18] were the first to combine all of these elements into one study. Budday *et al.* performed *in vitro* testing of human brain tissue samples from 10 cadavers within 48 hours of death, reducing the amount of tissue deterioration postmortem. Tissue samples from four regions of the brain (corpus callosum, corona radiata, basal ganglia, cortex) were collected and tested under various loading procedures. Not only did Budday *et al.* [18] consider different regions of the brain, they also explored if brain tissue mechanics were directionally dependent within brain regions due to the presence of white matter fibers. The experimental results were compared to five common constitutive models: neo-Hookean, Mooney-Rivlin, Demiray, Gent, and one-term Ogden. The results showed that the mechanical properties of human brain tissue are regionally dependent, but not directionally dependent, with the isotropic modified one-term Ogden model being the only constitutive model that was able to capture the hyperelastic behavior of the mechanical testing data across multiple loading modes. Following these results from Budday *et*

al. [18], we utilize the isotropic one-term Ogden model for the mechanical behavior of brain tissue into our model of glioma spread.

2.1.3 Travelling wave analysis

In this work we focus on one-dimensional invasion waves. An explicit calculation of the wave speed gives us vital information about the invasion process, and its dependence on the model parameters and the mechanical models. The method of using travelling wave speeds to determine invasiveness of populations is common in ecological literature [68, 125] and epidemiological modelling [125], but has also been applied to GBM models [40, 41, 49, 63, 118]. Swanson *et al.* [118] found that in their model the wave front was characterized by migration (diffusion) and proliferation (reaction) of tumor cells. Konukoglu *et al.* [63] also used the characteristics of a travelling wave of a reaction-diffusion model to define tumor invasion, but used additional patient-specific data taken from images, such as tissue heterogeneity and fiber structure. Gerlee and Nelander [40, 41] developed a reaction-diffusion glioma model that included switching between proliferative and motile phenotypes (go-or-grow hypothesis). They numerically and analytically determined the wave speed under suitable assumptions on the time scales of proliferation and migration, finding that the phenotypic switching rate altered the wave speed. Rather than exploring the effects of parameters on wave speed for a single model, Harko *et al.* [49] determined wave solutions for generalized versions of common glioma models. It should be noted that these models are all reaction-diffusion models that do not include advection or mechanical effects. Here, we include both advection and mechanics in our model and examine how these components alter the invasion speed.

2.1.4 Outline of the paper

We first derive our glioma mechanics model as an extension of Hogea's model [54] in Section 2.2.2. We model the glioma by a general framework where a reaction-advection-diffusion equation is coupled to a momentum balance equation which models the mechanics of the glioma and brain tissue. Driven by

the growing glioma, the momentum balance equation generates a displacement of the tissue. This displacement then results in an advection velocity which acts on both the tumor and the underlying tissue. We will introduce three biological scenarios called Bio-cases 1,2,3, which correspond to different stages of tumor development. Next we introduce the four main mechanical models, which we will refer to as Mech-cases 1, 2, 3, 4, as well as viscoelastic versions for Mech-cases 1 and 3. The elasticity models we consider are linear elasticity, linear incompressible elasticity and two cases of the one-term Ogden elasticity.

In our travelling wave analysis in Section 2.4, it turns out that we can use arguments that were similar to those used to determine minimal wave speed for the classical Fisher-KPP equation [57, 30]. With explicit expressions for the minimal wave speed, we then simulate the model to compare the analytical and simulated wave speeds, as well as to visualize the waves. We perform travelling wave analysis under each biological scenario for linear, linear incompressible, and one-term Ogden elasticity, and analyze the viscoelastic versions numerically to determine if adding viscosity to the mechanics significantly affects the results. We compare the different mechanical models and examine how each model affects glioma spread, as well as differences in tissue and mechanical dynamics between each mechanical model. Finally, we conclude by discussing how the biological and mechanical components of the model affect the existence of travelling waves, invasion wave speed, tissue dynamics, and the implications on our understanding of glioma growth.

2.2 Glioma model in 1D

Let the spatial domain be the line of length L, $x \in [0, L] = \Omega \subset \mathbf{R}$, and take time to be $t \in [0, \infty)$. Then the domain is $\mathcal{U} = \Omega \times [0, \infty)$. The tumor cell density (normalized) is denoted by c. Generally, the vector $\mathbf{m}$ denotes parameters associated with material properties of the tumor and healthy brain tissue, including diffusion $D(x,t)$, shear modulus $\mu(x,t)$, and bulk modulus $\lambda(x,t)$. Versions of the vector $\mathbf{m}$ specific to linear and one-term Ogden (visco)elasticity are given by $\mathbf{m}_{\text{Lin}} = (D, \lambda, \mu)$ and $\mathbf{m}_{\text{Ogd}} = (D, \mu)$, respectively. The body forces acting on the media are denoted by $b(x,t)$, and the viscosity coefficient

by $\eta(x,t)$. Although being a parameter associated with material properties, η is not included in the vector $\mathbf{m}$ as it is only involved in the viscoelastic versions of Mech-cases 1 and 3.

The displacement and the velocity resulting from this displacement, are denoted by $u(x,t)$ and $v(x,t)$, respectively. The system on $\mathcal{U}$ is then

$$\frac{\partial}{\partial t}c(x,t) = \frac{\partial^2}{\partial x^2}(D(x,t)c(x,t)) - \frac{\partial}{\partial x}(c(x,t)v(x,t)) + \rho c(x,t)(1-c(x,t)) \tag{2.1}$$

$$\frac{\partial}{\partial x}T\left(u_x(x,t), u_{xt}(x,t)\right) = -b(c(x,t)) \tag{2.2}$$

$$v(x,t) = \frac{\partial}{\partial t}u(x,t) \tag{2.3}$$

$$\frac{\partial}{\partial t}\mathbf{m}(x,t) + v(x,t)\frac{\partial}{\partial x}\mathbf{m}(x,t) = \mathbf{0} \tag{2.4}$$

$$\frac{\partial}{\partial t}\eta(x,t) + v(x,t)\frac{\partial}{\partial x}\eta(x,t) = 0\,, \tag{2.5}$$

with initial conditions for $x \in \Omega$

$$c(x,0) = c_0(x), \qquad \mathbf{m}(x,0) = \mathbf{m}_0(x), \qquad \eta(x,0) = \eta_0(x), \qquad u(x,0) = u_0(x)\,, \tag{2.6}$$

and boundary conditions for $t \in [0,\infty)$

$$\frac{\partial}{\partial x}c(0,t) = 0\,, \quad \frac{\partial}{\partial x}c(L,t) = 0\,, \quad \frac{\partial}{\partial x}u(0,t) = 0\,, \quad \frac{\partial}{\partial x}u(L,t) = 0\,. \tag{2.7}$$

It follows from equation (2.7) that

$$v(0,t) = 0\,, \quad v(L,t) = 0\,. \tag{2.8}$$

The key to closing the system is the expression of the stress tensor T as a function of the deformation gradient, u_x, and, for viscoelastic models, of u_{xt}, in (2.2). We consider different stress tensors: linear (Mech-case 1), linear incompressible (Mech-case 2), and one-term Ogden elastic model (Mech-cases

3,4) given by the following expressions:

$$\text{Case 1:} \quad T_{\text{Lin}}\left(u_x(x,t)\right) = \lambda(x,t)u_x(x,t) + 2\mu(x,t)u_x(x,t) \tag{2.9}$$

$$= (\lambda(x,t) + 2\mu(x,t))u_x(x,t)\,, \tag{2.10}$$

corresponding to all *deformations* being strictly one-dimensional along the x-axis, in other words, the deformation gradient tensor F having only one non-zero component, F_{11}, with other components of the deformation gradient tensor vanishing. An alternative model is obtained by assuming that the deformations are three-dimensional, but the stress is applied only in one direction. As we show below in (2.31), the stress $T_{11} = T$ relates to u_x as

$$\text{Case 1a:} \quad T_{\text{Lin1D}}\left(u_x(x,t)\right) = \mu(x,t)\frac{3\lambda(x,t) + 2\mu(x,t)}{\lambda(x,t) + \mu(x,t)}u_x(x,t)\,. \tag{2.11}$$

The next case is obtained by assuming the linear incompressible material, in which case, as we demonstrate below in (2.29), the stress $T_{11} = T$ relates to strain u_x as

$$\text{Case 2:} \quad T_{\text{LinInc}}\left(u_x(x,t)\right) = 3\mu(x,t)u_x(x,t)\,. \tag{2.12}$$

The incompressible material with uniaxial compression/tension described by the Ogden's model is derived below in (2.24), and relates the stress T to u_x as:

$$\text{Case 3:} \quad T_{\text{Ogd}}(u_x(x,t)) = \frac{2\mu(x,t)}{\alpha}\left((1-u_x(x,t))^{-\alpha} - (1-u_x(x,t))^{\frac{1}{2}\alpha}\right), \tag{2.13}$$

The value α that appears both as an exponent and scaling factor in the one-term Ogden model is a parameter. Although α has no specific physical meaning, it can be fit for a specific material and loading conditions (as discussed in Section 2.2.2). Finally, we consider viscoelastic versions of Mech-cases 1 and 3 above:

$$\text{Case 4:} \quad T_{\text{LinV}}\left(u_x(x,t), u_{xt}(x,t)\right) = (\lambda(x,t)+2\mu(x,t))u_x(x,t)+\eta(x,t)u_{xt}(x,t)\,, \tag{2.14}$$

Case 5: $T_{\text{OgdV}}\left(u_x(x,t), u_{xt}(x,t)\right) =$

$$\frac{2\mu(x,t)}{\alpha}\left((1-u_x(x,t))^{-\alpha} - (1-u_x(x,t))^{\frac{1}{2}\alpha}\right) + \eta(x,t)u_{xt}(x,t)\,, \tag{2.15}$$

We note that for the one-term Ogden viscoelasticity, we developed an alternative viscosity form that is similar to that of Kelvin-Voigt, but has the advantage of enhanced energy dissipation for high stresses, as derived in Appendix 2.8. The results of the glioma model with T_{OgdV2} from that Appendix were nearly identical to that of the results with (2.15) and thus are not included in the main text. For the derivation and select results of the model with T_{OgdV2}, see Appendix 2.8.

The functional form for the body forces through the growing tumor b is taken from [54] as

$$b\left(c, \mathbf{p}, c_x\right) = -f(c,\mathbf{p})c_x = p_1 \exp\left(-\frac{p_2}{c^s}\right) \exp\left(-\frac{p_2}{(2-c)^s}\right) c_x\,, \tag{2.16}$$

where $\mathbf{p} = (p_1, p_2, s)$, and p_1, p_2, and s are all positive constants. The vector $\mathbf{p}$ is a vector of parameters determining the size of area deformed by the tumor cells (p_2, s) and the strength of this deformation (p_1). This is a phenomenological model for the forces created by a growing tumor. There are key characteristics of this model that capture the likely reality of a growing tumor. First, in the absence of tumor cells, there is no force. Secondly, the first component of the force (the exponential part) is maximized at the carrying capacity of the tumor (i.e., when $c(x,t) = 1$). Lastly, the dependence on the gradient means that a larger force is generated in the presence of large differences in cancer density. The parameter p_1 is scaled by the initial value of the coefficient on the stress tensor which represents the elasticity of gray and white matter. This ensures that the relative scales of the material properties and forcing function are similar and result in a reasonable level of mass effect. That is, $p_1 = \lambda + 2\mu$ for the linear elastic case, $p_1 = 3\mu$ for the incompressible linear elastic case, and for the Ogden model, $p_1 = \left|\frac{2\mu}{\alpha}\right|$, where we take the absolute value in the Ogden case because α is negative. Hogea *et al.* [54] also employed this method of scaling p_1 by the value of the material's elasticity

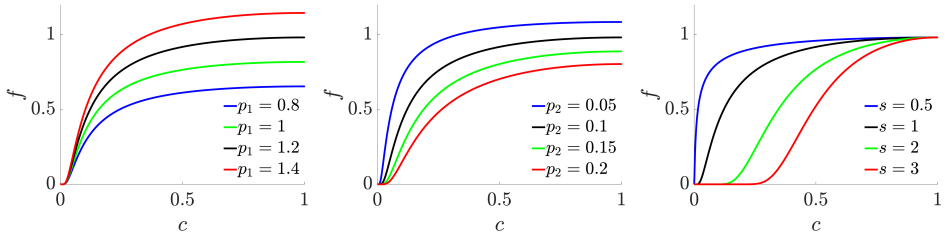

Figure 2.1: The forcing function, f, with a parameter set used in Hogea *et al.* [54] ($\mathbf{p} = (p_1, p_2, s) = (1.2, 0.1, 1)$) (*black curves*) and changes in the forcing function depending on varying the parameters p_1 (*left*), p_2 (*middle*), and s (*right*).

parameter. However, Hogea *et al.* [54] used artificial values for the elasticity parameters in order to explore their model. Here, we will incorporate experimental data for λ, μ, and η, and therefore the scaling of p_1 will follow the data for those parameters. Furthermore, Hogea *et al.* [54] assigned different values of elasticity parameters for gray and white matter. Following recent evidence suggesting the mechanical properties of brain tissue are homogeneous between white and gray matter [18], we assign the same elasticity parameters for both gray and white matter. Finally, following values used in [54], we take $p_2 = 0.1$ and $s = 1$ throughout the simulations presented in the following sections. The form of f with $\mathbf{p} = (1.2, 0.1, 1)$ (values used in Hogea *et al.* [54]) is shown as the black curves in Figure 2.1. Notice that the diffusion term in equation (2.1) is of Fokker-Planck form $(Dc)_{xx}$, which arises naturally from a random walk description of cell movement [52]. Since we consider a spatially one-dimensional model, there are no anisotropies, but if $D(x, t)$ depends on space and time, for example through deformation of the tissue, then we use the above term.

Following the method of Hogea *et al.* [54], the material parameters (D, λ, μ) are dependent on space and time, and are convected by the velocity produced by the growing tumor. We note that this is only one option for the choice of modelling material property evolution and that other factors could be included in the material property evolution, such as including dependency on tumor cell and/or tissue density. For this work, we limit ourselves to the case where the material properties are independent of cell density.

Table 2.1: Summary of model notation.

Notation	Description
x	Space
t	Time
$c(x,t)$	Tumor cell density
ρ	Tumor cell growth rate
$u(x,t)$	Displacement
$v(x,t)$	Advection velocity
$D(x,t)$	Diffusion coefficient
$\lambda(x,t)$	Bulk modulus
$\mu(x,t)$	Shear modulus
$\eta(x,t)$	Viscosity coefficient
$\mathbf{m}(x,t)$	Vector of material properties
T	Stress tensor
$b(c,\mathbf{p},c_x)$	Body force function
$\mathbf{p}=(p_1,p_2,s)$	Vector of body force function parameters

It is of note that Budday *et al.* [18] found a constant value for μ. In the following sections, we explore how changing μ affects the dynamics. Budday *et al.* determined this value of μ for healthy tissue, and we expect μ to change for glioma tissue. There is significant evidence showing that glioma is mechanically heterogeneous and affects the nature of healthy brain tissue, including altering the mechanical properties [48, 109, 82, 88, 90]. That is, it is plausible to assume that glioma introduces time- and space-dependent elasticity parameters. Thus, allowing for variation of the elasticity parameters μ and λ is not a biologically unrealistic choice.

Finally, the tumor cell density proliferates following the commonly used logistic growth model [31]. A summary of the model notation is given in Table 2.1.

2.2.1 Biological scenarios

We perform this analysis for three cases representing different biological scenarios.

Bio-case 1: Early cerebral glioma in physically homogeneous brain tissue. Here, the material variables (diffusion, elasticity, viscosity) are held constant. This represents a tumor that is growing in a homogeneous environment (a single brain structure with homogeneous physical properties) such that the tumor has the same properties as the environment, corresponding to an early stage of tumor development. This represents, for example, an early tumor growing only within gray matter [91, 116, 119, 89].

Bio-case 2: Early cerebral glioma in the presence of white matter. In this case, the mechanical properties of the tissue are constant, while the diffusion coefficient D is allowed to vary. This represents the case where a tumor is growing in mechanically homogeneous tissue, but with the presence of structures that alter the migration rates of the tumor cells, such as white matter. Regions with higher diffusion model the regions with white matter as tumor cells diffusion is faster along white matter fibers [43, 91, 116, 119]. The regions with lower diffusion represent the gray matter. Deformation caused by the tumor cell density deforms the tissue and as a result also transports the diffusion value accordingly. Hence in this case $D(x,t)$ will depend on space and time. As before in Bio-case 1, the elasticity parameters, λ and μ being constant represents that the elasticity of the brain tissue is uniform throughout [18].

Bio-case 3: Advanced glioma: mechanically heterogeneous glioma in a heterogeneous environment. This is the most general case where the mechanical properties of the tissue are fully variable, as well as the diffusion coefficient. This represents a tumor that can have different mechanical properties compared to the healthy tissue (advanced tumor), as well as the invaded tissue includes structures with different mechanical properties (cerebrum, ventricles, corpus callosum, etc.) [28, 54, 114]. The ventricles are a fluid filled

cavity in the center of the brain, while the corpus callosum is a dense, fibrous structure separating the two hemispheres. As the brain matter structure is pushed (advected) by the tumor, the elastic properties associated with different brain structures are pushed as well, hence the parameters $\mathbf{m}_{\text{Lin}} = (D, \lambda, \mu)$ and $\mathbf{m}_{\text{Ogd}} = (D, \mu)$, as well as η, follow the advection equation (2.4).

2.2.2 Mechanical models

Inspired by the work of Budday *et al.* [18] who performed mechanical testing of brain tissue as described above, we explore four main mechanical models: the linear elasticity model, linear incompressible elasticity model, one-term Ogden models with $\alpha = -7.3$ and $\alpha = -20$, as well as the corresponding viscoelastic models for the linear and one-term Ogden (with $\alpha = -20$) models.

Mech-case 1: Linear elasticity. For this case, we use equation (2.10) as the stress tensor. The linear elasticity model is included since it is by far the most commonly used in mathematical models of glioma [54, 114, 28, 15, 99]. As indicated by Budday *et al.* [18], this model is likely an oversimplified view of the mechanical behavior of brain tissue, but allows for a tractable inclusion of tissue elasticity in continuum models. We are also interested in comparing our results with previous work, and thus including analysis with the linear elasticity model allows for such direct comparison. Of note is that this model is compressible, which is in contrast to the one-term Ogden model which is incompressible. As the parameter values determined depend on the elasticity model tested, in order to use elasticity parameters determined with the linear elasticity model, we take values from [54] for λ and μ in this case.

Mech-case 2: Incompressible linear elasticity. Here, we use equation (2.12) as the stress tensor. We include an incompressible version of linear elasticity in order to have a direct comparison of linear and one-term Ogden models where the incompressibility property is included in both models. The value of μ used in this case will be the same as used in Mech-case 3 and 4 in order to directly compare results with those cases.

Mech-case 3: One-term Ogden elasticity with combined loading ($\alpha = -20$). The model that most closely represents the behavior of brain tissue is the one-term Ogden model [18]. Based on the results in Budday [18], the parameter value for the exponent α depends on the mechanical loading, with the value $\alpha = -20$ giving a good fit for combined loading such as shear *and* compression. For this Mech-case, the stress tensor is given by equation (2.13) where $\alpha = -20$. Note that the form of one-term Ogden model used in both Mech-cases 3 and 4 assumes incompressibility. The value of μ used in both Mech-case 3 and 4 is taken from [18] as these are the values found when calibrating the one-term Ogden model.

Mech-case 4: One-term Ogden elasticity with single loading ($\alpha = -7.3$). The final case we consider again uses one-term Ogden elasticity (equation (2.13)), but now with $\alpha = -7.3$. According to Budday [18], this value of α represents brain tissue mechanics under single loading.

We note that the values of α for the one-term Ogden models were determined under specific testing methods and it is possible that they are not applicable outside of these conditions. As noted in [19], the large absolute value of α can lead to "unrealistically high stresses for larger strains". However, given the long time scales of glioma growth, we believe it is reasonable to assume that a growing glioma falls under a small strain rate regime. Under this assumption, the larger absolute value α, i.e. $\alpha = -20$, is an appropriate choice. Furthermore, in the results presented in later sections, the stress values of the model with one-term Ogden elasticity with $\alpha = -20$ yield smaller stress values than both the linear model and the one-term Ogden model with $\alpha = -7.3$, indicating that the stress values are not unreasonably large. To our knowledge, this is the first time glioma invasion has been analyzed for a mathematical model including the one-term Ogden model for tissue mechanics.

To include viscoelastic effects in the elasticity models, we use the Kelvin-Voigt model [70] which adds the viscosity term $\eta u_{xt}(x,t)$ to each of the original Cauchy stress tensors given by (2.10) and (2.13), giving (2.14) and (2.15) as the respective viscoelastic counterparts. As mentioned before, we introduce

an alternative version of a viscoelastic Ogden model in Appendix 2.8.

Derivation of 1D one-term Ogden stress tensor. The different mechanical models are included via the Cauchy stress tensor $T(u_x, u_{xt})$ (in the deformed configuration) which appears in the momentum balance equation (2.2). The Cauchy stress tensor for the commonly used linear model (T_{Lin}) is given by (2.10). As the one-term Ogden model is less commonly used, for clarity we derive the 1D form of the Cauchy stress tensor (T_{Ogd}). The strain energy for the one-term Ogden Model in 3D is

$$W = \frac{2\mu}{\alpha^2}(\hat{\lambda}_1^{\alpha} + \hat{\lambda}_2^{\alpha} + \hat{\lambda}_3^{\alpha} - 3)\,, \tag{2.17}$$

[18, 84] where $\hat{\lambda}_i$ are the principal stretches (note that the hat distinguishes the principal stretch from the elasticity parameter λ), $\mu = \mu_{\text{Ogd}}$ is the shear modulus, and α is a parameter [18].

Note that we have chosen the definition of energy in (2.17) to have an additional factor $1/\alpha$ as compared with the original paper by Ogden [84]. We have chosen that notation in order for the linearized relationship between stress and strain for Ogden model at null strain (2.25) and incompressible linear model (2.29) coincide when the parameters μ in both models are equal: $\mu_{\text{Ogd}} = \mu_{\text{LinInc}}$. The Cauchy stress tensor components are then

$$T_i = -\,p + \hat{\lambda}_i \frac{\partial W}{\partial \hat{\lambda}_i} = -p + \sum_i \frac{2\mu}{\alpha}\hat{\lambda}_i^{\alpha}\,, \tag{2.18}$$

which gives the individual stress tensor components as

$$T_1 = -\,p + \frac{2\mu}{\alpha}\hat{\lambda}_1^{\alpha}\,, \quad T_2 = -p + \frac{2\mu}{\alpha}\hat{\lambda}_2^{\alpha}\,, \quad T_3 = -p + \frac{2\mu}{\alpha}\hat{\lambda}_3^{\alpha}\,, \tag{2.19}$$

where p is the pressure. Because we are only considering a single spatial dimension in this work, we can reduce the stresses to uniaxial compression/tension. Therefore, the general stress tensor reduces to T_1. Thus, we will denote

$T := T_1$. Under uniaxial compression/tension, $T_2 = T_3 = 0$, giving

$$T_2 = -p + \frac{2\mu}{\alpha}\hat{\lambda}_2^{\alpha} = 0\,, \quad T_3 = -p + \frac{2\mu}{\alpha}\hat{\lambda}_3^{\alpha} = 0 \implies \hat{\lambda}_2 = \hat{\lambda}_3\,. \tag{2.20}$$

The condition for an isotropic and incompressible material is $\hat{\lambda}_1\hat{\lambda}_2\hat{\lambda}_3 = 1$ [84]. Denoting $\hat{\lambda}_1 := \hat{\lambda}$ we get $\hat{\lambda}_2 = \hat{\lambda}_3 = \sqrt{\hat{\lambda}}^{-1}$. With this pressure p, the equation for T_2 gives the pressure as

$$p = \frac{2\mu}{\alpha}\hat{\lambda}_2^{\alpha} = \frac{2\mu}{\alpha}\left(\frac{1}{\sqrt{\hat{\lambda}}}\right)^{\alpha}\,. \tag{2.21}$$

Plugging this form of p into the equation for T_1, we get the 1D form of the one-term Ogden stress tensor as

$$T_{\text{Ogd}} := T_1 = \frac{2\mu}{\alpha}\left(\hat{\lambda}^{\alpha} - \left(\frac{1}{\sqrt{\hat{\lambda}}}\right)^{\alpha}\right) = \frac{2\mu}{\alpha}(\hat{\lambda}^{\alpha} - \hat{\lambda}^{-\frac{1}{2}\alpha})\,. \tag{2.22}$$

We now connect this expression for the Cauchy stress to the variables in our model. That is, we determine the relationship between the principal stretch, $\hat{\lambda}$, and displacement, u. Consider a deformation in spatial coordinates, where X is the Lagrangian label, which can be taken to be the initial coordinate of the material particle, and x is the final (Eulerian) position of the material particle. In 1D, we can write the deformation gradient as $F_{11} = \hat{\lambda}$. The principal stretch is given by the square roots of the eigenvalues of the left Cauchy-Green tensor defined by $\mathbf{b} = FF^T$, mapped in the Eulerian coordinates x (note that here $\mathbf{b}$ indicates the left Cauchy-Green tensor, rather than the force in the momentum balance equation (2.2)). For the one-dimensional dynamics, $F_{11} = X_x^{-1}$, we then get $\mathbf{b}_{11} = X_x^{-2} = \hat{\lambda}^2$. We use this relation between the principal stretch and deformation gradient to connect the principal stretch to displacement $u = x - X(x,t)$:

$$\hat{\lambda} = \frac{1}{1 - u_x(x,t)} \tag{2.23}$$

To connect this to displacement, we replace $\hat{\lambda}$ in equation (2.23), giving

$$T_{\text{Ogd}} = \frac{2\mu(x,t)}{\alpha}\big((1-u_x(x,t))^{-\alpha} - (1-u_x(x,t))^{\frac{1}{2}\alpha}\big)\,. \tag{2.24}$$

The linearization of the Ogden's stress given by (2.24) at equilibrium $u_x = 0$ is then

$$T_{\text{Ogd}} \simeq 3\mu u_x\,. \tag{2.25}$$

The coefficient 3μ in (2.25) is sometimes called the tangent modulus at null deformation.

In what follows, we use the 1D model corresponding to free stress, as it is more physical in the description of propagation of glioblastoma we are interested in. The most dangerous and rapid spread of the tumor occurs along a particular direction in the brain, while the stress from the invasion is dissipated in the nearby brain tissue. Thus, the 1D free stress Ogden model is advantageous to the plane model above. The plane model could also be useful for particular applications of the dynamics strictly constrained in a narrow domain for some physiological reason, which we shall not pursue here.

Note that (2.24), in spite of being called the one-term Ogden model, has two terms incorporating u_x. The name "one-term model" actually refers to the fact that there is only one power α in the expression for the Ogden model (2.17). The second term in that expression, proportional to $((1-u)_x)^{\frac{1}{2}\alpha}$, comes from the pressure term in (2.18) computed incompressibility criteria for the material, governed by the first term proportional to $((1-u)_x)^{-\alpha}$. We hope that no confusion in the nomenclature should arise here.

Incompressible linear models. In order to compare with the incompressible Ogden model, it is desirable to develop an interpretation of incompressible linear models. In general, the stress and strain in linear elastic models are written as

$$T^0_{\text{Lin}} = 2\mu\epsilon + \lambda \text{tr}\epsilon I\,, \quad \epsilon = \frac{1}{2}\left(\nabla\mathbf{u} + \nabla\mathbf{u}^T\right)\,. \tag{2.26}$$

Here, λ and μ are Lamé parameters. One has to be careful here, as the bulk modulus K and Lamé parameter λ are connected to the elastic modulus E

and Poisson's ratio ν through the expressions

$$K = \frac{E}{3(1-2\nu)}\,, \quad \lambda = \frac{\nu E}{(1+\nu)(1-2\nu)}\,, \quad \mu = \frac{E}{2(1+\nu)}\,. \tag{2.27}$$

For the three dimensional incompressible materials the Poisson ratio $\nu \to 0.5$ so the expression for λ given by (2.27), technically speaking, diverges. More precisely, there is an indeterminate coefficient $\lambda \mathrm{tr}\epsilon$ in the stress-strain relationship since in the limit of incompressibility, $\lambda \to \infty$ and $\mathrm{tr}\epsilon \to 0$. To resolve that uncertainty, one should use an additional pressure term p in the expression for stress T as follows:

$$T_{\mathrm{LinInc}} = 2\mu\epsilon - pI\,, \quad \mathrm{tr}\epsilon = 0\,. \tag{2.28}$$

For uniaxial compression/tension of a uniform material along the x direction (first coordinate), let us denote $\epsilon_{11} = u_x$. Because of symmetry and incompressibility, $\epsilon_{22} = \epsilon_{33} = -u_x/2$. Since no stress is applied to the sides, $T_{22} = T_{33} = 0$ which gives $p = -\mu u_x$. Thus, $T_{11} = 3\mu u_x$, and the effective value of the elastic modulus for one-dimensional dynamics in the x dimension is 3μ, where $\mu = \mu_{\mathrm{LinInc}}$ is the Lamé parameter denoting the shear modulus:

$$T_{\mathrm{LinInc}} = 3\mu u_x\,, \tag{2.29}$$

In order to match the linear elasticity with the tangent modulus for the Ogden model at $u_x = 0$, we take the shear modulus Lamé parameter $\mu_{\mathrm{LinInc}} = \mu_{\mathrm{Ogd}}$, where μ_{Ogd} is the coefficient from (2.25). Figure 2.2 shows stress as a function of the displacement derivative for all four mechanical models, with the far right panel showing that the incompressible linear model (i.e. where $T = 3\mu_{\mathrm{Ogd}} u_x$) is indeed tangent to the stress exhibited by the Ogden models at null strain.

Physical interpretation of compressible linear models. Similarly to the derivation above, we can consider a linear model (2.26) with the stress applied only along the x direction, so $T_{11} = T$, $T_{22} = T_{33} = 0$. We still have $\epsilon_{22} = \epsilon_{33}$, and thus $\mathrm{tr}\epsilon = \epsilon_{11} + 2\epsilon_{22}$. The stress conditions in (22) and (33)

directions yield

$$\epsilon_{22} = \epsilon_{33} = -\frac{\lambda}{2(\lambda+\mu)}\epsilon_{11} \quad \Rightarrow \quad \text{tr}\epsilon = \frac{\mu}{\lambda+\mu}\epsilon_{11} \tag{2.30}$$

and therefore

$$T = T_{11} = \mu\frac{3\lambda+2\mu}{\lambda+\mu}\epsilon_{11} = \mu\frac{3\lambda+2\mu}{\lambda+\mu}u_x \tag{2.31}$$

Note that as $\lambda \to \infty$ when the material tends to the incompressibility $\nu \to 0.5$ according to (2.27), the value of the coefficient of proportionality between stress T_{11} and strain u_x tends to 3μ, in accordance with the previous calculation on incompressibile one-dimensional stress-strain relationship.

The physics of the models considered here is quite different from the pure 1D model. In the expressions (2.29) and (2.31), we assumed that the stress is applied in one direction, but material particles are free to move in all available directions. Another way to interpret the one-dimensionality of models is enforce the motion of the particles in one dimension only. In that case, we obtain the stress-strain relationship given by (2.10).

Thus, we present two sets of results related to the linear model. One is the incompressible linear model derived here, corresponding in the linear regime to the Ogden's model. Another linear model presented in the paper is obtained with the values of λ and μ obtained from the literature [54], which is Case 1 described by (2.10) above.

Remark 1 (On the equations with non-constant elasticity parameters)**.** One can notice that the derivation of incompressible stress-strain relationships above (2.24), (2.29) and (2.31) remain valid for non-constant values of elasticity parameters as long as the appropriate symmetry conditions for the displacement and stress are satisfied. We shall always assume that it is true everywhere in the paper.

Analysis of elastic models. Before considering the entire glioma system, we consider the behavior of each of the elastic models. Beginning with the stress, we can consider the stress as a function of u_x under a given set of material parameters, $\mathbf{m} = (D, \lambda, \mu)$. Figure 2.2 shows stress as a function of

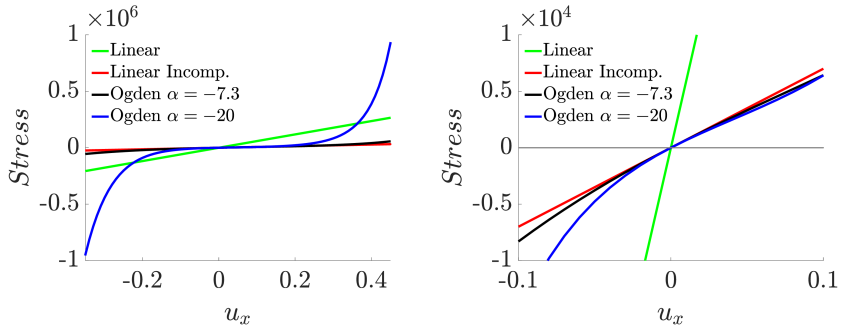

Figure 2.2: Plots of stress as a function of the spatial derivative of displacement, u_x, for each mechanical model. *Left*: For the linear elasticity (Mech-case 1), $\lambda = \bar{\lambda}$ and $\mu = \bar{\mu}_{\text{Lin}}$. For the linear incompressible (Mech-case 2) and Ogden elasticity models (Mech-case 3, 4), $\mu = \bar{\mu}_{\text{Ogd}}$. *Right*: A zoom in around $u_x = 0$ showing that the stress for each model is zero when $u_x = 0$ as expected (confirmed numerically). See Tables 2.4 and 2.5 for parameter notation.

u_x for linear elasticity, as well as Ogden elasticity with $\alpha = -7.3$ and $\alpha = -20$. It can be seen in Figure 2.2 that the stress functions differ significantly away from $u_x = 0$ and would give vastly different results for displacement and stress.

For example, the left panel of Figure 2.2 shows that near $u_x = 0$, there is a region where the linear model would result in larger stresses then the Ogden model with $\alpha = -20$, with this relationship inverting at larger values of u_x. Additionally, if $u_x = -0.2$, the Ogden stress with $\alpha = -20$ would have much larger scales compared to the linear stress or Ogden with $\alpha = -7.3$ (see Figure 2.2). For u_x near zero the functions take similar values. However, the larger magnitude exponent in the $\alpha = -20$ case leads to a much steeper curve as $|u_x|$ increases, with the magnitude of the stress becoming considerably different between the $\alpha = -7.3$ and $\alpha = -20$ cases. Thus, in cases where the displacement derivative remains near zero, the resulting stress will be similar between the two cases of α. Thus, there is a possibility that the stress produced in the full model system may be similar between all elasticity models under the condition that the value of u_x remains near zero. However, if u_x deviates from zero, the models would give considerably different stress dynamics, with differences in stress likely leading to different dynamics in other model components.

2.3 Travelling waves

Considering the four Mech-cases, as well as the two viscoelastic counterparts to Mech-case 1 and 3, and three biological scenarios, we have 18 cases to examine. In each case we explore the invasion speed, as well as how the invasion speed depends on the model parameters and the mechanical models used. We also compare the levels of deformation and stress that arise from the various formulations. We begin the travelling wave analysis with purely elastic linear, linear incompressible, and one-term Ogden mechanical models for the most general biological case (Bio-case 3); the other cases are similar. The corresponding viscoelastic models cannot be treated analytically on the same level, and we reside to numerical simulations. We show numerically that the invasion speeds are unchanged between elastic and viscoelastic formulations for the values of parameters we investigated.

2.3.1 Linear, linear incompressible, and one-term Ogden elasticity

To determine the wave speed, we transform our model (2.1) - (2.4) to a corresponding autonomous system by changing the argument of our functions from (x, t) to the travelling wave coordinates $z = x - \sigma t$, where $\sigma > 0$ is the wave speed (if it exists). With this change in coordinates, we also change the domain given in Section 2.2. Rather than a bounded spatial domain, we consider the entire real line $\mathbb{R}$ with conditions at $\pm\infty$. In the following, we present the details of the travelling wave analysis for linear elasticity and Bio-case 3.

For clarity, we introduce variable notation for the variables in travelling wave coordinates as follows:

- $c_0 = c(x - \sigma t)\,, c_1 = c'(x - \sigma t)$
- $D_0 = D(x - \sigma t)\,, D_1 = D'(x - \sigma t)$
- $u_0 = u(x - \sigma t)\,, u_1 = u'(x - \sigma t)$
- $\lambda = \lambda(x - \sigma t)$

- $\mu = \mu(x - \sigma t)$.

The autonomous system in the wave variable $z = x - \sigma t$ corresponding to the system (2.1)-(2.4) with variable $\mathbf{m}_{\text{Lin}} = (D, \lambda, \mu)$ and stress tensor given by (2.10) is

$$\begin{aligned} c_0' =& c_1 \\ c_1' =& \frac{1}{D_0}\left(-\sigma c_1 - D_1' c - 2D_1 c_1 + c_0(-\sigma u_1') + c_1(-\sigma u_1) - \rho c(1-c)\right) \\ u_0' =& u_1 \\ u_1' =& \frac{1}{\lambda + 2\mu}(f(c_0)c_1 - (\lambda + 2\mu)' u_1) \end{aligned} \tag{2.32}$$

along with the equation for the material properties

$$-\sigma \mathbf{m}'(1 + u_1) = \mathbf{0}\,, \tag{2.33}$$

where

$$f(c_0) = p_1 e^{-p_2\left(\frac{1}{c_0^s} + \frac{1}{(2-c_0)^s}\right)}\,. \tag{2.34}$$

For the boundary conditions, we have

$$\begin{aligned} & c_0(-\infty) = 1, c_0(\infty) = 0\,, \\ & c_1(\pm\infty) = 0\,, \\ & u_0(\pm\infty) = 0\,, \\ & u_1(\pm\infty) = 0\,, \\ & D_0(-\infty) = D_0^{-\infty}\,, D_0(\infty) = D_0^{\infty}\,, D_0^{\pm\infty} > 0\,, \\ & D_1(\pm\infty) = 0\,, \\ & \lambda(-\infty) = \lambda_0^{-\infty}\,, \lambda(\infty) = \lambda_0^{\infty}\,, \lambda_0^{\pm\infty} > 0\,, \\ & \mu(-\infty) = \mu_0^{-\infty}\,, \mu(\infty) = \mu_0^{\infty}\,, \mu_0^{\pm\infty} > 0\,. \end{aligned} \tag{2.35}$$

where $D_0^{\pm\infty}\,, \lambda_0^{\pm\infty}\,, \mu_0^{\pm\infty}$ is used to indicate that any (finite) value can be taken. The boundary conditions for c_0 represent a tumor cell density at carrying ca-

pacity for $x \to -\infty$, with no tumor cells present for $x \to \infty$. Thus, a travelling wave moving to the right represents the invasion of tumor cells into this previously healthy region. With the given conditions on tumor cell densities as $x \to \pm\infty$, there is no change in tumor cell density as $x \to \pm\infty$. Thus, the boundary conditions as $x \to \pm\infty$ for c_1 are both taken to be zero. As displacement of the tissue due to tumor cell presence is dependent on changing cell densities, no displacement or change in displacement is expected where c_1 is zero. Thus, the boundary conditions for both u_0 and u_1 are zero for $x \to \pm\infty$.

As for the diffusion coefficient boundary conditions, $D_0(\pm\infty)$, the PDE system allows for the boundary condition to be prescribed as any finite, real, positive value. Within the context of glioma, it should be noted that there would be limits on the magnitude of the diffusion coefficient dictated by the biological context.

The boundary conditions for the shear and bulk moduli, $\mu_0(\pm\infty)$ and $\lambda_0(\pm\infty)$ are taken to be positive values for the simulations presented here.

Lemma 1. *Consider the glioma model in travelling wave coordinates* (2.32)-(2.35) *with linear elasticity (that is, with stress tensor* (2.10)*). A necessary condition for the existence of a travelling wave is* $\sigma \geq \sigma^* = 2\sqrt{D_0^\infty \rho}$. *We call* σ^* *the minimum (theoretical) wave speed.*

Proof. A travelling wave of system (2.32)-(2.35) arises as a heterogeneous connection between a cancer free steady state at the wave front, with a coexistence equilibrium at the back of the wave. We denote the equilibrium points, $(c_0, c_1, D_0, D_1, u_0, u_1, \lambda, \mu)$, for the system by X_0 and X_1, where

$$X_0 = (0, 0, D^{*0}, 0, u^{*0}, 0, \lambda^{*0}, \mu^{*0}), \tag{2.36}$$

$$X_1 = (1, 0, D^{*1}, 0, u^{*1}, 0, \lambda^{*1}, \mu^{*1}), \tag{2.37}$$

where the values $D^{*0}, u^{*0}, \lambda^{*0}, \mu^{*0}$ and $D^{*1}, u^{*1}, \lambda^{*1}, \mu^{*1}$ can be any positive finite value. Given that we are assuming travelling wave solutions, the equi-

librium values necessarily take on the boundary values. Thus,

$$(D^{*0}, u^{*0}, \lambda^{*0}, \mu^{*0}) = (D_0^{\infty}, u_0^{\infty}, \lambda_0^{\infty}, \mu_0^{\infty}), \tag{2.38}$$

$$(D^{*1}, u^{*1}, \lambda^{*1}, \mu^{*1}) = (D_0^{-\infty}, u_0^{-\infty}, \lambda_0^{-\infty}, \mu_0^{-\infty}). \tag{2.39}$$

With the material properties satisfying equation (2.33), as we do not wish to restrict the value of u_1, this leads to the condition that $\mathbf{m}' = \mathbf{0}$ at equilibrium. That is, all of the material properties are constant at equilibrium. Holding $\mathbf{m}$ constant at equilibrium allows us to reduce the analysis to the remaining variables of c_0, c_1, u_0, and u_1. With $\mathbf{m}' = \mathbf{0}$, (2.32) reduces to

$$\begin{aligned} c_0' =& c_1 \\ c_1' =& \frac{1}{D}\left(-\sigma c_1 - \frac{-\sigma c_0 f(c_0) c_1}{\lambda + 2\mu} - \sigma c_1 u_1 - \rho c_0 (1 - c_0)\right) \\ u_0' =& u_1 \\ u_1' =& \frac{f(c_0) c_1}{\lambda + 2\mu}. \end{aligned} \tag{2.40}$$

Evaluating the Jacobian at the equilibrium points X_0 and X_1 gives

$$J(X_0) = \left[\begin{array}{cc|cc} 0 & 1 & 0 & 0 \\ -\frac{\rho}{D^{*0}} & -\frac{\sigma}{D^{*0}} & 0 & 0 \\ \hline 0 & 0 & 0 & 1 \\ 0 & 0 & 0 & 0 \end{array}\right] \tag{2.41}$$

and

$$J(X_1) = \begin{bmatrix} 0 & 1 & 0 & 0 \\ \frac{\rho}{D^{*1}} & -\frac{\sigma}{D^{*1}}\left(1+\frac{1}{\lambda^{*1}+2\mu^{*1}}\right) & 0 & 0 \\ 0 & 0 & 0 & 1 \\ 0 & \frac{1}{\lambda^{*1}+2\mu^{*1}} & 0 & 0 \end{bmatrix}. \tag{2.42}$$

Given the structure of $J(X_0)$, two of the eigenvalues are zero, with the remaining two eigenvalues determined by the upper left 2x2 matrix

$$M_{X_0} = \begin{bmatrix} 0 & 1 \\ \frac{-\rho}{D^{*0}} & \frac{-\sigma}{D^{*0}} \end{bmatrix}, \quad \text{with} \quad \det M_{X_0} = \frac{\rho}{D^{*0}}, \quad \operatorname{tr} M_{X_0} = -\frac{\sigma}{D^{*0}}. \tag{2.43}$$

Because $\sigma, D^{*0}, \rho > 0$ the determinant is positive and the trace is negative. Thus, X_0 is either a stable spiral or stable node. We assume, as in the classical Fisher case, that the minimal wave speed occurs where this fixed point switches between a stable spiral or stable node. To find this point, we solve for σ when the discriminant is zero:

$$(\operatorname{tr} M_{X_0})^2 = 4 \det M_{X_0} \implies \frac{\sigma^2}{(D^{*0})^2} = 4\frac{\rho}{D^{*0}} \implies \sigma = 2\sqrt{D^{*0}\rho}. \tag{2.44}$$

For $\sigma > 2\sqrt{D^{*0}\rho}$, X_0 is a stable node and for $\sigma < 2\sqrt{D^{*0}\rho}$, a stable spiral. Thus, for $\sigma > 2\sqrt{D^{*0}\rho}$, the existence of a travelling wave is possible, whereas $\sigma < 2\sqrt{D^{*0}\rho}$ does not permit the existence of a travelling wave.

Similarly, for the matrix $J(X_1)$, we determine that there are two zero

eigenvalues. The remaining two eigenvalues are given by

$$\Lambda_{1,2} = -\frac{\sigma}{D^{*1}}\left(1+\frac{1}{\lambda^{*1}+2\mu^{*1}}\right) \pm \sqrt{\left(\frac{\sigma}{D^{*1}}\left(1+\frac{1}{\lambda^{*1}+2\mu^{*1}}\right)\right)^2 + 4\frac{\rho}{D^{*1}}}\,, \tag{2.45}$$

giving one positive and one negative eigenvalue. Hence, X_1 is always a saddle point.

Thus, we get that X_0 is a stable node for $\sigma \geq \sigma^* = 2\sqrt{D^{*0}\rho}$ and X_1 is a saddle. Therefore, assuming the linear conjecture holds and noting that $D^{*0} = D_0^\infty$ from (2.38), the system exhibits travelling wave solutions with a minimal wave speed of $\sigma^* = 2\sqrt{D_0^\infty \rho}$. □

The analysis for the other cases follows the procedure as used in the proof of Lemma 1. The zero fixed point X_0 was stable under the condition $\sigma > \sigma^* = 2\sqrt{D^{*0}\rho} = 2\sqrt{D_0^\infty \rho}$ in all cases. Although we do not present the full analysis of each case here, we summarize the details for all the cases in Table 2.2 and Table 2.3. Of note is that this wave speed form is very similar to the Fisher equation wave speed, $\sigma = 2\sqrt{D\rho}$ [38]. In the case of the Fisher wave speed, D is always constant. This is true for Bio-case 1, however for Bio-cases 2 and 3, the constant D is replaced with D_0^∞. The implication of this difference is discussed in Section 2.5.1.

2.4 Numerical results

In the following, we present numerical simulations of the glioma model for each biological scenario, where we vary ρ and D. The majority of the results shown will be limited to Mech-case 1 and 3 as we consider these to be the most relevant, representing the base-line mechanical model used previously (linear elasticity) and the mechanical model most closely representing brain tissue *in vivo* (one-term Ogden elasticity with $\alpha = -20$). Furthermore, the results for the remaining Mech-cases closely follow those of Mech-case 1 and 3, and thus presenting full results for each Mech-case would be redundant. Comparisons of results between the mechanical cases are discussed in Section 2.5. The

Table 2.2: Summary of variables and constants in standard coordinates, (x, t), and travelling wave coordinates, $x - \sigma t$, for the different biological cases of the model with linear and Ogden elasticity. The variables indicate terms that are space and time dependent (i.e. have argument (x, t)), while the constants indicate that those values do not change in either space nor time. For the travelling wave coordinate variable, the subscripts correspond to the variables after reduction of order, with $c_0(z) := c(z)$ and $c_1(z) := c'(z)$, where this notation holds for the other variables as well.

Mech-case		1		2, 3, 4	
Coords.	Bio-case	Variable	Constant	Variable	Constant
(x, t)	1	c, u	D, λ, μ	c, u	D, μ
	2	c, u, D	λ, μ	c, u, D	μ
	3	c, u, D, λ, μ		c, u, D, μ	
$x - \sigma t$	1	c_0, c_1, u_0, u_1	D, λ, μ	c_0, c_1, u_0, u_1	D, μ
	2	$c_0, c_1, u_0, u_1,$ D_0, D_1	λ, μ	$c_0, c_1, u_0, u_1,$ D_0, D_1	μ
	3	$c_0, c_1, u_0, u_1,$ D_0, D_1, λ, μ		$c_0, c_1, u_0, u_1,$ D_0, D_1, μ	

Table 2.3: Summary of fixed points and minimum wave speeds for the different biological cases of the model with linear and Ogden elasticity. The notation $X^{*i}, X \in \{D, \mu, \lambda\}$ and $i \in \{0, 1\}$ indicate that any value in the domain may be taken. † indicates the fixed points are the same for the linear and Ogden cases.

Bio-case	Mech-case	Variable vector	
$1^{\dagger}$	1-4	(c_0, c_1, u_0, u_1)	
$2^{\dagger}$	1-4	$(c_0, c_1, D_0, D_1, u_0, u_1)$	
3	1	$(c_0, c_1, D_0, D_1, u_0, u_1, \lambda, \mu)$	
3	2-4	$(c_0, c_1, D_0, D_1, u_0, u_1, \mu)$	
Bio-case	Mech-case	Equilibria	Minimum wave speed
$1^{\dagger}$	1-4	$X_0 = (0, 0, u^{*0}, 0)$	$2\sqrt{D\rho}$
		$X_1 = (1, 0, u^{*1}, 0)$	
$2^{\dagger}$	1-4	$X_0 = (0, 0, D^{*0}, 0, u^{*0}, 0)$	$2\sqrt{D^{*0}\rho}$
		$X_1 = (1, 0, D^{*1}, 0, u^{*1}, 0)$	
3	1	$X_0 = (0, 0, D^{*0}, 0, u^{*0}, 0, \lambda^{*0}, \mu^{*0})$	$2\sqrt{D^{*0}\rho}$
		$X_1 = (1, 0, D^{*1}, 0, u^{*1}, 0, \lambda^{*1}, \mu^{*1})$	
3	2-4	$X_0 = (0, 0, D^{*0}, 0, u^{*0}, 0, \mu^{*0})$	$2\sqrt{D^{*0}\rho}$
		$X_1 = (1, 0, D^{*1}, 0, u^{*1}, 0, \mu^{*1})$	

model system is simulated in MATLAB R2020b. The spatial and temporal domains are discretized homogeneously with space and time steps dx and dt, respectively. For spatial derivatives, finite difference schemes are employed. The time derivatives are estimated using backward time differences. Further details regarding numerical methods are given in the Appendix 2.9.

In the numerical simulations, we set specific units in order to use data for parameters. Space is taken to be in centimeters, cm, while time is in days, d. Therefore, ρ has units $\frac{1}{d}$, D has units $\frac{cm^2}{d}$, λ and μ have units $\frac{kg}{cm\ d^2}$, and η has units $\frac{kg}{cm\ d}$. The cell density is normalized and is therefore unitless.

2.4.1 Parameter values and initial conditions

In all simulations, the initial cell density is taken to be a steep, smooth step function as shown in Figure 2.3.

To simulate the model in Bio-case 1 (with constant material properties), the material properties given by $\mathbf{m}_{\text{Lin}} = (D, \lambda, \mu)$ (for Mech-case 1) and $\mathbf{m}_{\text{Ogd}} = (D, \mu)$ (for Mech-case 2-4) are held constant in both space and time. For the cases when viscosity is included, η is also held constant.

For Bio-case 2, diffusion, $D(x,t)$, is allowed to vary over space and time, while the material parameters, λ, μ, and η, have a constant initial condition and are held constant. The initial diffusion is taken to be a normally distributed band with a peak at $x = 5$, with a base diffusion value outside of this band. The band of higher diffusion values represents a white matter region, while the region with the base value represents gray matter. The form of this distribution is given by

$$D(x,0) = D_{\text{base}} + \frac{D_{\text{base}}}{10} \frac{1}{\sqrt{2\pi(\delta)^2}} e^{\frac{-(x-M)^2}{2(\delta)^2}}, \tag{2.46}$$

where D_{base} is the base diffusion value, $\delta = 1$ is the standard deviation, and $M = \frac{L}{2}$ is the mean (where L is the length of the domain). The scaling factor of $\frac{D_{\text{base}}}{10}$ is used to give a peak diffusion value that is five-fold higher than the base diffusion value, representing the five-fold increase in diffusion rates in white matter over gray matter [119]. The initial diffusion distributions for

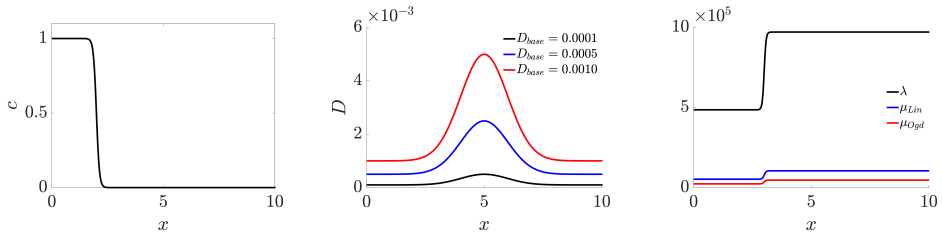

Figure 2.3: Initial condition cell density for all cases (*left*), initial diffusion distributions for Bio-case 2 and Bio-case 3 with base values $D_{\text{base}} = 0.0001, 0.0005, 0.0010$ (*middle*), and initial elasticity parameter distributions for Bio-case 3 (*right*).

each value of D_{base} used in the numerical simulations are shown in Figure 2.3. As the elasticity is constant, the simulations represent tumor growth within a mechanically homogeneous region.

Finally, to simulate Bio-case 3, both the diffusion and elasticity are variable over space and time. The initial diffusion is the same as for Bio-case 2. The initial distribution of the elasticity parameters, λ and μ, is taken to be non-constant in space with the values taking on the standard values (as given in Tables 2.4 and 2.5) from $x = 0$ to $x = 3$, then doubling the base value past $x = 3$. The initial distributions of the elasticity parameters is shown in Figure 2.3. In addition to non-constant initial conditions, the material properties, D, λ and μ, advect and vary in space and time. When viscosity is included, the viscosity coefficient, η, has a constant initial condition, but is also allowed to advect and vary in space and time.

The set of ρ values used were common between the simulations including the linear and one-term Ogden elasticity models. The proliferation rate values were taken to be $\rho \in \{0.05, 0.10, 0.15\ /d\}$ and were chosen in order to explore the model behavior. The base diffusion value of $D = 0.0001$ is referenced from [54] with the five-fold increase at the peak referencing [119]. Larger base diffusion values were also chosen in order to explore model dynamics within a reasonable range of diffusion. The values of the elasticity parameters for linear elasticity, λ and μ, were taken from [54]. The value of μ in the case of one-term Ogden elasticity was taken from [21]. In [21], measurements for the value of μ and η are given for different regions of the brain. From these measurements, we have taken the average to arrive at a biologically realistic

Case	Parameter	Value(s)	Ref.
Bio-case 1	D_{base}	$\{0.0001, 0.0005, 0.0010\ \frac{cm^2}{d}\}$ (constant)	[54]
	λ	$\bar{\lambda} = 6.5 \cdot \kappa_1\ \frac{kg}{cm\ d^2}$ (constant)	[54]
	μ	$\bar{\mu}_{\text{Lin}} = 0.7 \cdot \kappa_1\ \frac{kg}{cm\ d^2}$ (constant)	[54]
	η	$\bar{\eta} = 141.66 \cdot \kappa_2\ \frac{kg}{cm\ d}$ (constant)	[21]
Bio-case 2	D_{base}	$\{0.0001, 0.0005, 0.0010\ \frac{cm^2}{d}\}$ (initial)	[54]
	λ	$\bar{\lambda} = 6.5 \cdot \kappa_1\ \frac{kg}{cm\ d^2}$ (constant)	[54]
	μ	$\bar{\mu}_{\text{Lin}} = 0.7 \cdot \kappa_1\ \frac{kg}{cm\ d^2}$ (constant)	[54]
	η	$\bar{\eta} = 141.66 \cdot \kappa_2\ \frac{kg}{cm\ d}$ (constant)	[21]
Bio-case 3	D_{base}	$\{0.0001, 0.0005, 0.0010\ \frac{cm^2}{d}\}$ (initial)	[54]
	λ	as in Figure 2.3 (initial)	[54]
	μ	as in Figure 2.3 (initial)	[54]
	η	$\bar{\eta} = 141.66 \cdot \kappa_2\ \frac{kg}{cm\ d}$ (initial)	[21]

Table 2.4: Material parameter values and initial conditions for Mech-case 1 and each Bio-case. Note that $\kappa_1 = 74,649.6 \frac{kg}{cm\ d^2}$ and $\kappa_2 = 74,649.6 \cdot \frac{1}{24 \cdot 60 \cdot 60} \frac{kg}{cm\ d}$ are conversion factors (see Appendix 2.7).

value. A summary of the material parameters and initial conditions for the linear and one-term Ogden elasticity versions of the glioma model are given in Tables 2.4 and 2.5, respectively.

Note that for the Lamé parameters $\bar{\lambda}_{\text{Lin}}$ and $\bar{\mu}_{\text{Lin}}$ given by (2.4), the three-dimensional version of the linear dynamics given by (2.31) gives $T_{11} = 2.90\mu_{\text{Lin}}u_x$, which is very close to the incompressible case $T_{11} = 3\mu_{\text{Lin}}u_x$. We thus present only the results of the 1D deformation case, *i.e.*, Case 1 given by (2.10), as well as the incompressible case, as the results given by the effective 1D stress of the compressible case (2.31) are practically indistinguishable from those of the incompressible case given by (2.29).

For conciseness of notation, we will denote the initial parameter values as $\bar{\lambda} = 6.5 \cdot \kappa_1\ \frac{kg}{cm\ d^2}$, $\bar{\mu}_{\text{Lin}} = 0.7 \cdot \kappa_1\ \frac{kg}{cm\ d^2}$, $\bar{\mu}_{\text{Ogd}} = 0.3125 \cdot \kappa_1\ \frac{kg}{cm\ d^2}$ and $\bar{\eta} = 141.66 \cdot \kappa_1\ \frac{kg}{cm\ d}$. Using (2.27) we conclude that these values of μ and λ for the linear case correspond to the value of Poisson ratio $\nu \sim 0.451$. Since

Case	Parameter	Value(s)	Ref.
Bio-case 1	D_{base}	$\{0.0001, 0.0005, 0.0010\ \frac{cm^2}{d}\}$ (constant)	[54]
	μ	$\bar{\mu}_{\text{Ogd}} = 0.3125 \cdot \kappa_1\ \frac{kg}{cm\ d^2}$ (constant)	[21]
	η	$\bar{\eta} = 141.66 \cdot \kappa_2\ \frac{kg}{cm\ d}$ (constant)	[21]
Bio-case 2	D_{base}	$\{0.0001, 0.0005, 0.0010\ \frac{cm^2}{d}\}$ (initial)	[54]
	μ	$\bar{\mu}_{\text{Ogd}} = 0.3125 \cdot \kappa_1\ \frac{kg}{cm\ d^2}$ (constant)	[21]
	η	$\bar{\eta} = 141.66 \cdot \kappa_2\ \frac{kg}{cm\ d}$ (constant)	[21]
Bio-case 3	D_{base}	$\{0.0001, 0.0005, 0.0010\ \frac{cm^2}{d}\}$ (initial)	[54]
	μ	as in Figure 2.3 (initial)	[21]
	η	$\bar{\eta} = 141.66 \cdot \kappa_2\ \frac{kg}{cm\ d}$ (initial)	[21]

Table 2.5: Material parameter values and initial conditions for Mech-case 2-4 and each Bio-case.

$\nu = 0.5$ in the incompressible case, the values of Lamé parameters taken in our simulation correspond closely to the almost incompressible case, similar to the materials such as saturated clay [107].

As our main interest are the wave profiles of the cell density, we present the cell density plots for each set of simulations, omitting the plots of other components of the model. However, representative plots for the other components are also given for clarity of initial conditions and general dynamics.

2.4.2 Bio-case 1

Mech-case 1 and Bio-case 1. The representative dynamics and cell density plots for Mech-case 1 (linear elastic model) with constant material properties are given in Figures 2.4 and 2.5. Note that the bulk modulus is omitted from the representative dynamics figures throughout the numerical results as the behavior is the same as the shear modulus.

Because the initial cell density is a fairly steep step profile, it takes a bit of time for the wave profile to be established. After that time, a stable travelling wave is formed. As is expected from the analytical results, increasing either

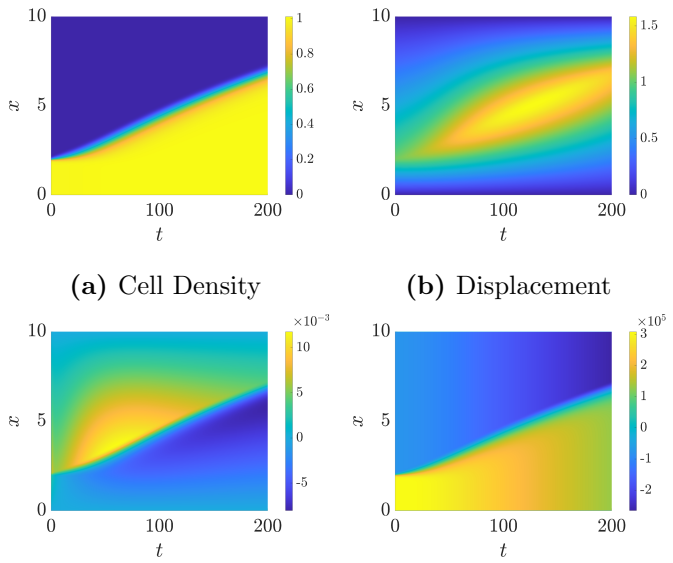

(a) Cell Density **(b)** Displacement

(c) Velocity **(d)** Stress

Figure 2.4: Representative dynamics of model components of the model for Biocase 1 with Mech-case 1. For this simulation, $\rho = 0.15$ and $\mathbf{m}_{\text{Lin}} = (0.0005, \bar{\lambda}, \bar{\mu}_{\text{Lin}})$. The plots for D, λ, and μ are omitted as they are constant.

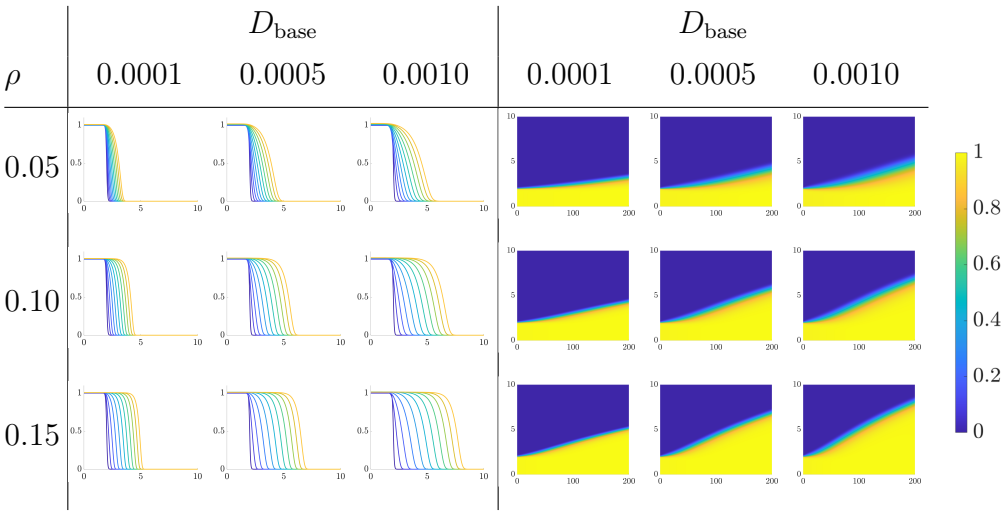

Figure 2.5: Wave profile (*left*) and cell density (*right*) plots of the model for Biocase 1 with Mech-case 1 where $\lambda = \bar{\lambda}$ and $\mu = \bar{\mu}_{\text{Lin}}$. For each panel of the wave profile plots, space (x) is on the x-axis and cell density (c) is on the y-axis. For each panel of the cell density plots, time (t) is on the x-axis and space (x) is on the y-axis. Values of ρ and D used in simulations are indicated on the axes.

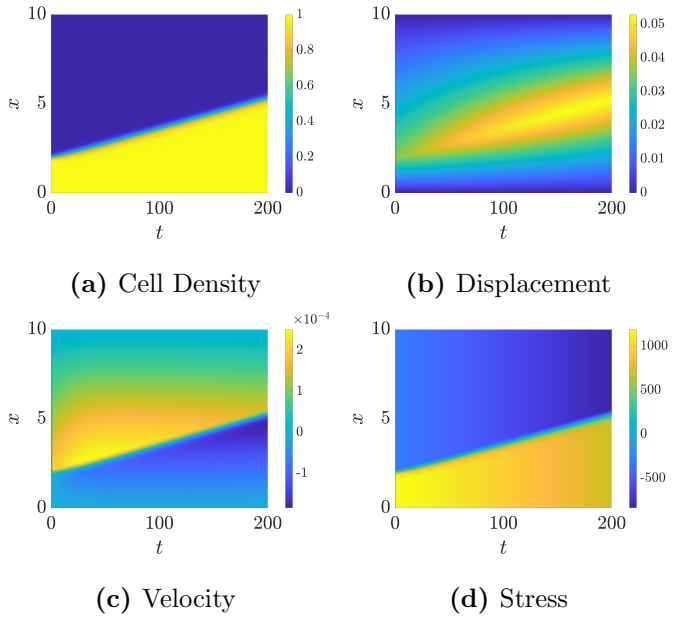

(a) Cell Density **(b)** Displacement

(c) Velocity **(d)** Stress

Figure 2.6: Representative dynamics of model components for the model for Bio-case 1 with Mech-case 3. For this simulation, $\rho = 0.15$ and $\mathbf{m}_{\text{Ogd}} = (0.0005, \bar{\mu}_{\text{Ogd}})$. The plots for D and μ are omitted as they are constant.

ρ and/or D increases the wave speed. In Table 2.6, we list the theoretical wave speed $2\sqrt{\rho D}$ and the simulated wave speed, where we used the last 25 time steps to estimate the wave speed. There is a fair agreement between the analytical and simulated wave speeds for the linear elasticity case, with the discrepancy caused by the time it takes for the cell density to settle into the wave form. The delay in wave establishment is not unexpected as this is a standard property of travelling waves. As the values of ρ and D increase, the cell density reaches the wave form faster, resulting in the simulated wave speeds being closer to the analytical wave speed for larger ρ and D values.

Mech-case 3 and Bio-case 1. The representative dynamics and cell density plots for Mech-case 3 (one-term Ogden elastic model with $\alpha = -20$) with constant material properties are given in Figures 2.6 and 2.7.

The numerical simulation results do not differ greatly when compared to the respective simulations with the linear elasticity model. Comparisons of the effects of each mechanical model on the full glioma model are discussed in later

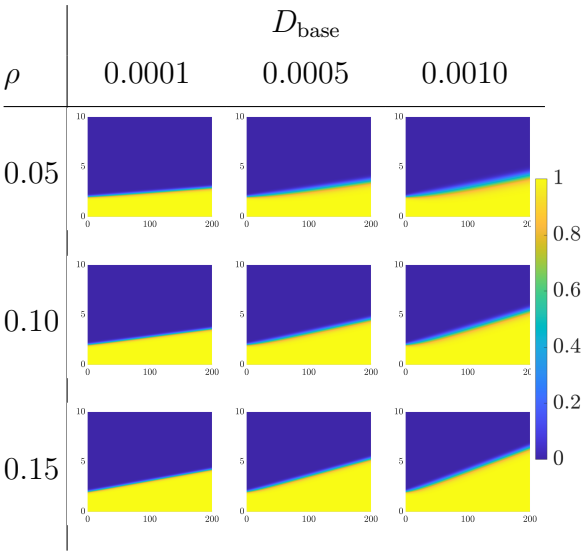

Figure 2.7: Cell density plots for the model for Bio-case 1 with Mech-case 3 where $\mu = \bar{\mu}_{\text{Ogd}}$. Each panel has time ($t$) on the x-axis and space (x) on the y-axis. Values of ρ and D used in simulations are indicated on the axes.

sections (see Section 2.5). Analysis showed that a travelling wave is expected in our model. This result is supported by the simulations with travelling waves occurring across multiple parameter combinations. As with linear elasticity, we again see that some time is required for the wave to establish from the steep initial cell density profile with the wave front initially spreading before taking a stable form. The analysis also resulted in a wave speed of $\sigma^* = 2\sqrt{D\rho}$ which is closely matched in all the simulations presented as noted in Table 2.6. Also reflected in the simulations is that increasing either ρ and/or D results in a faster wave speed, as was indicated by the derived wave speed.

Viscoelastic models and Bio-case 1. In Figure 2.8, the cell density and displacement for the Mech-case 1 and Mech-case 3 with constant material properties is compared with the corresponding viscoelastic versions of each model. It is clear from the figures that the addition of the viscosity term did not significantly affect either the shape or speed of the tumor cell density wave, nor the resulting displacement. With no significant differences observed with the addition of a viscoelastic term for Mech-case 1 and 3, we did not simulate viscoelastic versions for Mech-case 2 or 4.

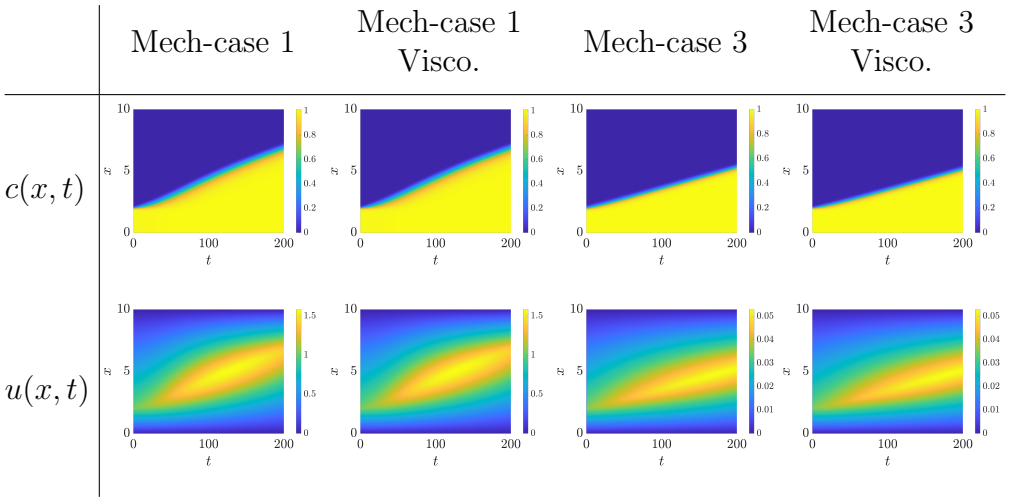

Figure 2.8: Comparison of cell density and displacement for the model for Bio-case 1 with Mech-case 1/Mech-case 3 and Mech-case 1/Mech-case 3 viscoelastic models where $\rho = 0.15$, $\mathbf{m}_{\text{Lin}} = (D, \lambda, \mu) = (0.0005, \bar{\lambda}, \bar{\mu}_{\text{Lin}})$, $\mathbf{m}_{\text{Ogd}} = (D, \mu) = (0.0005, \bar{\mu}_{\text{Ogd}})$, and $\eta = \bar{\eta}$.

We explored if the lack of change with added viscosity was purely due to the size of the viscosity coefficient used by considering much smaller and much larger, biologically unrealistic, values of η. Multiplying η by the factors 0.01, 0.1, 10, and 100 resulted in a slight difference at the beginning of simulations, with more notable changes occurring in the linear viscoelasticity case than in the Ogden case. However, for both viscoelastic models the effects of the extreme viscosity values were transient and did not affect the dynamics later in the simulation, with the wave profile and speed reverting to the non-viscous case following this transient period. Thus, there can be a minimal and transient difference by adding viscosity, but it can only occur at unreasonably large values of η and does not affect the longer term dynamics.

Wave speeds for Bio-case 1. For the glioma model in Bio-case 1, Table 2.6 presents the numerical wave speeds for each of the four mechanical models. There is good agreement between the analytical and numerically calculated wave speeds in all cases. The wave speed results are discussed in Section 2.5.1.

Table 2.6: Wave speeds with each mechanical model in Bio-case 1. $\downarrow/\uparrow$ indicates that the simulated value was lower/higher than the analytically calculated value. For all calculations, the wave speed was calculated starting at $t = 175$ until the end of simulation time. For the Ogden cases, $\alpha = -20$, and for the viscoelastic cases, $\eta = \bar{\eta}$. Note that the values Mech-case 1 and Mech-case 1 Visco. are the same. The values for the Mech-case 3 viscoelastic cases are the same for both T_{OgdV} and T_{OgdV2} except for those marked with *, which are 0.001 smaller in T_{OgdV2} case.

ρ	D	Analytical	Mech-case				3
			1	2	3	4	3, Visco.
0.05	0.0001	0.004	$0.008^{\uparrow}$	$0.006^{\uparrow}$	$0.005^{\uparrow}$	$0.005^{\uparrow}$	0.004
	0.0005	0.010	$0.015^{\uparrow}$	$0.011^{\uparrow}$	0.010	$0.009^{\downarrow}$	$0.009^{\downarrow}$
	0.001	0.014	$0.019^{\uparrow}$	$0.015^{\uparrow}$	$0.013^{\downarrow}$	$0.013^{\downarrow}$	$0.013^{\downarrow}$
0.10	0.0001	0.006	$0.012^{\uparrow}$	$0.010^{\uparrow}$	$0.008^{\uparrow}$	$0.008^{\uparrow}$	$0.007^{\uparrow}$
	0.0005	0.014	$0.020^{\uparrow}$	$0.016^{\uparrow}$	0.014	0.014	0.014^{*}
	0.0010	0.020	$0.024^{\uparrow}$	$0.021^{\uparrow}$	0.020	$0.019^{\downarrow}$	$0.019^{\downarrow}$
0.15	0.0001	0.008	$0.014^{\uparrow}$	$0.013^{\uparrow}$	$0.011^{\uparrow}$	$0.011^{\uparrow}$	0.008
	0.0005	0.017	$0.022^{\uparrow}$	$0.019^{\uparrow}$	$0.018^{\uparrow}$	0.017	0.017
	0.0010	0.024	$0.027^{\uparrow}$	$0.026^{\uparrow}$	0.024	$0.023^{\downarrow}$	0.024^{*}

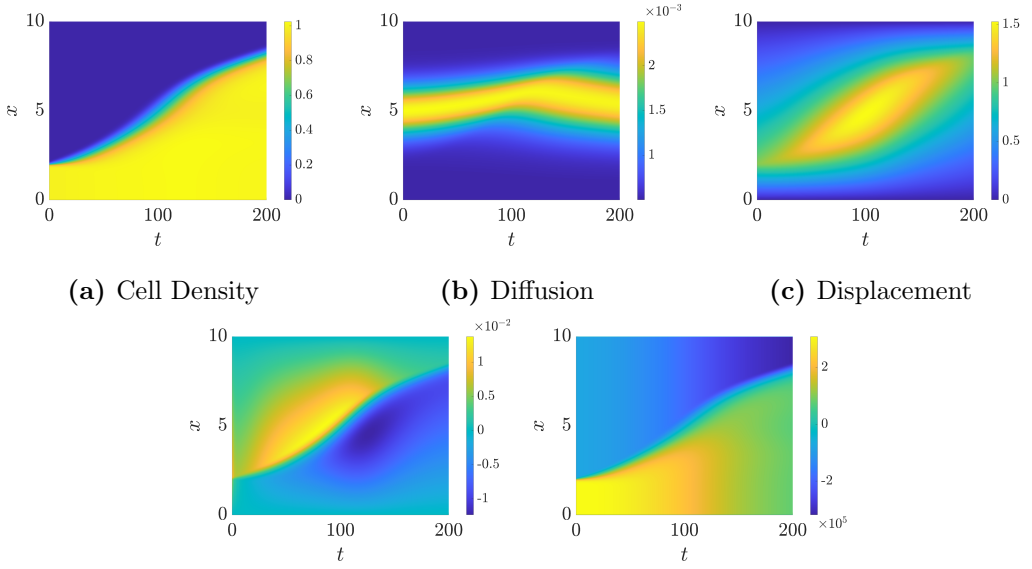

(a) Cell Density **(b)** Diffusion **(c)** Displacement

(d) Velocity **(e)** Stress

Figure 2.9: Representative dynamics of model components for the model for Bio-case 2 with Mech-case 1. For this simulation, $\rho = 0.15$, $D_{\text{base}} = 0.0005$, $\lambda = \bar{\lambda}$, and $\mu = \bar{\mu}_{\text{Lin}}$. The plots for λ and μ are omitted as they are constant.

2.4.3 Bio-case 2

Mech-case 1 and Bio-case 2. The representative dynamics and cell density plots for the linear elastic model with variable diffusion and constant elastic properties are given in Figures 2.9 and 2.10.

In agreement with the travelling wave analysis, we consistently see attenuated waves in the simulations. As the cell density "wave" front passes through the region with higher diffusion, the front is dispersed by the higher speed. After the front reaches the other side of the increased diffusion, the width of the front compresses and the slower wave is reestablished as the diffusion returns to a constant value. This can be interpreted as the edge of a tumor mass, previously positioned entirely within gray matter (low diffusion), encountering a white matter region (high diffusion). The tumor cells at the front boundary of the tumor migrate faster across the white matter than the cells still within the gray matter. This difference in migration causes a decreased density of tumor cells at the front of the tumor, as shown by the decreased cell density in the

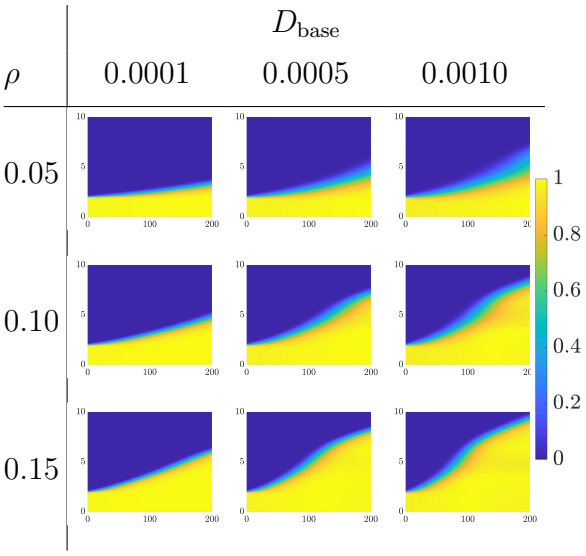

Figure 2.10: Cell density plots for the model for Bio-case 2 with Mech-case 1 where $\lambda = \bar{\lambda}$ and $\mu = \bar{\mu}_{\text{Lin}}$. Each panel has time ($t$) on the x-axis and space (x) on the y-axis. Values of ρ and D_{base} used in simulations are indicated on the axes.

wave profile figures. Once the front reaches the other side of the white matter region and enters the gray matter, the cells at the front slow their migration, causing the cell front to become more dense.

Mech-case 3 and Bio-case 2. The representative dynamics and cell density plots for the one-term Ogden elastic model (with $\alpha = -20$) with variable diffusion and constant elastic properties are given in Figures 2.11 and 2.12.

The cell density behavior agrees with the wave speed analysis and is similar to that with linear elasticity, with the cell density forming a wave which increases speed as ρ or D_{base} increases, or as the cells pass through a region of increased diffusion. However, as can be clearly seen in the diffusion panel, the deformation is much smaller with Ogden elasticity compared to linear elasticity, with the diffusion changing imperceptibly over time (it was numerically confirmed that the diffusion did change in time).

Viscoelastic models and Bio-case 2. We also compare the corresponding viscoelastic models for Bio-case 2. Again, we see essentially no difference between the elastic and the viscoelastic versions (simulations not shown).

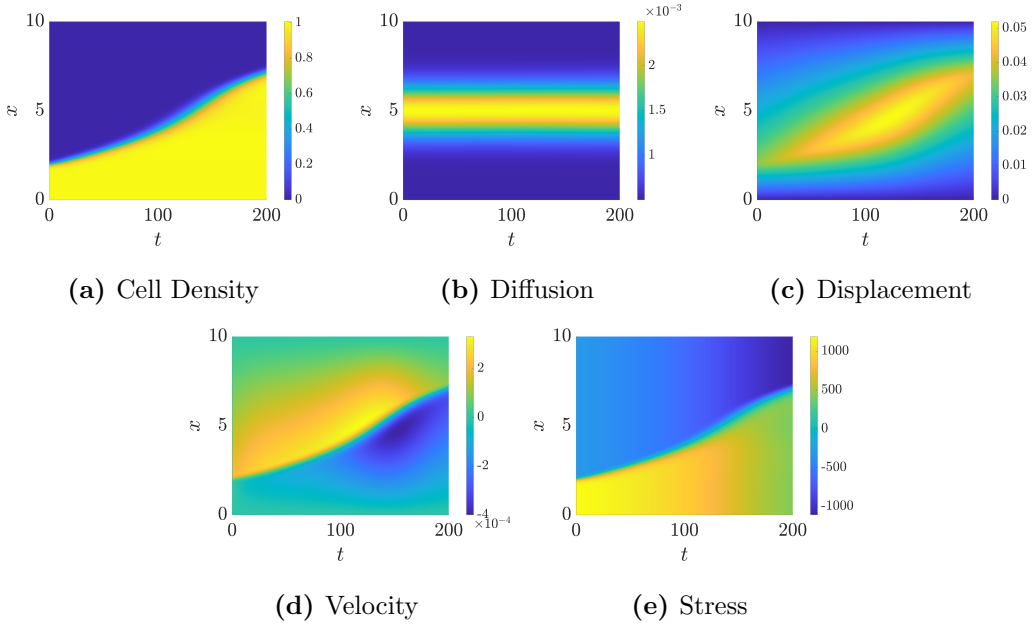

(a) Cell Density **(b)** Diffusion **(c)** Displacement

(d) Velocity **(e)** Stress

Figure 2.11: Representative dynamics of model components for the model for Bio-case 2 with Mech-case 3 where $\mu = \bar{\mu}_{\text{Ogd}}$. For this simulation, $\rho = 0.15$ and $D_{\text{base}} = 0.0005$. The plot for μ is omitted as it is constant.

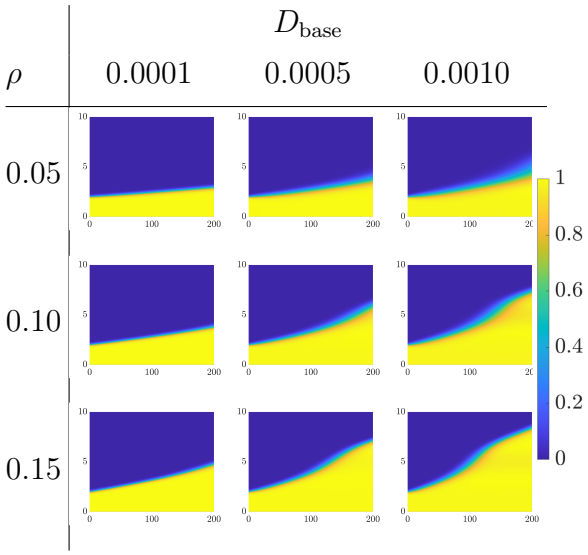

Figure 2.12: Cell density plots for the model for Bio-case 2 with Mech-case 3 where $\mu = \bar{\mu}_{\text{Ogd}}$. Each panel has time ($t$) on the x-axis and space (x) on the y-axis. Values of ρ and D_{base} used in simulations are indicated on the axes.

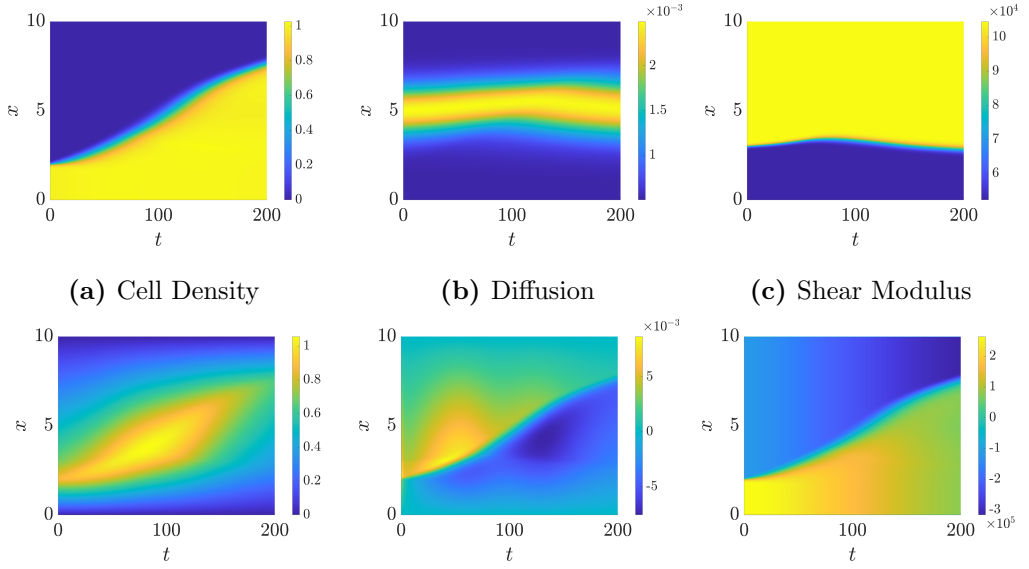

Figure 2.13: Representative dynamics of model components for the model for Bio-case 3 with Mech-case 1. For this simulation, $\rho = 0.15$, $D_{\text{base}} = 0.0005$, with the initial distributions of λ and μ as shown in Figure 2.3.

2.4.4 Bio-case 3

Mech-case 1 and Bio-case 3. The representative dynamics and cell density plots for the linear elastic model with variable material properties are given in Figures 2.13 and 2.14.

Once again, the cell density moves as a wave, increasing the spread speed with increased ρ, D_{base}, and over the region with increased diffusion. In agreement with the analysis, the introduction of variable material parameters does not eliminate the existence of a cell density wave and does not change the wave speed. With the introduction of a spatially varying initial condition for the shear modulus, μ, (as well as λ, not shown), there is clear deformation of μ (and λ) over time.

Mech-case 3 and Bio-case 3. The representative dynamics and cell density plots for the one-term Ogden elastic model (with $\alpha = -20$) with variable material properties are given in Figures 2.15 and 2.16.

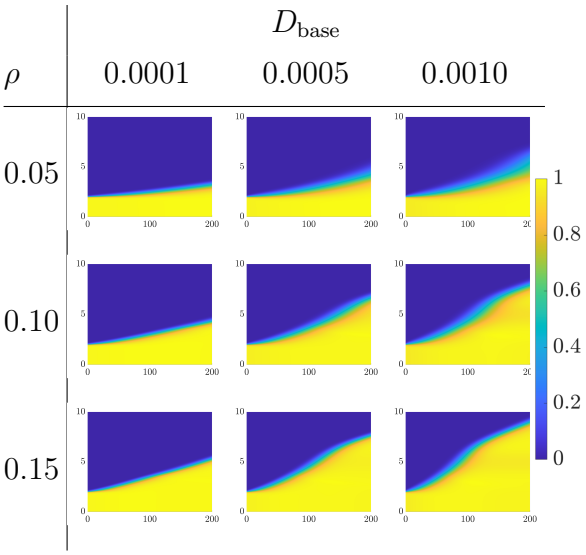

Figure 2.14: Cell density plots for the model for Bio-case 3 with Mech-case 1 with the initial distributions of λ and μ as shown in Figure 2.3. Each panel has time (t) on the x-axis and space (x) on the y-axis. Values of ρ and D_{base} used in simulations are indicated on the axes.

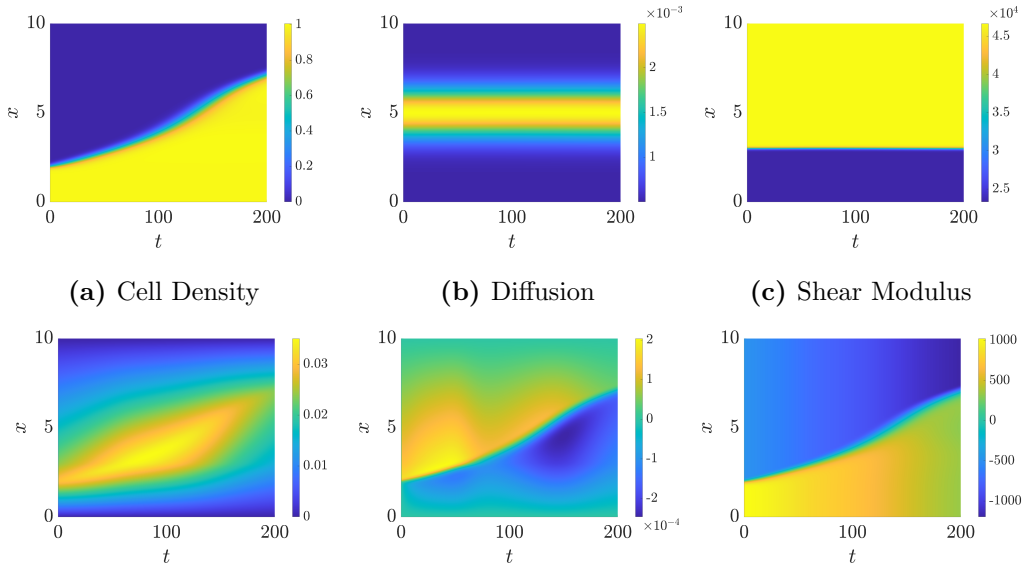

(a) Cell Density **(b)** Diffusion **(c)** Shear Modulus

(d) Displacement **(e)** Velocity **(f)** Stress

Figure 2.15: Representative dynamics of model components for the model for Bio-case 3 with Mech-case 3. For this simulation, $\rho = 0.15$, $D_{\text{base}} = 0.0005$, with the initial distribution of μ as shown in Figure 2.3.

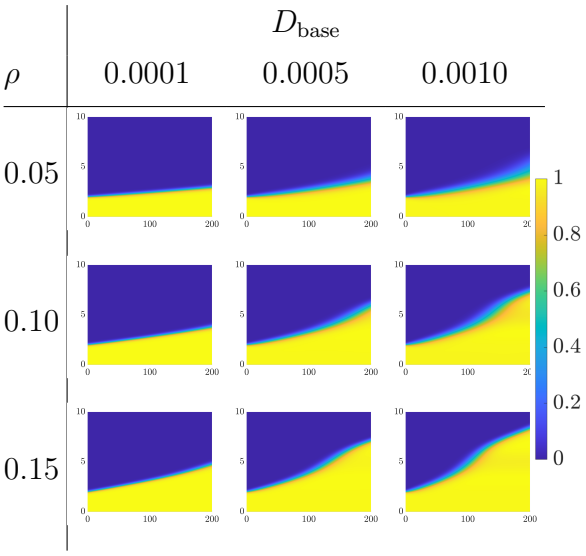

Figure 2.16: Cell density plots for the model for Bio-case 3 with Mech-case 3, with the initial distribution of μ as shown in Figure 2.3. Each panel has time (t) on the x-axis and space (x) on the y-axis. Values of ρ and D_{base} used in simulations are indicated on the axes.

As in the previous Bio-cases, the behavior of the cell density of the glioma model with Ogden elasticity is similar to that with linear elasticity. Also, similar to Bio-case 2, the deformation of the material properties (i.e. D, μ) is smaller in the Ogden case.

Viscoelastic models and Bio-case 3. As with the results in the constant material case, the addition of a viscosity term seems to have little to no affect on the model (simulations not shown).

2.5 Model comparison

2.5.1 Comparison of mechanical models

Wave speed and wave front. The analysis shows that the three main elasticity models (Mech-case 1 (2.10), Mech-case 2 (2.12), Mech-cases 3,4 (2.13)) included here result in the same analytically derived wave speed of $\sigma^* = 2\sqrt{D\rho}$. At first this may be a surprising result as one may think that the mechanical

dynamics of a substrate through which a wave is travelling will certainly affect the speed of that wave. However, the wave is a pulled wave and the speed only depends on the dynamics at the immediate front of the wave. At the leading edge of the wave, the cell density is very low, the deformation is minimal, and the wave front does not experience significant deformation at the front. However, simulations show that the shape of the wave front is steeper with Mech-case 3 than with Mech-case 1, while the Mech-case 2 results in an intermediate wave front that is shallower than that for Mech-case 3 but sharper than Mech-case 1. It can be seen in Figure 2.17 that the wave front in Mech-case 1 is more diffuse, that is, there is a larger region of intermediate density at wave front, than Mech-case 3. This can also be seen in Figure 2.18 where the wave fronts for Mech-case 3 (dashed lines) have a steeper step than Mech-case 2 (dotted lines), which are then steeper than for Mech-case 1 (solid lines). We also note that the wave profile plots for Mech-case 4 are nearly identical to Mech-case 3 and are thus not included in Figures 2.17 and 2.18. Although we did not analytically determine the shapes of the wave fronts, it is clear that the linear cases have generally more diffuse, shallow wave fronts. The linear model gives higher values of displacements, allowing the cells at the front of the wave to spread further than in either the linear incompressible or Ogden case.

In Bio-cases 2 and 3 the diffusion coefficient changes. Hence the wave speed also changes over space and time. Still, it roughly follows the speed $2\sqrt{D(x,t)\rho}$, which can be understood as instantaneous speed at a given location. Once the area of higher diffusion is passed, the wave relaxes back to a constant wave speed that corresponds to the base diffusion value.

Mechanical comparisons. It is also worth exploring how the mechanical factors such as deformation and stress that underlie the difference in cell dynamics compare. We begin by considering displacement, u, as shown in Figure 2.19. We note that there is two orders of magnitude difference in the displacement between Mech-case 1 and Mech-case 3. With the parameters used here, the displacement is on the order of 10^0, 10^{-1}, 10^{-2}, and 10^{-1} in the linear, linear incompressible, Ogden with $\alpha = -20$, and Ogden with $\alpha = -7.3$ cases,

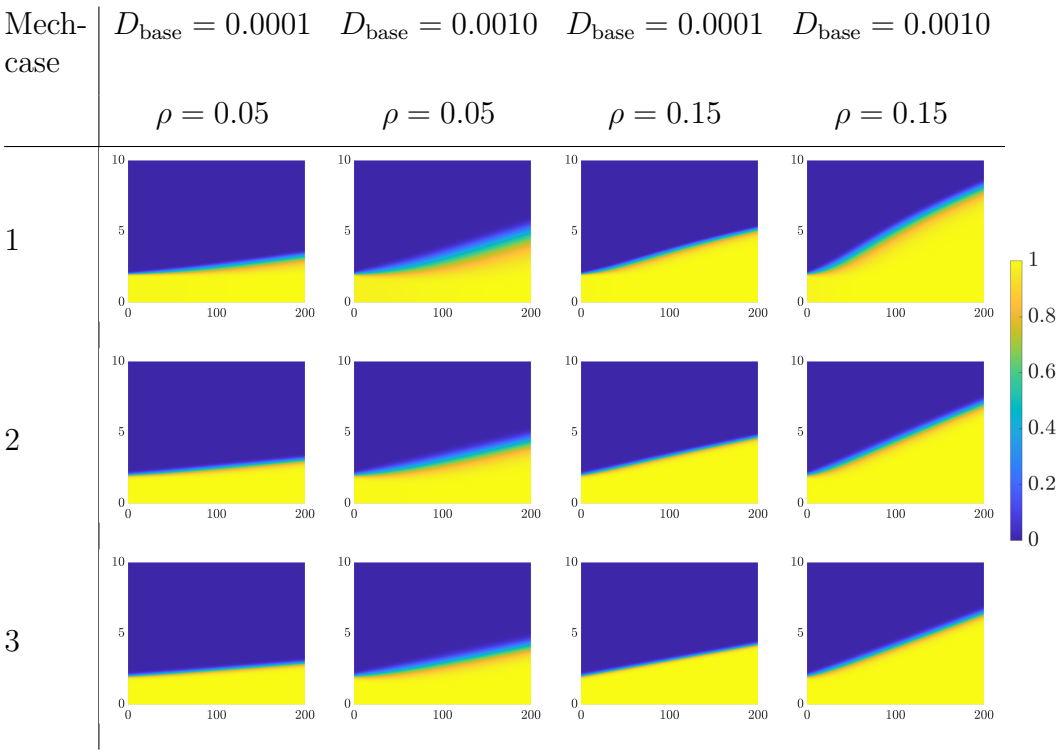

Figure 2.17: Cell density plots for Mech-case 1 (where $\lambda = \bar{\lambda}$, $\mu = \bar{\mu}_{\text{Lin}}$), Mech-case 2 (where $\mu = \bar{\mu}_{\text{Ogd}}$), and Mech-case 3 (where $\mu = \bar{\mu}_{\text{Ogd}}$) in Bio-case 1. Each panel has time (t) on the x-axis and space (x) on the y-axis. Values of ρ and D_{base} are as indicated.

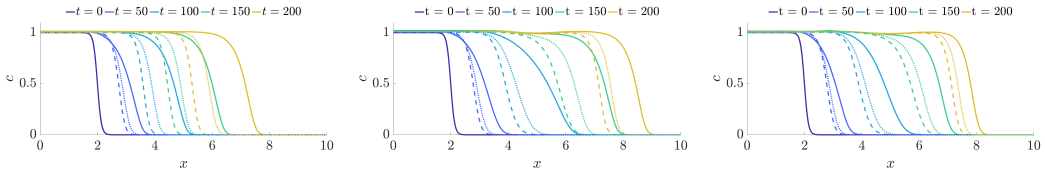

Figure 2.18: Wave profile plots at $t = 0, 50, 100, 150, 200$ for Mech-case 1 *(solid)*, Mech-case 2 *(dot)*, and Mech-case 3 *(dash)* with $\rho = 0.15$ and $D = 0.0005$ (or $D_{\text{base}} = 0.0005$, when applicable) for Bio-case 1 *(left)*, Bio-case 2 *(middle)*, and Bio-case 3 *(right)*.

Table 2.7: Ranges of $u(x,t)$ and stress for each Mech-case and Bio-case where $D = 0.0005$ (or $D_{\text{base}} = 0.0005$, when applicable) and $\rho = 0.15$. For Bio-case 1 and Bio-case 2, $\lambda = \bar{\lambda}$ and $\mu = \bar{\mu}_{\text{Lin}}$ for Mech-case 1 and $\mu = \bar{\mu}_{\text{Ogd}}$ for the remaining Mech-cases. In Bio-case 3, the initial distributions of λ and μ are as shown in Figure 2.3.

Bio-case	Mech-case	1	2
1	$u(x,t)$	$[0, 1.58]$	$[0, 0.529]$
	Stress	$[-2.74, 3.11] \times 10^5$	$[-7.95 \times 10^4, 1.08 \times 10^5]$
2	$u(x,t)$	$[0, 1.52]$	$[0, 0.515]$
	Stress	$[-3.23, 3.11] \times 10^5$	$[-1.02, 1.08] \times 10^5$
3	$u(x,t)$	$[0, 1.06]$	$[0, 0.351]$
	Stress	$[-3.21, 2.69] \times 10^5$	$[-1.09 \times 10^5, 9.51 \times 10^4]$
Bio-case	Mech-case	3	4
1	$u(x,t)$	$[0, 0.053]$	$[0, 0.145]$
	Stress	$[-8.35 \times 10^2, 1.19 \times 10^3]$	$[-2.34, 3.26] \times 10^3$
2	$u(x,t)$	$[0, 0.052]$	$[0, 0.142]$
	Stress	$[-1.11, 1.19] \times 10^3$	$[-3.06, 3.27] \times 10^3$
3	$u(x,t)$	$[0, 0.035]$	$[0, 0.096]$
	Stress	$[-1.20, 1.02] \times 10^3$	$[3.28, 2.81] \times 10^3$

respectively. Although we show only one combination of ρ and D/D_{base}, the difference in scale of displacement between elasticity models is conserved for the other combinations of parameters used previously. This disparity in scale carries through in the stress, with the stress being on the order of 10^5 for linear elasticity, 10^4 for linear incompressible elasticity, 10^2 for Ogden elasticity with $\alpha = -20$, and 10^3 for Ogden elasticity with $\alpha = -7.3$, as shown in Figure 2.20 and Table 2.7. As illustrated in Figure 2.2, significant differences in stress can be expected between the elasticity models if the gradient of the displacement shows large differences. Figure 2.21 shows u_x as a function of x for a given set of parameters for each elastic model in Bio-case 1.

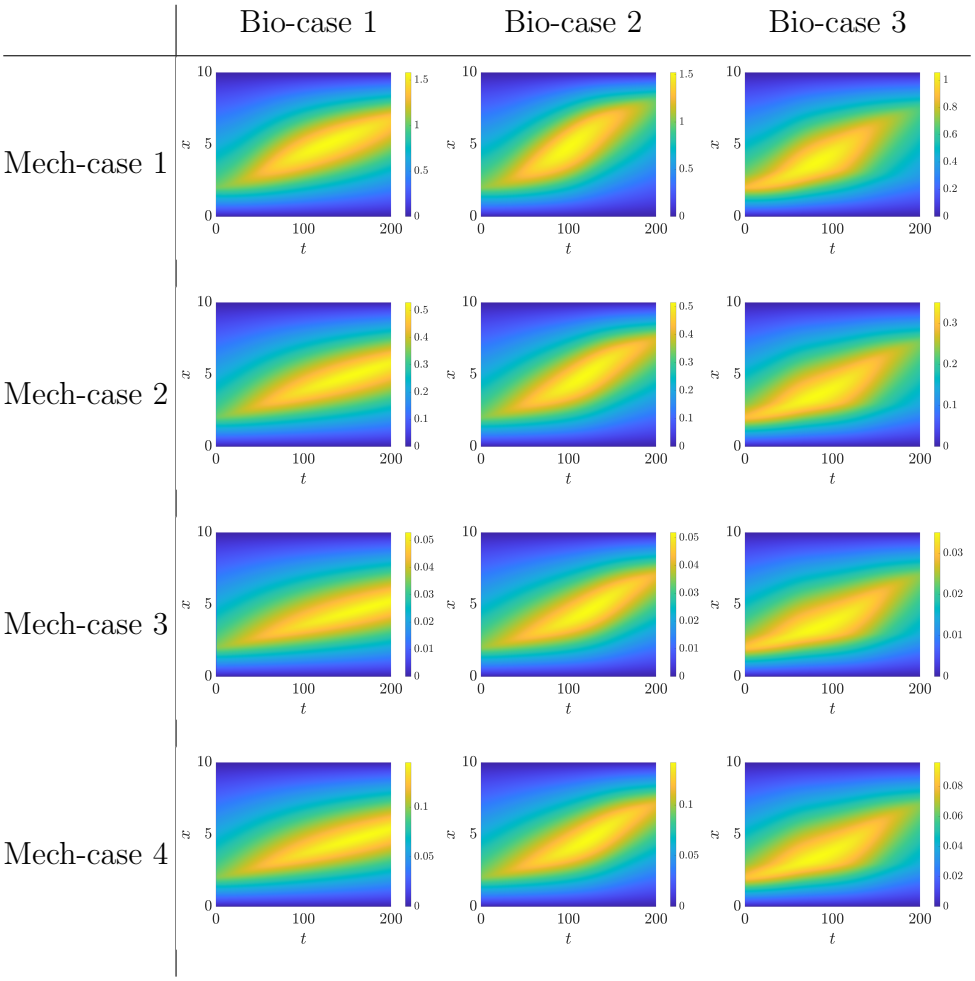

Figure 2.19: Displacement plots for each Mech-case and Bio-case where $D = 0.0005$ (or $D_{\text{base}} = 0.0005$, when applicable) and $\rho = 0.15$. For Bio-case 1 and Bio-case 2, $\lambda = \bar{\lambda}$ and $\mu = \bar{\mu}_{\text{Lin}}$ for Mech-case 1 and $\mu = \bar{\mu}_{\text{Ogd}}$ for the remaining Mech-cases. In Bio-case 3, the initial distributions of λ and μ are as shown in Figure 2.3.

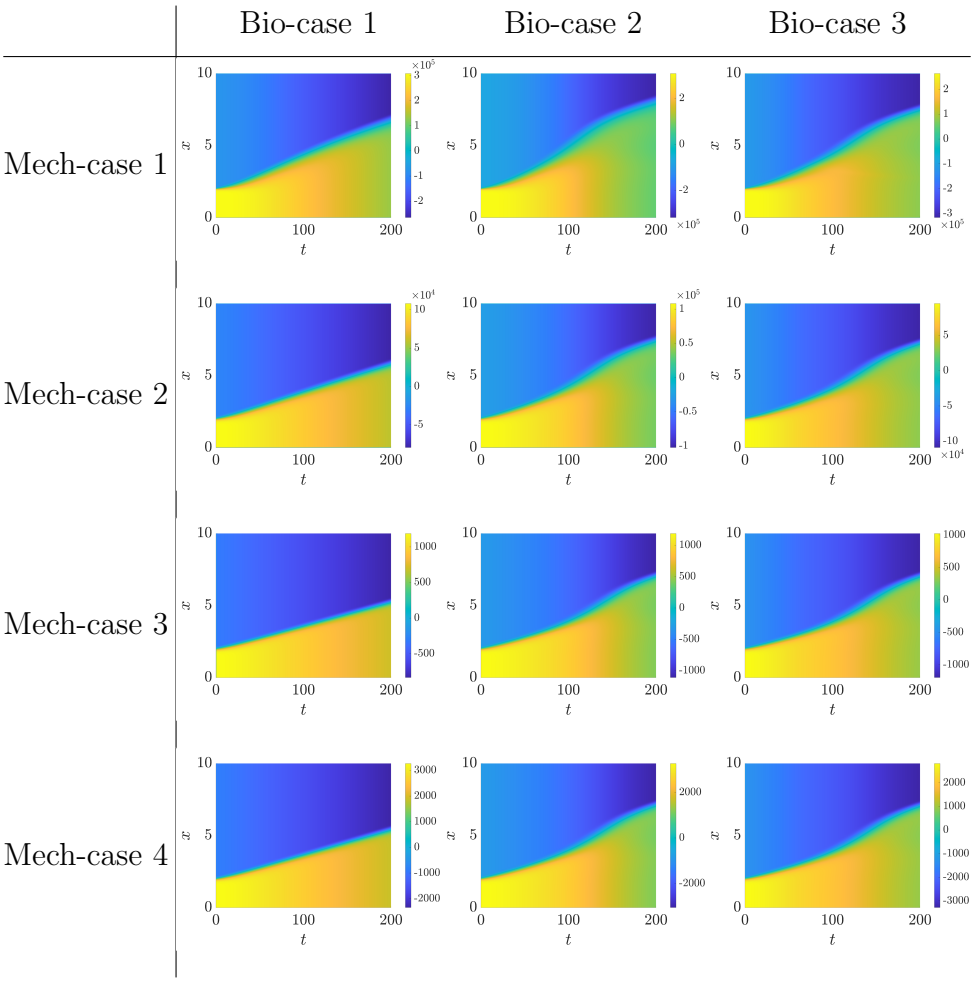

Figure 2.20: Stress plots for each Mech-case and Bio-case where $D = 0.0005$ (or $D_{\text{base}} = 0.0005$, when applicable) and $\rho = 0.15$. For Bio-case 1 and Bio-case 2, $\lambda = \bar{\lambda}$ and $\mu = \bar{\mu}_{\text{Lin}}$ for Mech-case 1 and $\mu = \bar{\mu}_{\text{Ogd}}$ for the remaining Mech-cases. In Bio-case 3, the initial distributions of λ and μ are as shown in Figure 2.3.

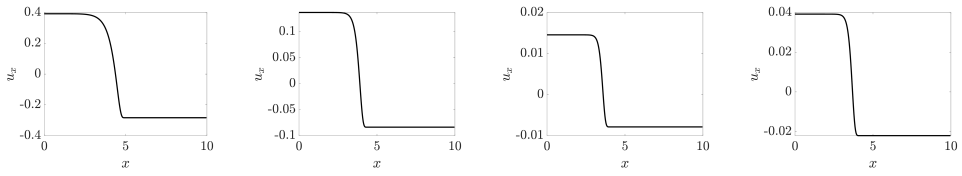

Figure 2.21: Plots of the spatial derivative of displacement, u_x, at time $t = 100$ for Bio-case 1 (where $\rho = 0.15$) with each Mech-case. *Left to right:* Mech-case 1 ($\mathbf{m}_{\text{Lin}} = (D, \lambda, \mu) = (0.0005, \bar{\lambda}, \bar{\mu}_{\text{Lin}})$), Mech-case 2 ($\mathbf{m} = (D, \mu) = (0.0005, \bar{\mu}_{\text{Ogd}})$), Mech-case 3 and 4 ($\mathbf{m}_{\text{Ogd}} = (D, \mu) = (0.0005, \bar{\mu}_{\text{Ogd}})$).

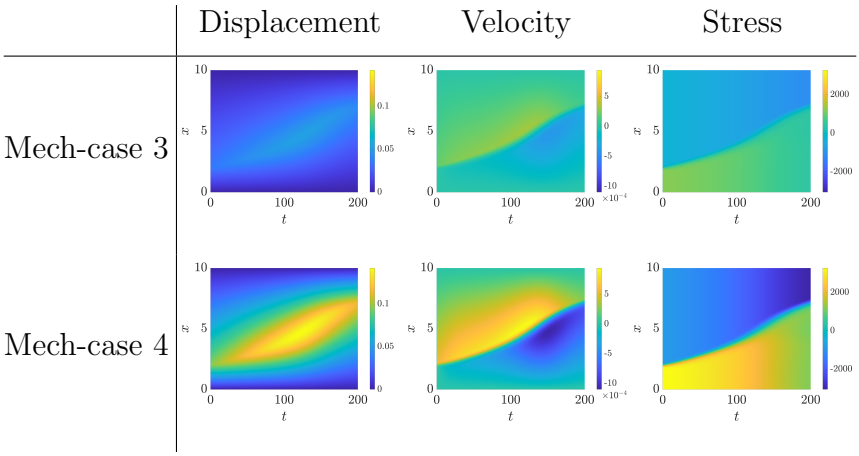

Figure 2.22: Comparison of displacement, velocity, and stress in Bio-case 2 with Mech-case 3 and 4, where $\rho = 0.15$, $\mu = \bar{\mu}_{\text{Ogd}}$, and $D = 0.0005$ (or $D_{\text{base}} = 0.0005$, when applicable).

Comparison of Mech-case 3 and 4. As noted in Section 2.2.2, Budday *et al.* [18] determined two values for the exponent in the one-term Ogden model, noting that the value determined under combined loading modes ($\alpha = -20$) is more likely to realistically represent the situation of a glioma growing in the brain. Although $\alpha = -20$ is likely more realistic for our purposes, for completeness we explore the differences that result between the Ogden models with $\alpha = -20$ (Mech-case 3) and $\alpha = -7.3$ (Mech-case 4).

Figure 2.22 compares the displacement, velocity, and stress between Mech-case 3 and 4 for each biological scenario. The scales for each metric are held constant in order to emphasize the differences between cases. The qualitative behavior (i.e. surface shape) is similar between the cases in each metric. For every metric, Mech-case 4 has larger relative differences (as indicated by the larger color variation). The quantitative differences for displacement and stress between Mech-case 3 and 4 with this parameter set are also presented in Table 2.7. Because all of the Bio-cases show similar behavior, we only present a comparison for Bio-case 2.

2.6 Conclusion

2.6.1 Travelling waves

We have shown that the 1D glioma model permits travelling wave solutions with the linear, linear incompressible, or one-term Ogden models of elasticity. To our knowledge, this is the first time wave speed analysis has been applied to a glioma model comprised of a reaction-advection-diffusion equation coupled to a momentum balance equation to include mass effect. In cases where the diffusion coefficient varies in space and time, the wave speed $2\sqrt{D\rho}$ needs to be understood as an instantaneous wave speed, which the system tries to achieve and we see "attenuated travelling waves". We have also shown that allowing the elasticity parameters to vary does not affect the wave speed. This is due to low cell density at the leading edge of the wave causing insignificant deformation.

The wave speed does not change between the linear and one-term Ogden models of elasticity, nor does the addition of viscosity. Simulations do show differences in the wave profiles between the elasticity models, with a steeper wave profile in the case of the one-term Ogden model. This steeper profile is caused by the smaller magnitude of deformation in the one-term Ogden model. We also found that there is an order of magnitude difference in the displacement between the linear and Ogden models. This is a significant difference that results from the linear vs. exponential forms taken by the Cauchy stress functions of the linear and Ogden models (2.10) and (2.13), respectively.

We have considered only the propagation of one-dimensional invasion fronts of glioma. We are currently in the process of implementing two-dimensional version of these simulations [101]. A more complex three-dimensional model can eventually be implemented as well. If one were to assume isotropic diffusion tensor and isotropic uniform mechanical material, a reduced model of evolution, for example cylindrically or radially symmetric, can be considered as well. We did not consider such models here as we are interested in the glioma invasions along one dimension, as the first step in understanding the speed of invasion which can be computed (almost) analytically and studied thoroughly between different mechanical models presented.

2.6.2 Implications of mechanical comparisons on model choice

Our initial motivation to use the linear and one-term Ogden models of elasticity was based on the fact that previous work commonly used the linear model, and that the experimental results from Budday *et al.* suggested the Ogden model as a more realistic representation of healthy brain tissue [18]. We have previously noted that the $\alpha = -20$ case is likely a more realistic representation of the mode of elasticity present in a real brain with glioma as multiple loading forces would be experienced simultaneously. In fact, the above analysis can be used to further explore the validity of this assertion. By examining the differential effects of each elasticity model (linear, linear incompressible, Ogden with $\alpha = -20$, and Ogden with $\alpha = -7.3$) on our model of GBM spread and comparing to both experimental and clinical observations of GBM, we may be able to point to the most accurate model among these four options.

A newly developed method to measure tissue mechanics is magnetic resonance elastography (MRE) [53, 110, 113], where MRI imaging is combined with low-frequency vibrations. It has been shown to be useful to identify tissue stiffness differences as in fibrosis or tissue scarring [53, 110, 113]. Although we do not directly use parameters from any MRE studies, they do provide valuable information for general brain mechanics, as well as changes in mechanics that result from pathologies such as glioma.

2.6.3 Clinical relevance

Before discussing the application of this work to clinical disease, we would like to make it clear that we have not fit our models to clinical data. We have made our best efforts to produce realistic results by parameterizing with experimental data, but clinical data is not included. Keeping this in mind, we believe there are still meaningful conclusions be drawn from the distinctions between the mechanical models as shown here. One such consequence is the mechanical effect of a growing tumor on the brain tissue. Some symptoms of GBM can be directly related to mechanics, such as headaches that are induced by high intracranial pressure, and local destruction of brain tissue through tear

and shear [48]. Although headaches are a common symptom of brain tumors, headaches are not as commonly associated with GBM compared to other brain tumors [92]. As headaches are typically caused by increased intracranial pressure and deformation, our model may suggest that GBM causes comparatively lower levels of pressure and deformation compared to other types of brain tumors, which is consistent with the Ogden model. Secondly, GBM (a stage 4 cancer) is the most frequently diagnosed astrocytoma, accounting for more than 60% of brain tumors in adults [92], and more than 50% of GBM patients have a short history of symptoms (3-6 months) [48]. A possible explanation for the trend of few symptoms and a late stage of diagnosis in GBM is that the tumor grows and spreads slowly enough such that the surrounding brain tissue is able to adapt to the displacement caused by the tumor [109]. It appears that the tumor is able to develop without causing significant amounts of deformation and stress because of the mechanical properties of brain tissue. We note, however, that mechanical deformations is only one contribution to medical symptoms, as many other mechanisms are at play, such as edema formation, angiogenesis, fibrosis, inflammation, and other systemic reactions. None of these are included in our model.

Acknowledgements and declarations

Funding. M.R. acknowledges funding from the Cancer Research Institute of Northern Alberta (CRINA) and the Terry Fox Research Institute for their funding through the CRINA Marathon of Hope Graduate Studentship in Breast Cancer or Glioblastoma Research. M.R. acknowledges the Pacific Institute for the Mathematical Sciences (PIMS) MathBio Accelerator Award for partial support during this project. T.H. is grateful for support from the Natural Sciences and Engineering Research Council of Canada under the Discovery Grants Program RGPIN-2017-04158.

Conflicts of interest/Competing interests. The authors declare that they have no conflict of interest.

Availability of data and material. Not applicable.

Code availability. Code can be made available upon request.

Authors' contributions. M.R., T.H., and V.P. developed the model. M.R. carried out the calculations and analysis. M.R. implemented the model in the code and produced the figures. M.R., T.H., and V.P. wrote the manuscript. M.R., T.H., and V.P. read and approved the final manuscript.

2.7 Unit conversion

It is of note that the measurements for the elasticity parameters λ and μ are typically reported with units kPa, which in turn has units $kPa = \frac{kg}{m\ s^2}$. Similarly, the units for the viscosity coefficient, η, is usually reported with units $kPa \cdot s = \frac{kg}{m\ s^2} s = \frac{kg}{m\ s}$. As we are working in space and time units of cm and d, we must convert $kPa = \frac{kg}{m\ s^2}$ to $\frac{kg}{cm\ d^2}$ for λ and μ, as well as convert $kPa \cdot s = \frac{kg}{m\ s}$ to $\frac{kg}{cm\ d}$ for η. To do this, we multiply by conversion factors. For λ and μ, the factor is denoted by κ_1, while for η, the factor is denoted κ_2. The value of κ_1 is calculated by

$$1\ Pa = 1\frac{kg}{m\ s^2} = 1\frac{kg}{100\ cm\left(\frac{d}{24\cdot 60\cdot 60}\right)^2} = 74,649,600\frac{kg}{cm\ d^2} \tag{2.47}$$

$$\implies 1\ kPa = 74,649.6\frac{kg}{cm\ d^2} \implies \kappa_1 = 74,649.6\frac{kg}{cm\ d^2}\,. \tag{2.48}$$

Similarly, the value of κ_2 is calculated as

$$1\ kPa \cdot s = 74,649.6 \cdot \frac{1}{24 \cdot 60 \cdot 60}\frac{kg}{cm\ d} \tag{2.49}$$

$$\implies \kappa_2 = 74,649.6 \cdot \frac{1}{24 \cdot 60 \cdot 60}\frac{kg}{cm\ d}\,. \tag{2.50}$$

2.8 Alternative Ogden viscoelasticity

For the one-term Ogden viscoelasticity, we have developed an alternative viscosity form that is similar to that of Kelvin-Voigt, but instead of the time

derivative being applied only to u_x, we apply the time derivatives to the non-linear function of u_x that appears in the one-term Ogden model:

$$T_{\mathrm{OgdV2}}\left(u_x(x,t), u_{xt}(x,t)\right) = \frac{2\mu(x,t)}{\alpha}\left((1-u_x(x,t))^{-\alpha} - (1-u_x(x,t))^{\frac{1}{2}\alpha}\right) + \eta(x,t)\frac{\partial}{\partial t}\left(\frac{|\alpha|}{\alpha}\left((1-u_x(x,t))^{-\alpha} - (1-u_x(x,t))^{\frac{1}{2}\alpha}\right)\right). \tag{2.51}$$

Note that this viscoelastic Ogden model is chosen in such a way that the energy is always dissipated for both $\alpha > 0$ and $\alpha < 0$ as given by (2.57) below.

Equation (2.51) is a generalization of the classical Kelvin-Voigt model for hyperelastic materials. To show this relation we consider a material with the elastic part of the stress in the spatial representation given by T^{el}, and the viscoelastic part of the stress by T^{vi}, with the total stress being $T = T^{\mathrm{el}} + T^{\mathrm{vi}}$. In the absence of external heat energy sources, with external forces being $\mathbf{f}$, the equation of motion for spatial velocity $\mathbf{v}$ in three dimensions is given by the three dimensional generalization of (2.2)

$$\rho\left(\frac{\partial}{\partial t}\mathbf{v} + \mathbf{v}\cdot\nabla\mathbf{v}\right) = \mathrm{div}\left(T^{\mathrm{el}} + T^{\mathrm{vi}}\right) + \mathbf{f}\,, \tag{2.52}$$

see [76] for a more general formulation of balance laws of momenta and energy in various representations of material science, including the inertial terms.

It is assumed that T^{el} is derived from the stored energy function W in such a way that the total energy E is conserved in the absence of viscoelastic terms $T^{\mathrm{vi}} = 0$, with no external forces. We are only interested in one-dimensional motion, although the results below will also be valid for three dimensional motion with appropriate generalizations. Then, the dissipation of total mechanical energy in 1D, where $\mathbf{f} = (f, 0, 0)$, is given by the action of viscous term T^{vi} and the external force f

$$E = \int_\Omega \frac{1}{2}\rho|\mathbf{v}|^2 + W\mathrm{d}x \quad \Rightarrow \quad \frac{dE}{dt} = -\int_\Omega T^{\mathrm{vi}} v_x \mathrm{d}x + \int f v \mathrm{d}x \tag{2.53}$$

It is natural to put $v(x,t) = u_t(x,t)$ as we have indeed done in (2.3). We are only going to be interested in the first term of energy balance equation (2.53),

describing the energy dissipation due to the viscous terms.

Equation (2.51) can be viewed as a particular case of the viscoelastic part of the stress tensor to be

$$\begin{aligned} T^{\text{vi}} =& \eta \frac{\partial}{\partial t}\frac{\partial Q}{\partial u_x}, \quad \text{with} \\ Q :=& \frac{|\alpha|}{\alpha}\left(\frac{1}{1-\alpha}(1-u_x(x,t))^{1-\alpha} - \frac{1}{\alpha/2+1}(1-u_x(x,t))^{\frac{1}{2}\alpha+1}\right) \\ \frac{\partial Q}{\partial u_x} =& \frac{|\alpha|}{\alpha}\left((1-u_x(x,t))^{-\alpha} - (1-u_x(x,t))^{\frac{1}{2}\alpha}\right) \\ \frac{\partial^2 Q}{\partial u_x^2} =& |\alpha|\left((1-u_x(x,t))^{-\alpha-1} + \frac{1}{2}(1-u_x(x,t))^{\frac{1}{2}\alpha-1}\right) \geq 0\,, \end{aligned} \tag{2.54}$$

with the equation of motion still given by (2.52). In general, $Q(u_x)$ is a dimensionless "dissipative" function of the deformation gradient satisfying the convexity condition $\partial_{u_x}\partial_{u_x}Q \geq 0$. We have chosen Q in such a way that $\partial_{u_x}Q$ is proportional to the non-dimensionalized Ogden's stress (2.24), in order to have higher dissipation values at higher stresses, although other expressions for the function $Q(u_x)$ are possible as well. For an arbitrary $Q(u_x)$, the viscoelastic part of (2.54) can also be derived from the dissipation function [78] as follows. In one dimension, if the domain occupied by the material is Ω, the dissipation function is given by $\mathcal{R} = \int_\Omega \zeta \mathrm{d}x$, with the dissipative integrand $\zeta(\partial_x u, \partial_t u_x, t)$ given by

$$\zeta = \frac{\eta}{2}\frac{\partial^2 Q}{\partial u_x \partial u_x}u_{xt}^2\,. \tag{2.55}$$

Then, the viscoelastic part T^{vi} computed from the derivatives of dissipation function with respect to u_{xt}:

$$T^{\text{vi}} = \frac{\partial \zeta}{\partial u_{xt}} = \eta\frac{\partial^2 Q}{\partial u_x \partial u_x}u_{xt} = \eta\frac{\partial}{\partial t}\frac{\partial Q}{\partial u_x}\,. \tag{2.56}$$

A multi-dimensional generalization of that dissipative function can also be readily derived, with additional requirements on the symmetry of the dependence of Q on its components (frame indifference) as described by [78]. With

this dissipation function, the total energy evolves according to

$$\frac{dE}{dt} = -\int_\Omega \eta \frac{\partial^2 Q}{\partial u_x \partial u_x} u_{xt}^2 \mathrm{d}x = -2\int_\Omega \zeta \mathrm{d}x \tag{2.57}$$

The standard extension of the Kelvin-Voigt theory is a particular case of (2.54) with $Q = \frac{1}{2}u_x^2$:

$$T^{\mathrm{vi}} = \eta \partial_t u_x \tag{2.58}$$

giving the energy dissipation

$$\frac{dE}{dt} = -\int_\Omega \eta u_{xt}^2 \mathrm{d}x\,, \quad \zeta = \frac{\eta}{2} u_{xt}^2\,. \tag{2.59}$$

As shown in Figure 2.23, for the application of slowly evolving brain mechanics we are interested in here, there is no discernible difference between the results of the augmented viscoelastic problem (2.51) and the classical choice $Q = \frac{1}{2}u_x^2$. We also found no significant differences in the wave speed between the two versions of viscoelastic Ogden models (see Table 2.6).

2.9 Numerical methods

The model system is simulated in MATLAB R2020b. The spatial and temporal domains are discretized homogeneously with space and time steps Δx and Δt, respectively. For spatial derivatives, finite difference schemes are employed. The time derivatives are estimated using backward time differences.

The system is simulated by sequentially solving the equations over all spatial points for each time step. A broad outline is as follows:

1. Initialize simulation parameters

    - Set simulation parameters (domain size, step sizes, simulation time, etc.)
    - Set function parameters ρ, p_1, p_2, s
    - Specify initial conditions c_0, $\mathbf{m}_0$, u_0

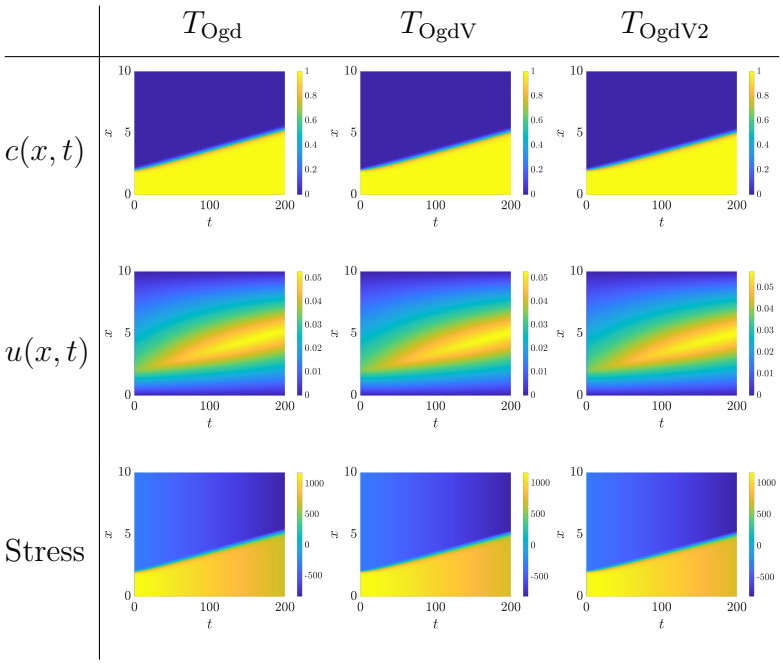

Figure 2.23: Comparison of cell density and displacement for the Mech-case 3 and Mech-case 3 viscoelastic models, T_{OgdV} and T_{OgdV2}, ($\alpha = -20$) for Bio-case 1 where $\rho = 0.15$, $\mathbf{m}_{\mathrm{Ogd}} = (D, \mu) = (0.0005, \bar{\mu}_{\mathrm{Ogd}})$, and $\eta = \bar{\eta}$.

2. Sequentially solve the system equations over all spatial points in a time loop

   - Material advection (equation (2.4))
     - Apply advection operator to $D(:,t)$, $\lambda(:,t)$, $\mu(:,t)$, $\eta(:,t)$ (*upwind*) to get $D(:,t+\Delta t)$, $\lambda(:,t+\Delta t)$, $\mu(:,t+\Delta t)$, $\eta(:,t+\Delta t)$
   - Advection-diffusion-reaction of tumor cell density (equation (2.1)). Note that operator splitting is used to apply each process (diffusion, advection, proliferation) in the equation.
     - Apply diffusion operator (*conservative centered difference*) to get c^*
     - Apply advection operator (*conservative upwind*) to get c^{**}
     - Apply reaction operator (*forward difference*) to get $c(:,t+\Delta t)$
   - Elasticity/viscoelasticity equation for displacement (equation (2.2)).
     - For linear elasticity/viscoelasticity and linear incompressible elasticity: For linear and linear incompressible elasticity, use implicit solver (*mldivide*, *centered difference*) to get $u(:,t+\Delta t)$. For linear viscoelasticity, the same method is used, but a finite difference is used to incorporate the necessary time derivatives.
     - For one-term Ogden elasticity: In order to solve for the deformation with Ogden elasticity, a nested pair of root solvers (*fzero*) is used. The outer root finder solves for $T(0,t)$ with the objective function involving a second instance of *fzero* which solves for $u(x,t)$ with $T(0,t)$ as parameter.
       First, the momentum balance equation is integrated with respect to x, giving

$$\begin{aligned} T_{\mathrm{Ogd}}(u_x(x,t)) =& \frac{2\mu(x,t)}{\alpha}((1-u_x(x,t))^{-\alpha} - (1-u_x(x,t))^{\alpha/2}) \\ =& \int_0^x b(c(x,t))\, dx + T(0,t)\,. \end{aligned} \tag{2.60}$$

       where $T(0,t)$ is unknown. In order to solve for u_x, a substitution is made where $z(x,t) := (1-u_x(x,t))^{-\alpha}$, resulting in the

equation

$$T_{\mathrm{Ogd}}(z(x,t)) = \frac{2\mu(x,t)}{\alpha}(z(x,t) - z(x,t)^{-1/2}) = \int_0^x b(c(x,t))\, dx + T(0,t)\,, \qquad (2.61)$$

This equation is then solved for $z(x,t)$ (using *fzero*) while leaving $T(0,t)$ as an unknown parameter. The resulting value of $u(x,t)$ is then determined from $z(x,t)$ via numerical integration (*trapz*) with respect to x. The final step is to determine the appropriate value of $T(0,t)$. This is achieved in the outer loop of *fzero* with $T(0,t)$ as the variable. For Ogden viscoelasticity, the same method is used, but a finite difference is used to incorporate the necessary time derivatives.

- Update velocity (equation (2.3))
  - Use $u(:, t + \Delta t)$ to get $v(:, t + 1)$ (*backward difference*)

3. Go back to step 2 for the next time step until final time is reached.

The numerical wave speeds were computed by taking backward differences from the midpoint of the wave profiles at regular time intervals (every time step) and then averaging over these differences. As the discretization would not permit a true midpoint in most cases, the wave profiles were smoothed using interpolation (via the *interp1* function in MATLAB) before taking the backward differences. The starting point for these differences was taken as $t = 175$ to allow for the establishment of the wave front.

2.9.1 Numerics equations

For the function arguments (x,t), x represents the space step and t the time step.

- Centered difference, first derivatives with respect to time and space,

respectively.

$$u_t(x,t) = \frac{u(x,t+\Delta t) - u(x,t-\Delta t)}{2\Delta t} \tag{2.62}$$

$$u_x(x,t) = \frac{u(x+\Delta x,t) - u(x-\Delta x,t)}{2\Delta x} \tag{2.63}$$

- Centered difference, second derivative with respect to time and space, respectively.

$$u_{tt}(x,t) = \frac{u(x,t+\Delta t) - 2u(x,t) + u(x,t-\Delta t)}{\Delta t^2} \tag{2.64}$$

$$u_{xx}(x,t) = \frac{u(x+\Delta x,t) - 2u(x,t) + u(x-\Delta x,t)}{\Delta x^2} \tag{2.65}$$

- Forward difference, first derivative with respect to time

$$u_t(x,t) = \frac{u(x,t+\Delta t) - u(x,t)}{\Delta t} \tag{2.66}$$

2.9.2 Elasticity solver check

The elasticity equation is given by

$$((\lambda + 2\mu)u_x)_x = b\,.$$

This is a non-homogeneous Sturm-Liouville problem with the associated eigenvalue problem

$$((\lambda + 2\mu)u_x)_x + \lambda u = b\,.$$

Taking $(\lambda + 2\mu) = (1 - x^2)$, this is the Legendre equation which has the form

$$((1 - x^2)u_x)_x + n(n+1)u = b\,.$$

We use this relation between the elasticity equation and Legendre equation to confirm the elasticity solver by setting $\lambda + 2\mu = (1 - x^2)$ and comparing the simulated results to the analytic solution obtained using Legendre polynomial expansions. Both the homogeneous ($b = 0$) and nonhomogeneous ($b \neq 0$) Leg-

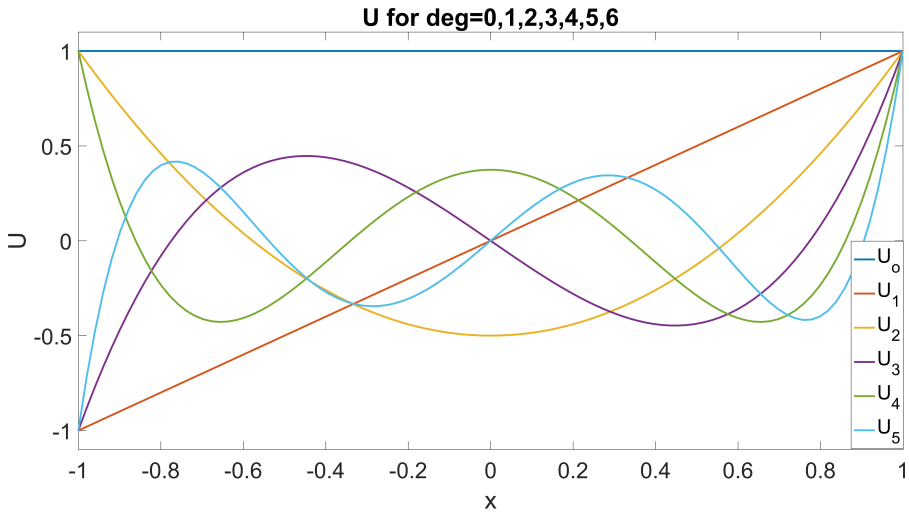

Figure 2.24: Homogenous Legendre Equation Solutions

endre equations are considered. The simulated solutions for the homogeneous case (of degrees $n = 0...6$) are shown in figure 2.24, successfully reproducing the classical Legendre polynomials.

For the nonhomogeneous case, we set the left hand side to be $\sin(\pi x)$ and consider the third order expansion solutions. As the n^{th} order term of the Legendre expansion solution goes to 0, we take $n = 4$ in the Legendre equation, giving a third order approximation on the left hand side. We then set the right hand side to be the third order Legendre polynomial expansion of $\sin(\pi x)$. That is, we take the left hand side to be

$$b = \sin(\pi x) \approx \left(\frac{3}{\pi} - 3\left(\frac{7(\pi^2 - 15)}{2\pi^3}\right)\right) x + 5\left(\frac{7(\pi^2 - 15)}{2\pi^3}\right) x^3 .$$

Figure 2.25 shows both the analytic and numerical solutions of the nonhomogenous Legendre equation, with good agreement between them. This supports the accuracy of the numerical elasticity solver.

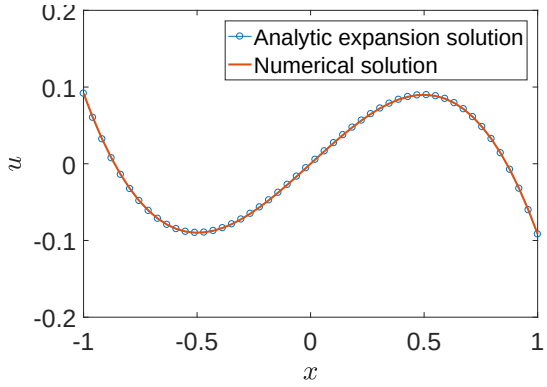

Figure 2.25: Nonhomogeneous Legendre Equation Solution Comparison

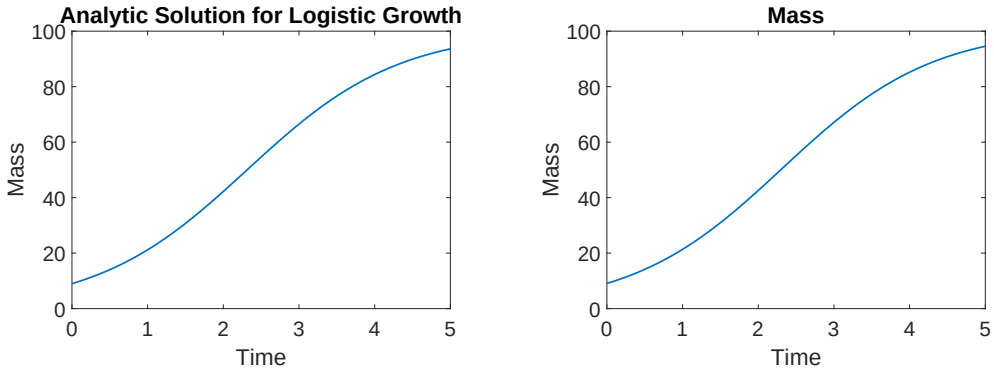

Figure 2.26: Reaction Equation Solution Comparison

2.9.3 Reaction solver check

The reaction function uses a simple backwards time difference to approximate the solution to logistic equation

$$c_t = \rho c(1 - c)\,.$$

Figure 2.26 shows that the solver agrees with the analytic solution to the logistic growth equation.

2.10 Generalization of wave speed analysis

With the results from Sections 2.3 and 2.4 that travelling waves exist with the same minimal wave speed for both the linear and one-term Ogden elasticity models, we considered whether the wave speed results could be generalized. As well as the elasticity model, we also investigate if the wave speed results hold for the conservative advection of material parameters as mentioned in Section 1.5. In this section, we present results exploring these extensions to the analysis in Section 2.3.

2.10.1 Wave speed analysis of the glioma model with generalized elasticity

With the wave speed analysis result of Lemma 1 holding for both the linear elasticity and one-term Ogden elasticity models, we considered whether this result holds for a larger class of elasticity models. Here, we define a more "generalized elasticity" model which follows some assumptions and show that Lemma 1 still hold for this larger class of elasticity models.

First, we define a "generalized elasticity" model.

Definition 1. *Definition of generalized elasticity model. Consider the momentum balance equation of the form* $T_x = (P(x,t)E(u_x))x = f(c)c_x$*, where* $P(x,t)$ *includes the elasticity parameters and* $E(u_x)$ *defines the type of elasticity. We define* $T_x = (P(x,t)E(u_x))x = f(c)c_x$ *as a generalized elasticity model under the assumptions*

- *there is no force in the absence of tumor cells, that is* $f(0) = 0$*,*
- *the stress tensor* T *must explicitly include* u_x*, i.e.* $\frac{\partial}{\partial u_x}E \neq 0$*,*
- *the stress tensor* T *must explicitly include* λ *or* μ*, i.e.* $P(x,t) \neq 0$ *.*

We carried out the wave speed analysis the 1D glioma model with non-conservative advection of the material properties, as well as the 1D glioma model with conservative advection of the diffusion and non-conservative advection of the elasticity parameters. The case where both the diffusion and elasticity parameters advect conservatively was not included as it was intractable

and because, as argued in Section 1.5, this case is likely not physically realistic. We present the results for the 1D glioma model with non-conservative advection of the material properties as the other calculations follow similarly.

With the generalized elasticity model, the 1D glioma model becomes

$$\begin{aligned} c_t =& (Dc)_{xx} - (cv)_x + \rho c(1-c) && (2.67)\\ T_x =& (P(x,t)E(u_x))x = f(c)c_x && (2.68)\\ v =& u_t && (2.69)\\ \mathbf{m}_t + v\mathbf{m}_x =& \mathbf{0} && (2.70) \end{aligned}$$

We can compare this form to linear and Ogden elasticity to see the components clearly.

- For linear elasticity, the stress tensor is

$$T = (\lambda + 2\mu)u_x\,, \tag{2.71}$$

  corresponding to $P = \lambda + 2\mu$ and $E = u_x$.

- For Ogden elasticity, the stress tensor is

$$T = \frac{2\mu}{\alpha}\left((1-u_x)^{-\alpha} - (1-u_x)^{\alpha/2}\right)\,, \tag{2.72}$$

  corresponding to $P = \frac{2\mu}{\alpha}$ and $E = (1-u_x)^{-\alpha} - (1-u_x)^{\alpha/2}$.

Then the momentum balance equation $T_x = b = f(c)c_x$ with a general elastic model is

$$\begin{aligned} T_x =& \frac{\partial}{\partial x}(P(x,t))E(u_x) + P(x,t)\frac{d}{dx}(E(u_x)) && (2.73)\\ =& \frac{\partial}{\partial x}(P(x,t))E(u_x) + P(x,t)\frac{\partial}{\partial u_x}(E(u_x))u_{xx} && (2.74)\\ \implies f(c)c_x =& \frac{\partial}{\partial x}P(x,t)E(u_x) + P(x,t)\frac{\partial}{\partial u_x}(E(u_x))u_{xx}\,. && (2.75) \end{aligned}$$

Solving this for u_{xx}, we have

$$u_{xx} = \frac{f(c)c_x - \frac{\partial}{\partial x}(P(x,t))E(u_x)}{P\frac{\partial}{\partial u_x}(E(u_x))}\,. \tag{2.76}$$

We can do a sanity check with the elasticity models used earlier.

Example 1 – Linear elasticity. With the linear elasticity stress tensor (2.71) giving that $P = \lambda + 2\mu \implies \frac{\partial}{\partial x}P = \lambda_x + 2\mu_x$ and $E = u_x \implies \frac{\partial}{\partial u_x}(E(u_x)) = 1$.
So we expect to get

$$u_{xx} = \frac{f(c)c_x - (\lambda_x + 2\mu_x)u_x}{\lambda + 2\mu}\,. \tag{2.77}$$

With the linear stress tensor, we calculate the momentum balance equation as

$$\begin{aligned} T_x =& (\lambda + 2\mu)_x u_x + (\lambda + 2\mu)(u_x)_x && (2.78)\\ =& (\lambda_x + 2\mu_x)u_x + (\lambda + 2\mu)(u_{xx}) && (2.79)\\ =& f(c)c_x && (2.80)\\ \implies u_{xx} =& \frac{f(c)c_x - (\lambda_x + 2\mu_x)u_x}{\lambda + 2\mu} && (2.81) \end{aligned}$$

exactly as expected.

Example 2 – Ogden elasticity. With the one-term Ogden stress tensor (2.72) giving that $P = \frac{2\mu}{\alpha} \implies \frac{\partial}{\partial x}P = \frac{2\mu_x}{\alpha}$ and $E = (1-u_x)^{-\alpha} - (1-u_x)^{\alpha/2}$ $\implies \frac{\partial}{\partial u_x}(E(u_x)) = \alpha\left((1-u_x)^{-\alpha-1} + \frac{1}{2}(1-u_x)^{\alpha/2-1}\right)$.
So we expect to get

$$u_{xx} = \frac{f(c)c_x - \frac{2\mu_x}{\alpha}\left((1-u_x)^{-\alpha} - (1-u_x)^{\alpha/2}\right)}{\frac{2\mu}{\alpha}\alpha\left((1-u_x)^{-\alpha-1} + \frac{1}{2}(1-u_x)^{\alpha/2-1}\right)}\,. \tag{2.82}$$

With the Ogden stress tensor, we calculate the momentum balance equation as

$$\begin{aligned} T_x =& \left(\frac{2\mu}{\alpha}\left((1-u_x)^{-\alpha}-(1-u_x)^{\alpha/2}\right)\right)_x && (2.83)\\ =& \left(\frac{2\mu_x}{\alpha}\right)\left((1-u_x)^{-\alpha}-(1-u_x)^{\alpha/2}\right) \\ &+\left(\frac{2\mu}{\alpha}\right)(\alpha u_{xx})\left((1-u_x)^{-\alpha-1}+\frac{1}{2}(1-u_x)^{\alpha/2-1}\right) && (2.84)\\ =& f(c)c_x && (2.85)\\ \implies u_{xx} =& \frac{f(c)c_x-\left(\frac{2\mu_x}{\alpha}\right)\left((1-u_x)^{-\alpha}-(1-u_x)^{\alpha/2}\right)}{\frac{2\mu}{\alpha}\alpha\left((1-u_x)^{-\alpha-1}+\frac{1}{2}(1-u_x)^{\alpha/2-1}\right)} && (2.86)\end{aligned}$$

exactly as expected.

Equilibria and stability. The full system in travelling wave coordinates is then

$$\begin{aligned} c_0' =& c_1 && (2.87)\\ c_1' =& \frac{-1}{D_0}(-\sigma c_1-\sigma c_0 u_1'-\sigma c_1 u_1-2D_1c_1-D_1'c_0-\rho c_0(1-c_0)) && (2.88)\\ u_0' =& u_1 && (2.89)\\ u_1' =& \frac{f(c_0)c_1-\frac{\partial}{\partial x}(P)E(u_1)}{P\frac{\partial}{\partial u_1}(E(u_1))}\,. && (2.90)\end{aligned}$$

From (2.70), we get that

$$\begin{aligned} \mathbf{m}_t+v\mathbf{m}_x =& \mathbf{0} && (2.91)\\ \implies -\sigma\mathbf{m}'-\sigma u'\mathbf{m}' =& \mathbf{0} && (2.92)\\ \implies -\sigma\mathbf{m}'(1+u') =& \mathbf{0} && (2.93)\\ \implies \mathbf{m}'=(D_1,\lambda_1,\mu_1) =& \mathbf{0} && (2.94)\\ \implies \mathbf{m}=(D_0,\lambda_0,\mu_0) =& \text{ cnst} && (2.95)\\ \implies \frac{\partial}{\partial x}P=0 \text{ and } P =& \text{ cnst} && (2.96)\end{aligned}$$

As this condition does not depend on any of the other variables, we can assume this in the glioma model which then simplifies to

$$\begin{aligned} c_0' =& c_1 && (2.97)\\ c_1' =& \frac{1}{D_0}(-\sigma c_1 - \sigma c_0 u_1' - \sigma c_1 u_1 - \rho c_0(1-c_0)) && (2.98)\\ u_0' =& u_1 && (2.99)\\ u_1' =& \frac{f(c_0)c_1}{PE_{u_1}}\,. && (2.100) \end{aligned}$$

where $E_{u_1} := \frac{\partial}{\partial u_1}(E(u_1))$.

At equilibrium, we get that $c_1 = 0$ and $u_1 = 0$. With $c_1 = 0$ the u_1' equation is automatically zero. Finally, with these equilibrium values, from the c_1' equation we get that $c^{*0} = 0$ or $c^{*1} = 1$. Thus, we have the equilibria $X_0 = (0, 0, u^{*0}, 0)$ and $X_1 = (1, 0, u^{*1}, 0)$, where u^{*0}, u^{*1} can be any positive finite values.

The Jacobians are given by

$$J(X_0) = \begin{bmatrix} 0 & 1 & 0 & 0 \\ \frac{-\rho}{D} & \frac{-\sigma}{D} & 0 & 0 \\ 0 & 0 & 0 & 1 \\ 0 & 0 & 0 & 0 \end{bmatrix} \quad \text{and} \quad J(X_1) = \begin{bmatrix} 0 & 1 & 0 & 0 \\ \frac{-\rho}{D} & \frac{-\sigma}{D}\left(1 + \frac{f(1)}{PE_{u_1}(0)}\right) & 0 & 0 \\ 0 & 0 & 0 & 1 \\ 0 & \frac{f(1)}{PE_{u_1}(0)} & 0 & 0 \end{bmatrix}. \tag{2.101}$$

For $J(X_0)$, we get the same conditions for a stable node as usual, ie. $\sigma > 2\sqrt{D\rho}$

with Eigenvalues $\Lambda = (-, -, 0, 0)$. For $J(X_1)$, we need to get the Eigenvalues.

$$\det(J(X_1) - \Lambda I) = \det \begin{bmatrix} -\Lambda & 1 & 0 & 0 \\ \frac{-\rho}{D} & \frac{-\sigma}{D}\left(1 + \frac{f(1)}{PE_{u_1}(0)}\right) - \Lambda & 0 & 0 \\ 0 & 0 & -\Lambda & 1 \\ 0 & \frac{f(1)}{PE_{u_1}(0)} & 0 & -\Lambda \end{bmatrix} \tag{2.102}$$

$$= -\Lambda \det \begin{bmatrix} \frac{-\sigma}{D}\left(1 + \frac{f(1)}{PE_{u_1}(0)}\right) - \Lambda & 0 & 0 \\ 0 & -\Lambda & 1 \\ \frac{f(1)}{PE_{u_1}(0)} & 0 & -\Lambda \end{bmatrix} \tag{2.103}$$

$$- \det \begin{bmatrix} \frac{-\rho}{D} & 0 & 0 \\ 0 & -\Lambda & 1 \\ 0 & 0 & -\Lambda \end{bmatrix} \tag{2.104}$$

$$= -\Lambda \left[\Lambda^2 \left(\frac{-\sigma}{D}\left(1 + \frac{f(1)}{PE_{u_1}(0)}\right) - \Lambda\right)\right] - \Lambda^2 \frac{\rho}{D} \tag{2.105}$$

$$= \Lambda^2 \left[-\Lambda \left(\frac{-\sigma}{D}\left(1 + \frac{f(1)}{PE_{u_1}(0)}\right) - \Lambda\right) - \frac{\rho}{D}\right] \tag{2.106}$$

$$= 0 \tag{2.107}$$

which gives $\Lambda_1, \Lambda_2 = 0$. For $\Lambda_{3,4}$, we solve

$$-\Lambda \left(\frac{-\sigma}{D}\left(1 + \frac{f(1)}{PE_{u_1}(0)}\right) - \Lambda\right) - \frac{\rho}{D} = 0 \tag{2.108}$$

$$\implies \Lambda^2 + \Lambda \left(\frac{\sigma}{D}\right)\left(1 + \frac{f(1)}{PE_{u_1}(0)}\right) - \frac{\rho}{D} = 0 \tag{2.109}$$

$$\implies \Lambda_{3,4} = \left[-\left(\frac{\sigma}{D}\right)\left(1 + \frac{f(1)}{PE_{u_1}(0)}\right) \pm \sqrt{\left(\frac{\sigma}{D}\right)^2 \left(1 + \frac{f(1)}{PE_{u_1}(0)}\right)^2 + 4\frac{\rho}{D}}\right] /2 \tag{2.110}$$

For X_1 to be a saddle, we need the expression under the root to be positive. This is guaranteed as both ρ and D are positive.

Thus, for $\sigma \geq \sigma^* = 2\sqrt{D^{*0}\rho}$, we get that X_0 is a stable node and X_1 is a saddle, allowing for the existence of travelling waves. This is the same result as in Lemma 1.

2.10.2 Wave speed analysis with conservative material property advection

As discussed in Section 1.5, the form of the advection operator for the material property advection has been modeled as both conservative and non-conservative. With this in mind, we carried out the same wave speed analysis for the 1D model as in Section 2.3.1 (with both linear elasticity and one-term Ogden model) with conservative advection for

- diffusion only
- both diffusion and material properties, λ and/or μ.

In all cases, we came to the same conclusion as Lemma 1. Numerical simulations were carried out for these cases (not shown), confirming the results.

Chapter 3

Glioma spread model in 2D

3.1 Introduction

In this chapter, we turn to simulating and examining our mechanical model of glioma spread in higher spatial dimensions. Although there may be some insight to be gained using the tractability and analysis of a glioma spread model in one spatial dimension, real brain tumors are obviously three dimensional. As a step closer to modelling the 3D spread of glioma, we next consider a model with two spatial dimensions. Unlike the previous chapter, we only consider the linear elasticity model in this chapter. This is a limitation imposed by the numerics, which we discuss in Section 3.5.

We begin the chapter by presenting the full 2D model. Next, we discuss the numerical software used to simulate the model, including a brief overview of the software structure and description of the simulation work flow. Furthermore, we describe in detail the methods for acquiring, translating, and incorporating data for the simulation domain and initial condition for diffusion tensors. With the simulation preliminaries in hand, we present and compare simulations of the 2D model for a range of parameters.

3.2 The 2D model

Let the spatial domain be $\Omega \subset \mathbf{R}^2$, and take time to be $t \in [0, \infty)$. Then the domain is $\mathcal{U} = \Omega \times [0, \infty)$. The spatial domain is determined by MRI data which is then translated into a single domain representing the brain tissue. The total boundary of the domain, denoted $\partial\Omega$, is composed of three distinct boundaries: the left and right ventricles, denoted $\partial\Omega_{\text{vent}}$, and the outer brain tissue boundary, denoted $\partial\Omega_{\text{out}}$. The ventricle boundaries are taken to be deformable, while the outer brain tissue boundary is assumed to be static. The tumor cell density (normalized) is denoted by c. The vector $\mathbf{m}$ denotes parameters associated with material properties of the tumor and healthy brain tissue, including diffusion $\mathbf{D}(\mathbf{x}, t)$, shear modulus $\mu(\mathbf{x}, t)$, and bulk modulus $\lambda(\mathbf{x}, t)$. The displacement and the velocity resulting from this displacement, are denoted by $\mathbf{u}(\mathbf{x}, t)$ and $\mathbf{v}(\mathbf{x}, t)$, respectively. The system on $\mathcal{U}$ is then

$$c_t(\mathbf{x}, t) = \nabla\nabla : (\mathbf{D}(\mathbf{x}, \mathbf{t})c(\mathbf{x}, t)) - \nabla \cdot (c(\mathbf{x}, t)\mathbf{v}(\mathbf{x}, t)) + \rho c(\mathbf{x}, t)(1 - c(\mathbf{x}, t)) \tag{3.1}$$

$$\nabla \cdot \mathbf{T}\,(\mathbf{x}, t, \nabla\mathbf{u}) = \mathbf{b}(c(\mathbf{x}, t)) \tag{3.2}$$

$$\mathbf{v}(\mathbf{x}, t) = \mathbf{u}_t(\mathbf{x}, t) \tag{3.3}$$

$$\mathbf{m}_t(\mathbf{x}, t) + \mathbf{v}(\mathbf{x}, t)\nabla\mathbf{m}(\mathbf{x}, t) = 0\,, \tag{3.4}$$

with initial conditions for $\mathbf{x} \in \Omega$

$$c(\mathbf{x}, 0) = c_0(\mathbf{x}), \qquad \mathbf{m}(\mathbf{x}, 0) = \mathbf{m}_0(\mathbf{x}), \qquad \mathbf{u}(\mathbf{x}, 0) = \mathbf{u}_0(\mathbf{x})\,. \tag{3.5}$$

The cell density has no-flux boundary conditions for $t \in [0, \infty)$ given by

$$\nabla \cdot (\mathbf{D}(\mathbf{x}, t)c(\mathbf{x}, t)) - c(\mathbf{x}, t)\mathbf{v}(\mathbf{x}, t)|_{\partial\Omega} = 0\,. \tag{3.6}$$

For static boundaries of the spatial domain, $\partial\Omega_{\text{out}}$, we have the boundary condition

$$\mathbf{u}(\mathbf{x}, t)|_{\partial\Omega_{\text{out}}} = 0\,. \tag{3.7}$$

On $\partial\Omega_{\text{out}}$, it follows from equation (3.7) that

$$\mathbf{v}(\mathbf{x},t)|_{\partial\Omega_{\text{out}}} = 0\,. \tag{3.8}$$

On the deformable boundaries, $\partial\Omega_{\text{vent}}$, we allow $\mathbf{u}(\mathbf{x},t)$ to be nonzero. Hence, $\mathbf{v}(\mathbf{x},t)$ can also be nonzero on such boundaries. The key to closing the system is the expression of the stress tensor $\mathbf{T}$ as a function of the deformation gradient, $\nabla\mathbf{u}$, in (3.2). The linear stress tensor is given by

$$\mathbf{T}_{\text{Lin2D}}(\mathbf{x},t,\nabla\mathbf{u}) = \lambda(\mathbf{x},t)\nabla\cdot\mathbf{u}(\mathbf{x},t) + \mu(\mathbf{x},t)(\nabla\mathbf{u}(\mathbf{x},t) + \nabla\mathbf{u}(\mathbf{x},t)^T)\,. \tag{3.9}$$

The associated (general plane) von Mises stress is then

$$T_{\text{vm}} = \sqrt{T_{11}^2 - T_{11}T_{22} + T_{22}^2 + 3T_{12}^2}\,. \tag{3.10}$$

The body forces produced by the growing tumor are denoted by $\mathbf{b}$. The form of $\mathbf{b}$ is taken from [114] as

$$\mathbf{b}\,(c,p,\nabla c) = p\tanh(c)\nabla c\,. \tag{3.11}$$

As described in Section 1.4, this is a phenomenological model for the forces created by a growing tumor borrowed from [114]. There are key characteristics of this model that capture the likely reality of a growing tumor. First, in the absence of tumor cells, there is no force. Secondly, the force is maximized at the carrying capacity of the tumor (i.e., when $c(\mathbf{x},t) = 1$). Lastly, the dependence on the gradient means that a larger force is generated in the presence of large differences in cancer density. Notably, the parameter p is unknown. As discussed later, it may be possible to fit p to patient data. For this work, we use a range of p values to explore how p affects the dynamics of glioma spread.

The choices of diffusion and reaction terms are the same as discussed in Section 2.2.

3.3 Methods for simulating glioma in 2D

From obtaining the simulation domain to producing figures, there are many steps required to simulate the 2D glioma model. The main steps are

- Domain definition from MRI/DTI;
- Initialization of variables and parameters, including initialization of the diffusion tensor from DTI data;
- Running the model simulation;
- Saving and visualizing the data .

These main points include many steps which are discussed in the following sections.

3.3.1 Numerical software and problem formulation

To simulate the 2D model, we turn to the finite element software FreeFEM [51]. FreeFEM automatically generates finite elements for a prescribed geometry, making it very user-friendly. The automatic generation, and adaptation, of the finite element mesh is a powerful tool that allows the implementation of complex physics models without the need of using cumbersome manual mesh generation. Within a given finite element space, you can then define finite element functions which are automatically interpolated across the mesh. Each operator or equation is defined as a "Problem" in FreeFEM, with the simulation occurring when the problem is called.

The PDE "Problems" in FreeFEM must be defined using the *weak form* of the PDE. To derive the weak form of the PDEs involved, for each equation, we multiply the equation by a test function, $\mathbf{q}$, and integrate over space. Finally, we apply the Divergence Theorem to arrive at the weak form equations. We will show the derivation of the weak forms for the glioma spread model given by (3.1)-(3.8).

Weak formulation of FAAD. The FAAD equation which models the tumor cell evolution is given by (3.1). For the weak formulation of FAAD, we leave out the reaction term, applying that after solving the rest of the equation. This leaves us with the modified FAAD equation:

$$c_t(x,t) = \nabla\nabla : (\mathbf{D}(x,t)c(x,t)) - \nabla \cdot (c(x,t)\mathbf{v}(x,t))\,. \tag{3.12}$$

For the time derivative, we use a simple finite difference approximation:

$$c_t(x,t) = \frac{c(x,t) - c(x,t-\Delta t)}{\Delta t}\,, \tag{3.13}$$

where t denotes the current time step. With this approximation, the modified FAAD equation becomes

$$\frac{c(x,t) - c(x,t-\Delta t)}{\Delta t} = \nabla\nabla : (\mathbf{D}(x,t)c(x,t)) - \nabla \cdot (c(x,t)\mathbf{v}(x,t)) \tag{3.14}$$

$$\implies \frac{c(x,t) - c(x,t-\Delta t)}{\Delta t} - \nabla\nabla : (\mathbf{D}(x,t)c(x,t)) + \nabla \cdot (c(x,t)\mathbf{v}(x,t)) = 0\,. \tag{3.15}$$

Multiplying by a test function, $q(x,t)$, and integrating over space, we have

$$\int_\Omega \left(\frac{c(x,t) - c(x,t-\Delta t)}{\Delta t}\right) q(x,t)\; d\Omega - \int_\Omega \left(\nabla\nabla : (\mathbf{D}(x,t)c(x,t))\right)\; q(x,t)\; d\Omega + \int_\Omega \left(\nabla \cdot (c(x,t)\mathbf{v}(x,t))\right)\; q(x,t)\; d\Omega = 0\,. \tag{3.16}$$

Applying the Divergence Theorem, we have

$$\begin{aligned}
&\int_\Omega \left(\frac{c(x,t)-c(x,t-\Delta t)}{\Delta t}\right) q(x,t)\ d\Omega \\
&\quad + \int_\Omega (\nabla\cdot(\mathbf{D}(x,t)c(x,t)))\cdot\nabla q(x,t)\ d\Omega \\
&\quad - \int_{\partial\Omega} \mathbf{n}\cdot(\nabla\cdot(\mathbf{D}(x,t)c(x,t)))q(x,t)\ d\partial\Omega \\
&\quad - \int_\Omega (c(x,t)\mathbf{v}(x,t))\cdot\nabla q(x,t)\ d\Omega \\
&\quad + \int_{\partial\Omega} \mathbf{n}\cdot(c(x,t)\mathbf{v}(x,t))q(x,t)\ d\partial\Omega = 0 \qquad (3.17)\\
\Longrightarrow &\int_\Omega \left(\frac{c(x,t)-c(x,t-\Delta t)}{\Delta t}\right) q(x,t)\ d\Omega \\
&\quad + \int_\Omega (\nabla\cdot(\mathbf{D}(x,t)c(x,t)))\cdot\nabla q(x,t) - (c(x,t)\mathbf{v}(x,t))\cdot\nabla q(x,t)\ d\Omega \\
&\quad - \int_{\partial\Omega} \mathbf{n}\cdot\big((\nabla\cdot(\mathbf{D}(x,t)c(x,t))) - (c(x,t)\mathbf{v}(x,t))\big)q(x,t)\ d\partial\Omega = 0\,. \qquad (3.18)
\end{aligned}$$

With no flux boundary conditions, we have

$$\mathbf{n}\cdot\big((\nabla\cdot(\mathbf{D}(x,t)c(x,t))) - (c(x,t)\mathbf{v}(x,t))\big) = 0$$

on $\partial\Omega$. Thus, the above simplifies to

$$\begin{aligned}
&\int_\Omega \left(\frac{c(x,t)-c(x,t-\Delta t)}{\Delta t}\right) q(x,t)\ d\Omega \\
&\quad + \int_\Omega (\nabla\cdot(\mathbf{D}(x,t)c(x,t)))\cdot\nabla q(x,t)\ d\Omega \\
&\quad - \int_\Omega (c(x,t)\mathbf{v}(x,t))\cdot\nabla q(x,t)\ d\Omega = 0 \qquad (3.19)\\
\Longrightarrow &\int_\Omega (c(x,t)-c(x,t-\Delta t))\, q(x,t)\ d\Omega \\
&\quad + \Delta t \int_\Omega (\nabla\cdot(\mathbf{D}(x,t)c(x,t)))\cdot\nabla q(x,t)\ d\Omega \\
&\quad - \Delta t \int_\Omega (c(x,t)\mathbf{v}(x,t))\cdot\nabla q(x,t)\ d\Omega = 0\,. \qquad (3.20)
\end{aligned}$$

This is the final form of the weak formulation that is then translated into the FreeFEM code with the reaction term added as well. The boundary conditions are also applied by including "`+on(G0, c=0), +on(G1, c=0), +on(G2, c=0),`" inside the FAAD problem.

Weak formulation of momentum balance equation. The momentum balance equation is given by (3.2).

$$\nabla \cdot \mathbf{T}(\mathbf{u}) = \mathbf{b}\,, \tag{3.21}$$

where $\mathbf{T}(\mathbf{u}) = 2\mu\epsilon(\mathbf{u}) + \lambda\ tr(\epsilon(\mathbf{u}))\mathbf{I}$ and $\epsilon(\mathbf{u}) = \frac{1}{2}(\nabla\mathbf{u} + \nabla\mathbf{u}^T)$. Multiplying by a test function, $\mathbf{q}$, and integrating over space, we have

$$\int_\Omega \nabla \cdot \mathbf{T}(\mathbf{u}) \cdot \mathbf{q}\ d\Omega = \int_\Omega \mathbf{b} \cdot \mathbf{q}\ d\Omega\,. \tag{3.22}$$

Applying the Divergence Theorem, we get that

$$\int_\Omega -\mathbf{T}(\mathbf{u}) : \nabla\mathbf{q}\ d\Omega + \int_{\partial\Omega} \mathbf{T}(\mathbf{u})\mathbf{n} \cdot \mathbf{q}\ d\partial\Omega = \int_\Omega \mathbf{b} \cdot \mathbf{q}\ d\Omega\,. \tag{3.23}$$

By symmetry of $\mathbf{T}$, we can write $\nabla\mathbf{q} = \frac{1}{2}(\nabla\mathbf{q} + \nabla\mathbf{q}^T) = \epsilon(\mathbf{q})$. Thus,

$$\int_\Omega -\mathbf{T}(\mathbf{u}) : \epsilon(\mathbf{q})\ d\Omega + \int_{\partial\Omega} \mathbf{T}(\mathbf{u})\mathbf{n} \cdot \mathbf{q}\ d\partial\Omega = \int_\Omega \mathbf{b} \cdot \mathbf{q}\ d\Omega\,. \tag{3.24}$$

With the boundary condition that $\mathbf{T}(\mathbf{u})\mathbf{n} = 0$ on $\partial\Omega$, the final weak formulation is

$$-\int_\Omega \mathbf{T}(\mathbf{u}) : \epsilon(\mathbf{q})\ d\Omega = \int_\Omega \mathbf{b} \cdot \mathbf{q}\ d\Omega\,. \tag{3.25}$$

In FreeFEM, the boundary conditions for $\mathbf{u} = (u_x, u_y)$ (where u_x and u_y indicate the x and y components of the u, not partial derivatives) are incorporated by including "`+on(G0, ux=0, uy=0)`" inside the momentum balance problem.

Material convection. For the material convection, we apply a discontinuous-Galerkin method found in the FreeFEM manual [51]. The discontinuous-

Galerkin method is both faster and more stable than a typical finite difference (in time) convection operator. The details of the derivation are complex and can be found in [33]. The implementation details can be found in the FreeFEM manual [51].

3.3.2 Domain definition from MRI data

With spatial structure clearly having a significant role in cellular movement and mechanical dynamics, a realistic simulation domain is a crucial component in both 2D and 3D glioma models. We have implemented code to take in medical images, which are then processed and used in FreeFEM to define the simulation domain. In the specific simulations in this thesis, the image data is taken from example data provided by the software ExploreDTI [69]. ExploreDTI is a software that takes in DTI data files, allowing the user to explore the data visually as well as output various forms of the data. The sample data set provided by ExploreDTI has the same format as typical patient data, and thus the current numerical work flow would also be able to take in patient specific data.

Below, we outline the process of turning DTI data to a 2D simulation domain.

Export image from ExploreDTI. For our purposes of defining a simulation domain in 2D, we only need the general structure of the brain. In particular interest for our needs, the outer boundary of the brain tissue and the ventricles is sufficient for this work.

A First, in ExploreDTI, we load the DTI data file.

B Next, we select "`Image map`" → "`MD`" (mean diffusion) for visualization. Here, we use MD as it shows enough structure to specify the domain. Any image that has (or could be processed to have) significant contrast between the brain structures would be sufficient in this step. With the data provided, MD was the best option.

C Finally, the MD image is exported in an RGB format as a `.mat` file via "`Data`"→ "`Export current volume as RGB (*.mat)`"

Select layer from volume and convert to black and white image. The MD data exported from ExploreDTI is really a stack of 2D images that makes a "3D" image. As we are only interested in a 2D simulation domain at this point, we need to select one of these 2D "slices" from the MD data. The exported MD data is stored as matrix arrays. Thus, we can isolate a slice by selecting an element from this array. The choice of slice would be dependent on the desired purpose and possibly location of the tumor. Because we are using data assuming a healthy brain free of tumors, we don't need to consider the location of the tumor. The slice chosen for the current work was taken based on the clarity of the ventricles and maximizing the connectedness of each brain structure (i.e. no holes in ventricles or brain tissue).

With a suitable 2D slice isolated, there is a further step to process the data/image to maximize it's function in FreeFEM. The final destination of the domain image data is FreeFEM, which will use a package to identify isolines (lines that separate regions of different brightnesses). For this to function properly, a sufficient level of contrast is needed for the isolines delineating the brain structures to be identified. Therefore, a processing step that converts a low contrast image to a black and white version is used.

To achieve this output, the following steps are taken.

A In MATLAB load the MD data file. Isolate the desired slice (z-level) and set as a new variable (slice 36 for the data set used in this work). An example of the isolated slice is shown in Figure 3.1, panel 1.

B Alter this variable to make the values 0 or 1 depending on a threshold level where this threshold value is representing the brightness level. The choice of threshold value used is dependent on the input data with the goal being to capture the structures sufficiently. A threshold of 0.6 was used here. This outputs a black and white image which may still have some small unwanted artifacts, such as holes. We choose black and white specifically, as opposed to two other contrasting colors, as FreeFEM reads

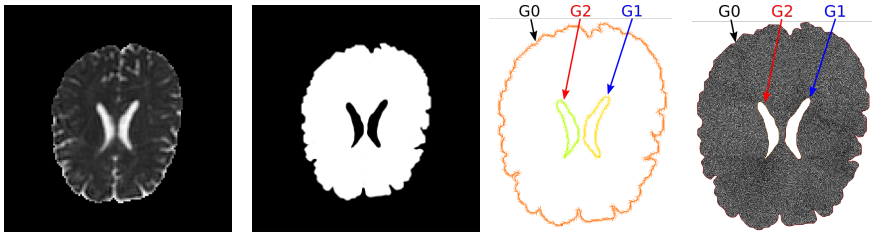

Figure 3.1: Steps of domain definition. *Left to right*: MD figure in ExploreDTI, black and white formatted figure (Inkscape output), isolines identified in FreeFEM, meshed domain in FreeFEM.

.pgm (portable gray map) files. With the data converted to 0's and 1's, we plot the altered data to get a black and white image and save this figure as a `.png` file.

C In Inkscape (or other image editing software), we open this .png to clean up any undesired spots within the brain domain as there may still be some spots left even with the thresholding. Furthermore, we change the size of the image to match the data. For the example data used here, the size should be 230x230 pixels. Finally, we export the brain figure to a `.png` file (See Figure 3.1, panel 2) and convert to a `.pgm` file.

Import image into FreeFEM and define numerical domain.
In FreeFEM the `.pgm` file is loaded and read. FreeFEM uses "`isoline`" to determine a specified number of closed curves (denoted by `Gi, i=0, 1, 2...`). It should be noted that FreeFEM requires a specific orientation of the line which is governed by the sign of the argument of `Gi`. Once the lines are specified, we build a function combining the lines to give the total domain (see Figure 3.1, panel 3). Finally we build a mesh in the domain (See 3.1, panel 4). To initialize the domain, run the FreeFEM code with "`bool BUILDMESHandVARIABLES =true;`" and "`bool RUNMODEL = false;`". By running this section of code, FreeFEM builds the mesh and also outputs the (x, y) spatial locations for each node in the mesh to a `.txt` file. This is needed to interpolate the DTI data in the Python code. The initial simulation domain and meshing are shown in detail in Figure 3.2.

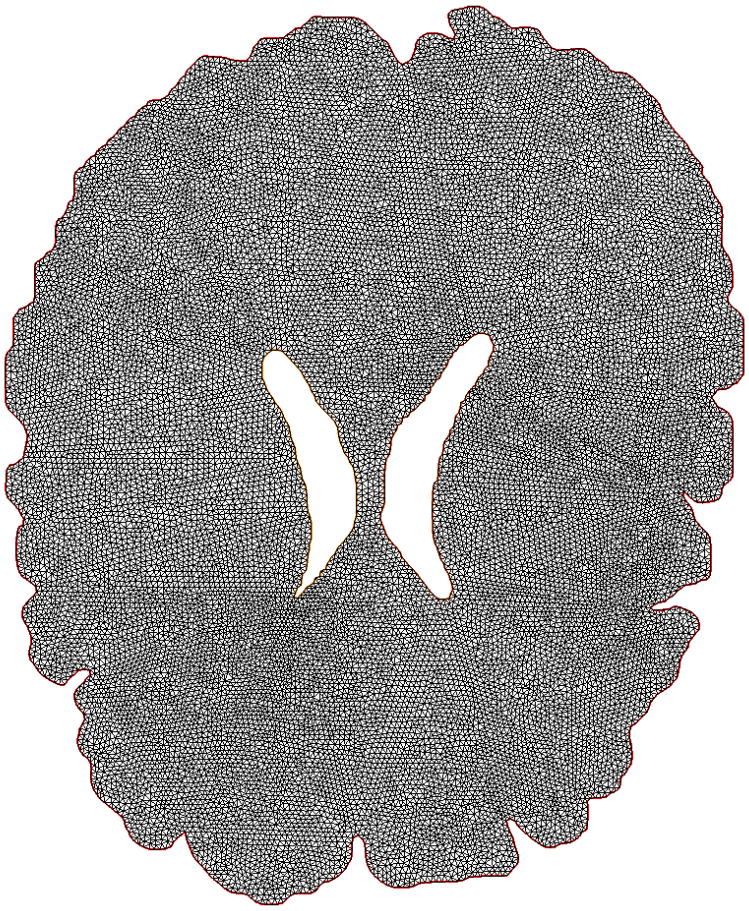

Figure 3.2: Initial simulation domain and mesh.

3.3.3 Diffusion tensor input from DTI data

Diffusion tensor translations and interpolation from DTI data. For the initial diffusion tensor elements, we import DTI data from the sample data file provided from ExploreDTI. First, following Swan *et al.* [116], the DTI data must be translated to cancer cell diffusion tensors. Next, the cancer cell diffusion tensors must be formatted to be applied to the FreeFEM mesh. Similarly to the exported MD data, the DTI data file stores data as matrix arrays. Hence, we can extract the data we need by isolating those data points. However, the DTI data is stored in matrices that correspond to the imaging voxels. Obviously these cubic voxels do not coincide with the finite element mesh generated in FreeFEM. Thus, we must interpolate the matrix DTI data in order to use it in FreeFem. Note that the mesh generated by FreeFEM is taken to be much finer than the DTI data grid. Therefore, there is no precision loss in the DTI interpolation step. This is achieved with the following procedure.

A In MATLAB load the DTI data and extract elements of diffusion tensor, D_{xx}, D_{xy}, D_{yy}.

B Translate the water diffusion tensor data to cancer diffusion tensors, $\mathbf{D}_c$, using the result from [115]:

$$\mathbf{D}_c = \frac{1}{\mu_{\text{turn}}} \int_\Omega \mathbf{v}\mathbf{v}^T q(\mathbf{x}, \mathbf{v})\ d\mathbf{v} \tag{3.26}$$

$$= \frac{1}{\mu_{\text{turn}}} Var[q] \tag{3.27}$$

$$= \frac{1}{\mu_{\text{turn}}} \left(\frac{1}{2} \left(1 - \frac{I_0(k)}{I_2(k)} \right) \mathbf{I} + \left(\frac{I_0(k)}{I_2(k)} \right) \boldsymbol{\gamma}\boldsymbol{\gamma}^T \right) \tag{3.28}$$

- μ_{turn} = turning rate (assigned)
- $\mathbf{v}$ = velocity
- q = turning distribution (bimodal Von Mises)
- $k(x) = \kappa$ FA where FA is the Fractional Anisotropy
  Note: κ is assigned, FA is taken directly from the DTI data file.

- $I_\nu(k)$ = modified Bessel functions of the first kind of order ν (Matlab has a function "`besseli`" for this)
- γ = unit vector (determined from DTI data)

An example of the tensor translation results is shown in Figure 3.3. The initial condition diffusion map elements for the two values of κ used in the following simulations, $\kappa = 10$ and $\kappa = 50$, are shown in Figure 3.4.

C Write these transformed D_c variables to a `.mat` file

D In Python import the D_{xx}, D_{xy}, D_{yy} variables. The (x, y) values of the nodes from the `.txt` file made by FreeFEM are also loaded. On the grid from the DTI data (defined by voxel size and matrix dimensions of diffusion tensor elements), interpolate the DTI data. For our case voxel size is 1.7969 mm and the matrix size is $128 \times 128 => x, y = [0, 230]$ mm (where pixels are equivalent to mm). For each FreeFEM mesh node point (x, y), specify the D_{xx}, D_{xy}, D_{yy} values using this interpolated data. This gives a vector of scalar values for each node (for each of D_{xx}, D_{xy}, D_{yy}). Save the D_{xx}, D_{xy}, D_{yy} values at each node to a `.txt` file (one file for each variable). This `.txt` file is then loaded in the FreeFEM code.

Initialization of diffusion tensor elements from interpolated DTI data. To initialize the variables and run the simulation, we compile the FreeFEM code with "`bool BUILDMESHandVARIABLES =true;`" and "`bool RUNMODEL = true;`". FreeFEM reads the .txt file containing the D_{xx}, D_{xy}, D_{yy} values at each node and defines the initial values of D_{xx}, D_{xy}, D_{yy} (D0, D1, D2 in FreeFEM) from this file. We now have a domain and diffusion tensor defined in FreeFEM using the DTI data. The other initial values $(c_0, u_0, v_0, \lambda_0, \mu_0)$ and simulation parameters are also specified at this point. Note that the FreeFEM code will write the initial conditions and simulation parameters to a .txt file (which are located in a folder created by the FreeFEM code if "`bool SaveData = true;`"). The model is then ready to be simulated on the domain with the remaining initial conditions as specified.

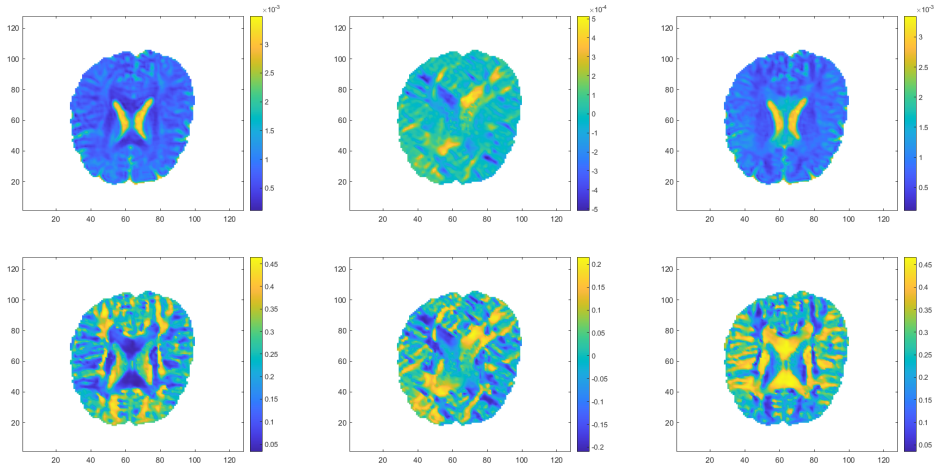

Figure 3.3: Diffusion tensor components determined from DTI data. Left to right: D_{xx}, D_{xy}, D_{yy}. *Top*: Raw DTI data. *Bottom*: Translated cancer diffusion tensors, $\mathbf{D}_c$, with $\kappa = 10$ and $\mu = 2$.

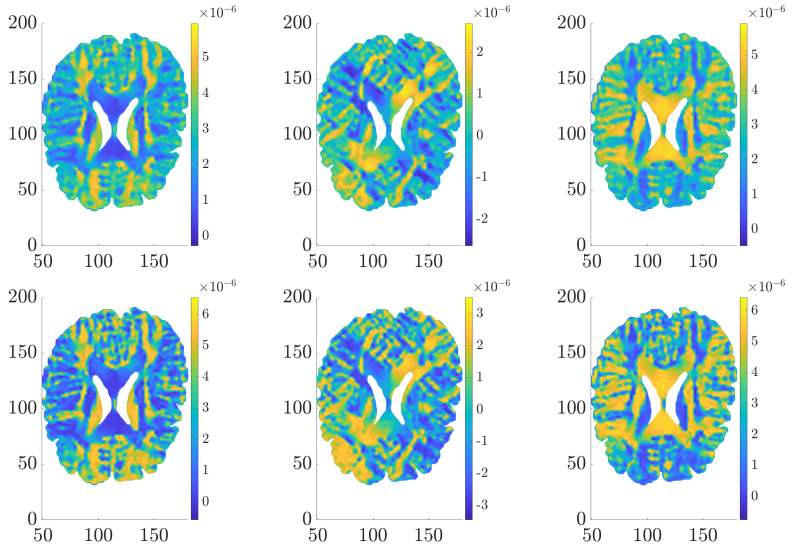

(a) D_{xx} **(b)** D_{xy} **(c)** D_{yy}

Figure 3.4: Translated diffusion tensor components used as initial conditions. *Top*: $\kappa = 10$. *Bottom*: $\kappa = 50$.

3.3.4 Model simulation outline

Definition of finite element spaces and functions. Any variable must be defined, along with it's associated test function. The test functions for each variable X (ie. $X = c, D0, \lambda, ...$) are denoted by qX. Each component of the deformation (u_x, u_y), velocity (v_x, v_y), and diffusion tensor (D_{xx}, D_{xy}, D_{yy}), are defined as their own variable as this simplified some of the calculations and made the variables easier to track. That is, for the diffusion tensor

$$D = \begin{pmatrix} D0 & D1 \\ \\ D1 & D2 \end{pmatrix}, \tag{3.29}$$

$D0, D1, D2 (= D_{xx}, D_{xy}, D_{yy})$ are their own variables that get convected. The variables $c, D0, D1, D2, ux, uy, vx, vy, f$, lambda and mu are defined as P1 elements, where *"[P1] piecewise linear continuous finite element (2d, 3d, surface 3d), the degrees of freedom are the vertices values." [51].*

Define the "problems". As noted previously, with coupled systems FreeFEM requires each equation to be defined as a problem. The order of problem definitions does not matter. The "problems" for the glioma model are

- The FAAD equation without reaction term. The reaction term is included explicitly in the time loop.
- The momentum balance (or elasticity) equation.
- Material property $(\lambda, \mu, D_{xx}, D_{xy}, D_{yy})$ convection.

Solve the system in a time loop. Finally, with the domain, initial conditions, etc. defined, the model is simulated by solving the system in a time loop. At each time step, the order is

1. Convect material properties (D0, D1, D2, lambda, mu)

2. Solve FAAD

3. Solve reaction term (ie. proliferation)

4. Solve Elasticity

5. Apply resulting deformation to mesh (via `movemesh`)

6. Adapt mesh with respect to cell density (optional step which may or may not be beneficial, depending on the specific simulation)

7. Restart time loop

Saving and visualizing the results. The results of the simulation can be saved at specified time intervals. The mesh, FE space, as well as each variable is saved in it's own file for each time point. These can be used to create plots in MATLAB. As this is time evolution data, gifs are a useful visualization tool and can be made from the .png figures produced by MATLAB using Python code. FreeFEM can also save .eps figure files for plots at specified time intervals, which can then be made into a .gif using Python code. However, these .eps files cannot be customized as nicely as the MATLAB produced .png files.

3.4 Results and discussion

In this section we present simulations of the glioma spread model in 2D. To explore the model dynamics, simulations with different initial conditions and parameter values are presented.

The data incorporated (domain and initial diffusion tensors) in the current simulations were taken from an example of a healthy brain and thus had no tumor present. To simulate a tumor, we define a normally distributed tumor cell density with small variance to indicate a small initial tumor size. Because the brain structure is spatially heterogeneous, we pick two different locations for the initial tumor to explore how the tumor development can be affected by location in the brain. We will call these locations "upper left" and "center right" (see top left panels of Figures 3.6 and 3.7). The locations were chosen

Table 3.1: Numerical simulation parameter values. Note that $\mu_{\text{turn}} = 10$ is only used in the simulations for Figure 3.12. All other simulations shown use $\mu_{\text{turn}} = 2$.

Parameter	Value(s)	Reference
Turning rate, μ_{turn}	2 $/s$	[115]
	10 $/s$	[115]
Anisotropy parameter, κ	10 (low)	[115]
(unitless)	50 (high)	[115]
Proliferation rate, ρ	0.0006 $/d$ (low)	[42]
	0.1 $/d$ (high)	[54]
Bulk modulus, λ	6.5 kPa	[54]
Shear modulus, μ	0.7 kPa	[54]
Body force parameter, p	0.1 kPa (low)	
	1 kPa (high)	

as they have very different positions with respect to the ventricles; the upper left will grow into the tip of a ventricle, while the center right will grow into the side of a ventricle. These locations were also chosen to be positioned far enough away from the ventricles and outer brain boundary to allow for some development before encountering these structures. Of course, realistically, a tumor could start at any location in the brain. These simulations could be easily adapted to initialize a tumor based on patient data as was accomplished in Swan *et al.* [116].

The model parameters for the numerical simulations are given in Table 3.1. Note that λ, μ, and p are given in kPa which has units $\frac{kg}{mm \cdot s^2}$. Thus, λ, μ, and p are multiplied by $(60 \cdot 60 \cdot 24)^2$ to convert the time units to days.

The diffusion tensor elements are taken in from the DTI data which has units mm^2/s. We convert the diffusion data units to days by multiplying by $60 \cdot 60 \cdot 24$. The raw DTI values are translated using the bimodal von Mises distribution, where we borrow μ_{turn} and κ values from [115]. Note that the value of μ_{turn} given in Table 3.1 is in units $/s$, and thus we multiply by $60 \cdot 60 \cdot 24$ to convert to $/d$.

In the following sections, we will show select simulation elements in order

to focus in on particular results of the model. Note that the simulations terminated once ventricle closure occurred (i.e. when two points on the ventricle boundary came in contact with each other). We refer to the time this occurs as the simulation "outcome". Figure 3.2 shows the initial simulation domain with mesh, while Figure 3.4 shows the initial diffusion tensor components. For a full understanding of the model and simulation outputs Figure 3.5 shows plots of a variety of the model components at time $t = 50$.

Figure 3.5a shows the cell density which seems to be causing deformation a large distance from the tumor boundary. What is not clearly visible in the figures, but can be seen while the simulations are running, is that there is a "halo" of tumor cells surrounding the visible tumor region. This "halo" is a ring of very low density of tumor cells which are not easily seen. The next panel, Figure 3.5b is used to enhance the visibility of this low density tumor region by setting a threshold of $c = 0.001$ and plotting using a black and white color scheme. That is, this "cell boundary" plot shows the regions where $c > 0.001$ in white. From the cell boundary plot, it is clear that the tumor front is much further than can be seen in Figure 3.5a, showing that the tumor is effectively much closer to the ventricles than seen in Figure 3.5a.

Panels 3.5d-3.5f show the elements (D_{xx}, D_{xy}, D_{yy}) of the diffusion tensor $\mathbf{D}$. Panels 3.5g-3.5i show the displacement in the x and y directions, as well as a plot of the vector $\mathbf{u}$, while panels 3.5j-3.5l show the corresponding elements for the velocity.

Figures 3.6 and 3.7 show a time evolution for tumors initiated in the upper left and right center locations, respectively. Although not shown for most simulations, the elements of the diffusion tensor, D_{xx}, D_{xy}, D_{yy}, evolve with the tissue deformation in all simulations. Figure 3.8 shows an example of the evolution of these diffusion tensor elements.

Next, we study the effect of our model parameters.

Effect of proliferation rate, ρ. Figures 3.9 and 3.10 show the effects of changing the value of ρ for the upper left and center right initial tumor location, respectively. Not unsurprisingly, increasing the value of ρ increases the rate of growth of the tumor, with the time to ventricle closure being much shorter

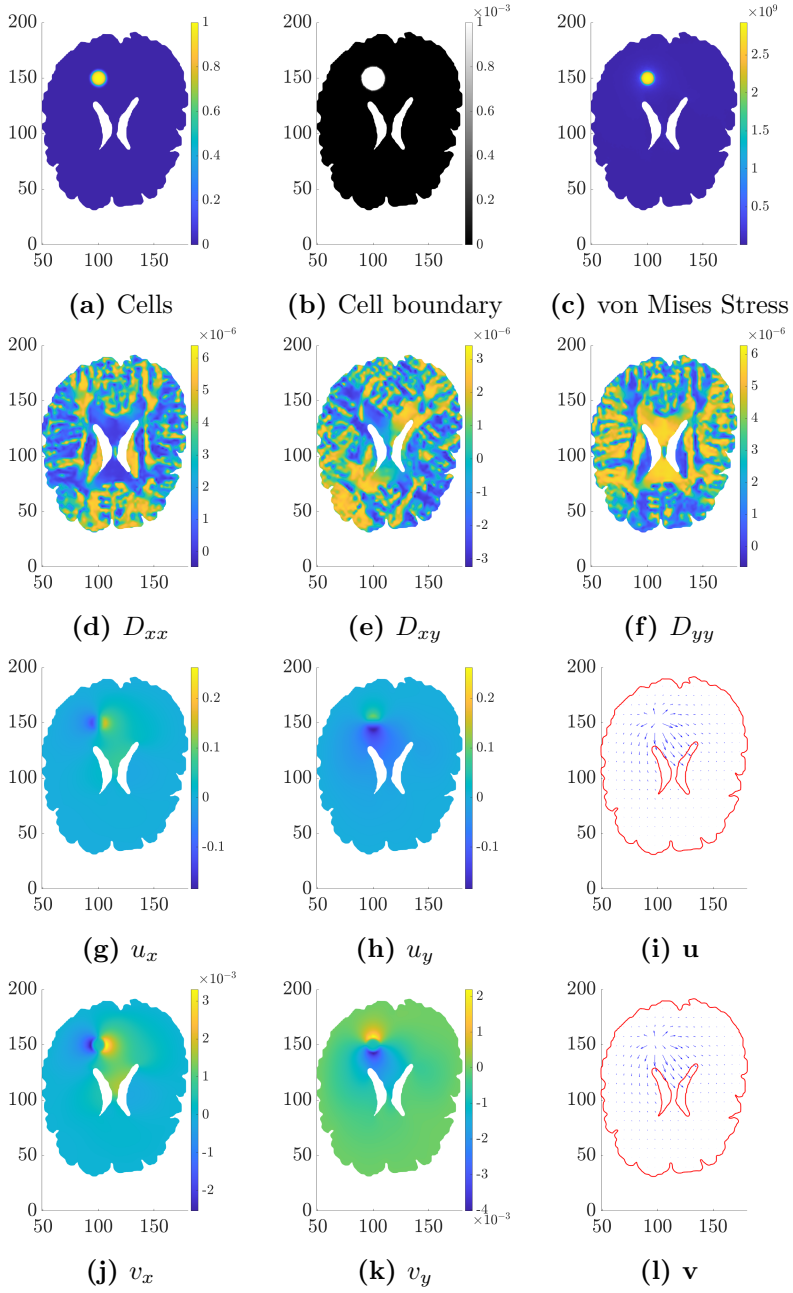

(a) Cells **(b)** Cell boundary **(c)** von Mises Stress

(d) D_{xx} **(e)** D_{xy} **(f)** D_{yy}

(g) u_x **(h)** u_y **(i)** **u**

(j) v_x **(k)** v_y **(l)** **v**

Figure 3.5: Examples of plot types at time 50 where $\kappa = 50, \rho = 0.1, \lambda = 6.5, \mu = 0.7, p = 1$.

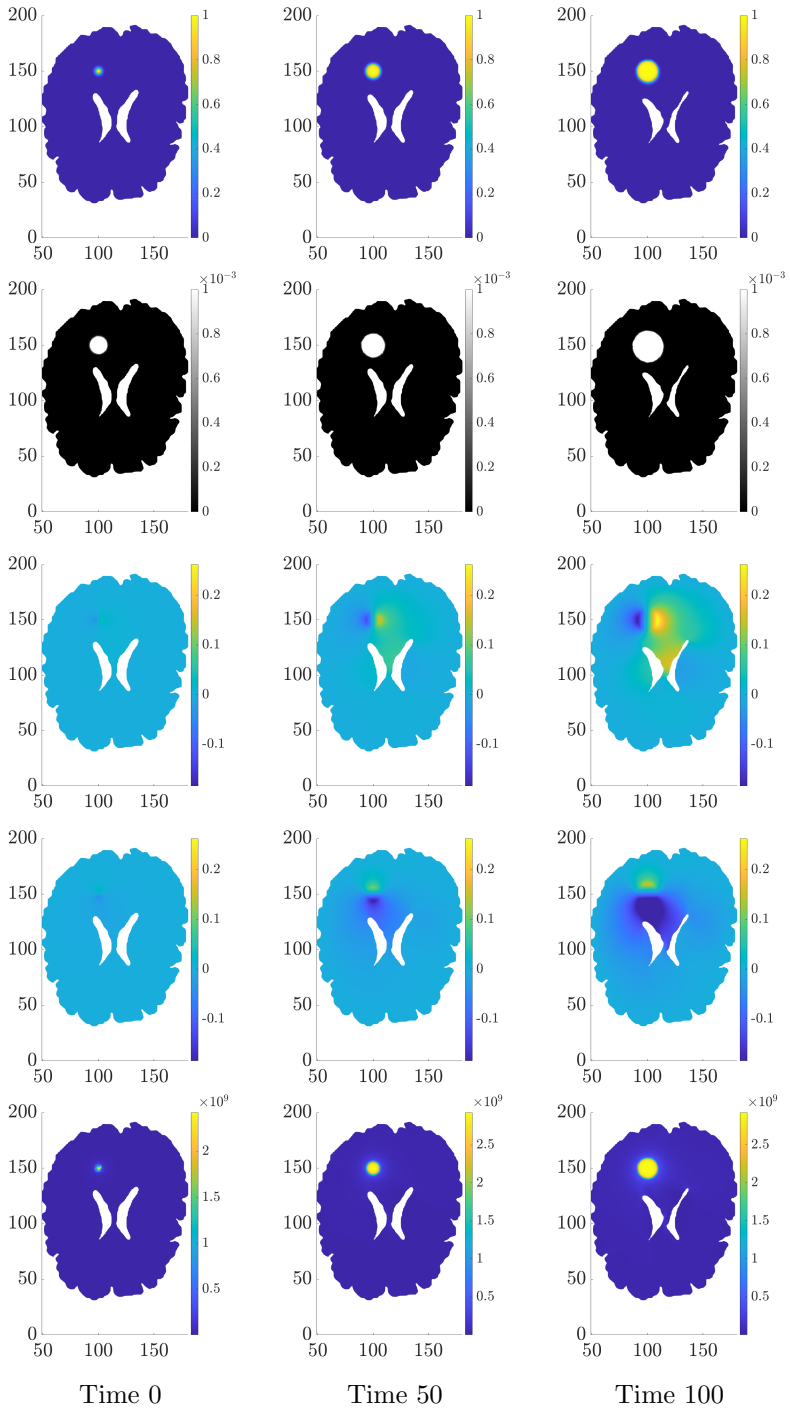

Figure 3.6: Simulations for upper left initial tumor location with $\rho = 0.1, \lambda = 6.5, \mu = 0.7, p = 1, \kappa = 50$. *Top to bottom:* Cell density, boundary for low cell density (0.001) tumor front, u_x, u_y, von Mises stress.

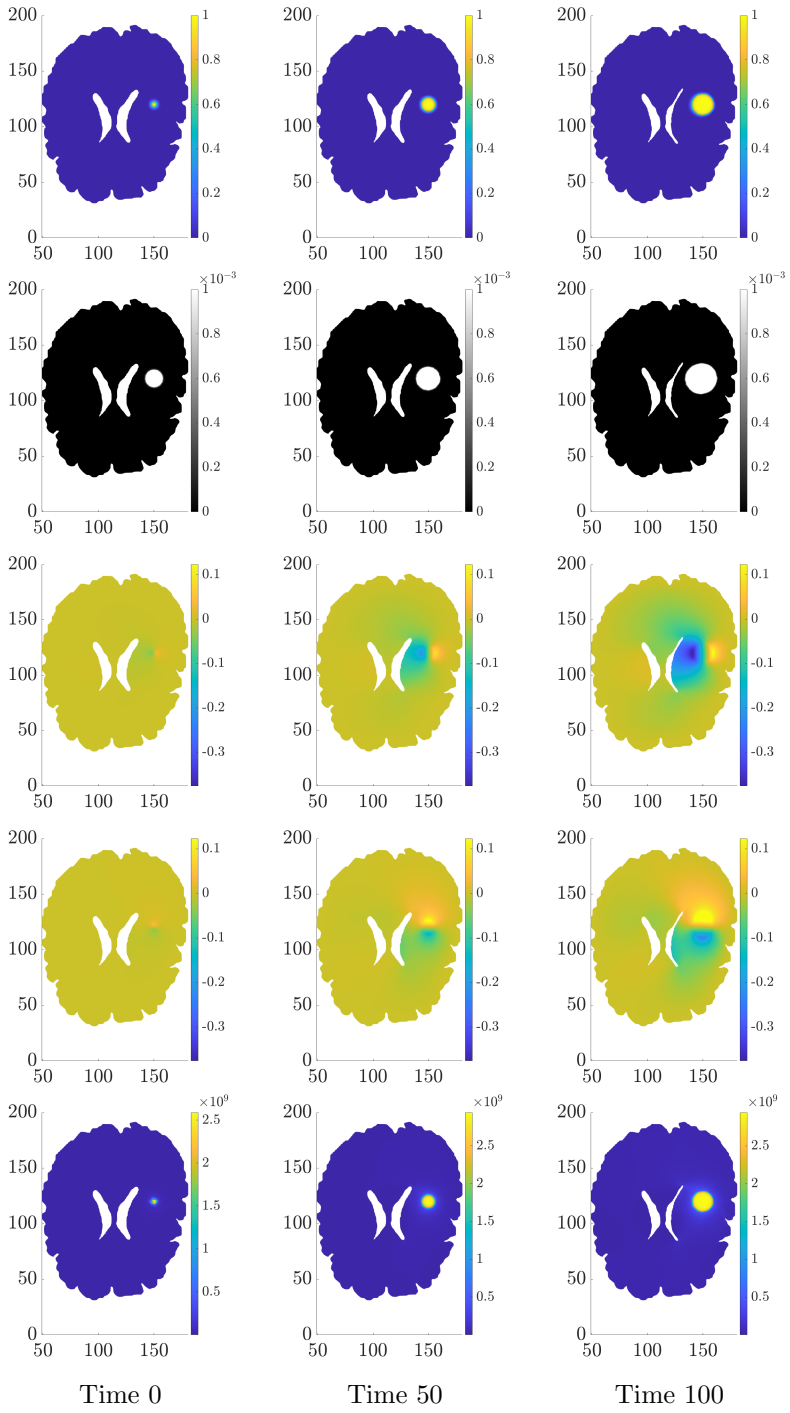

Figure 3.7: Simulations for center right initial tumor location with $\rho = 0.1, \lambda = 6.5, \mu = 0.7, p = \lambda + 2\mu, \kappa = 50$. *Top to bottom:* Cell density, boundary for low cell density (0.001) tumor front, u_x, u_y, von Mises stress.

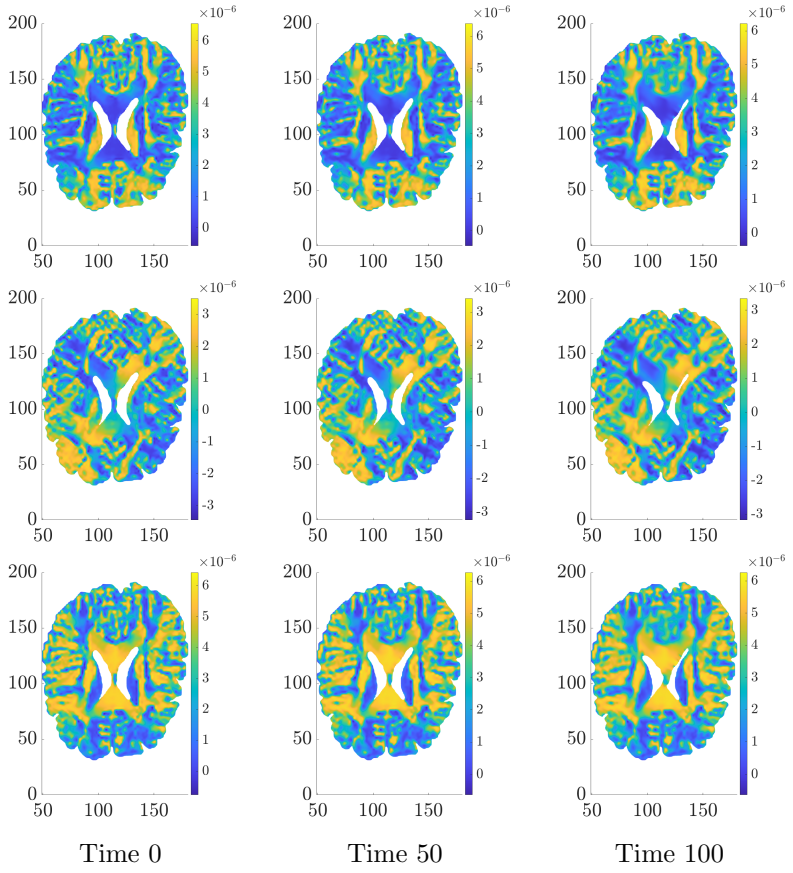

Figure 3.8: Evolution of diffusion tensor elements over time with upper left initial tumor and $\rho = 0.1, \lambda = 6.5, \mu = 0.7, p = 1, \kappa = 50$. *Top*: D_{xx}. *Middle*: D_{xy}. *Bottom*: D_{yy}.

for the high ρ case. Furthermore, the size of the tumor is also larger at the time of ventricle closure, with a larger region of tumor cells in the high ρ case. The relative difference between the final sizes of tumor in the high and low ρ simulations appears to depend on the initial location of the tumor. Comparing the upper left and center right initial locations, there is a larger discrepancy between the low and high ρ final tumor sizes in the upper left case. This can especially be seen in the black and white tumor boundary figures. The maximum tumor density is also increased in the high ρ case, with the smaller ρ simulation having a maximum density significantly below 1, while the high ρ tumor retains a region with maximum density.

In addition to the variations in cell density between high and low ρ simulations, there are also notable differences in the mechanical elements of deformation and stress. The higher ρ value results in larger magnitude deformations, as well as an increased magnitude and region of stress, compared to the low ρ simulations.

Effect of the anisotropy parameter, κ, and turning rate, μ_{turn}. Within the parameter regimes used in this work, the results for the $\kappa = 10$ and $\kappa = 50$, and $\mu_{\text{turn}} = 2$ and $\mu_{\text{turn}} = 10$, simulations are indistinguishable in terms of cell density, deformation, and stress. This may be due to the non-vanishing part of the diffusion tensor in equation (3.28).

Effect of body force scaling parameter, p. One component of the model that appears to greatly alter tumor spread dynamics is the body force function parameter p. As described in Section 3.2, p scales the magnitude of the body forces. This parameter could be tuned to each patient, but without any particular data, there is no way of knowing exactly what this value should be. In [54] (where p_1 from Chapter 2 is equivalent to p) and [114], a value for the scaling factor of the forcing function was chosen without justification. Thus, examining the impacts of changing the value of p is a worthwhile pursuit. A larger value of p means the tumor cells cause a larger force. Thus, with a larger value of p the tumor can more easily deform the surrounding tissue. In this section, we discuss the effects of changing p on the size of tumor, spread

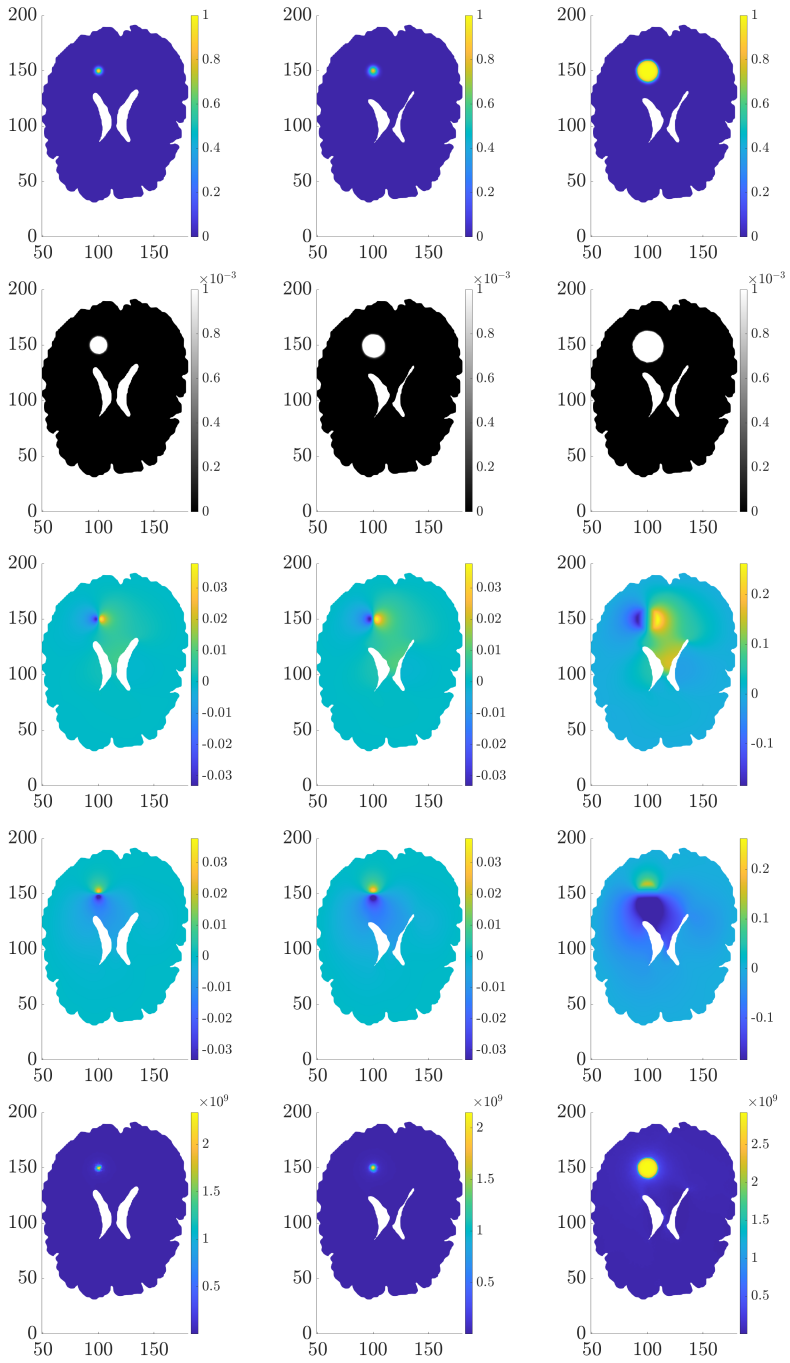

Figure 3.9: Comparison of model outcomes with the upper left tumor location where $\lambda = 6.5, \mu = 0.7, p = 1, \kappa = 50$. *Left to right*: Initial condition, time 1000 with low ρ ($\rho = 0.0006$), time 100 with high ρ ($\rho = 0.1$). *Top to bottom:* Cell density, boundary for low cell density ($c > 0.001$) tumor front, u_x, u_y, von Mises stress.

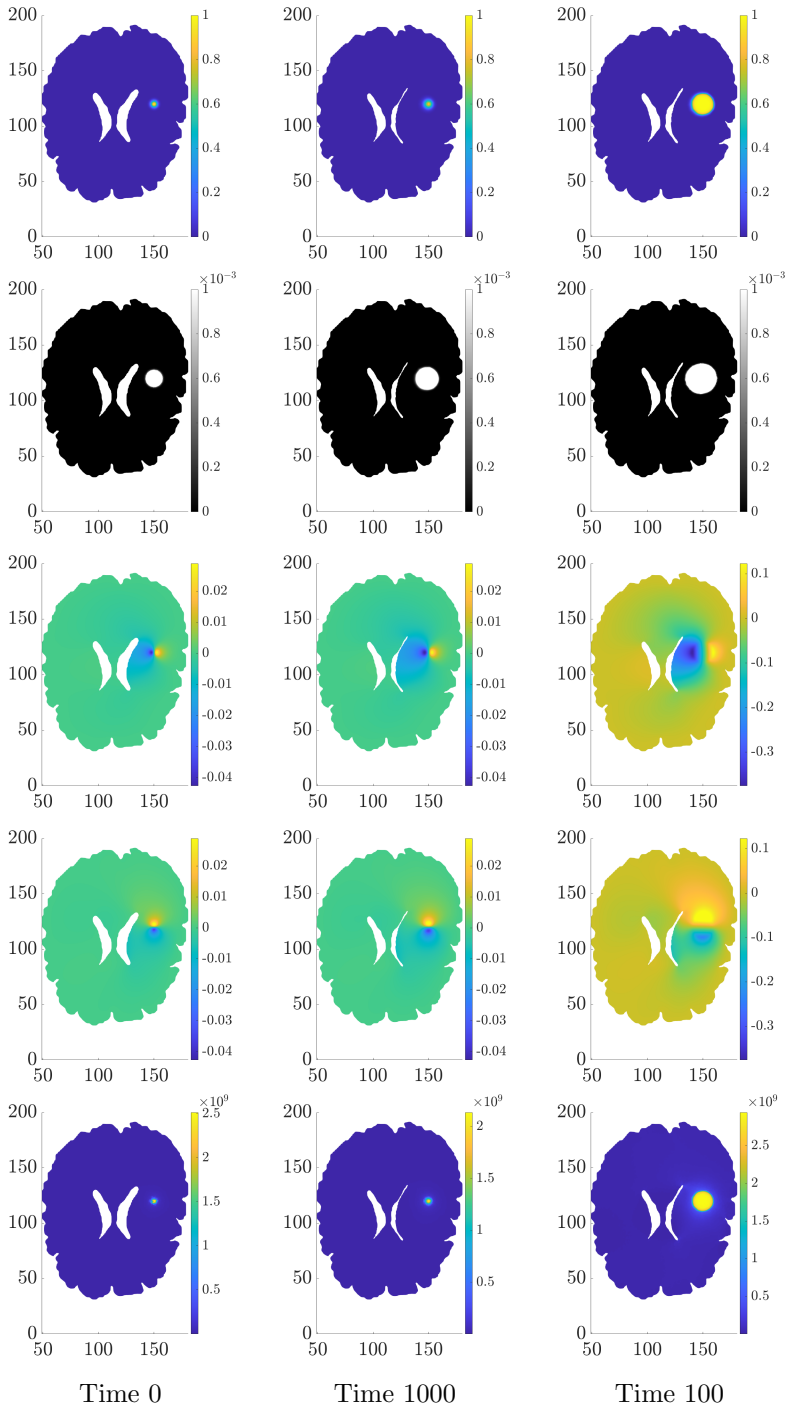

Figure 3.10: Comparison of model outcomes with the center right tumor location where $\lambda = 6.5, \mu = 0.7, p = 1, \kappa = 50$. *Left to right*: Initial condition, time 1000 with low ρ ($\rho = 0.0006$), time 100 with high ρ ($\rho = 0.1$). *Top to bottom:* Cell density, boundary for low cell density ($c > 0.001$) tumor front, u_x, u_y, von Mises stress.

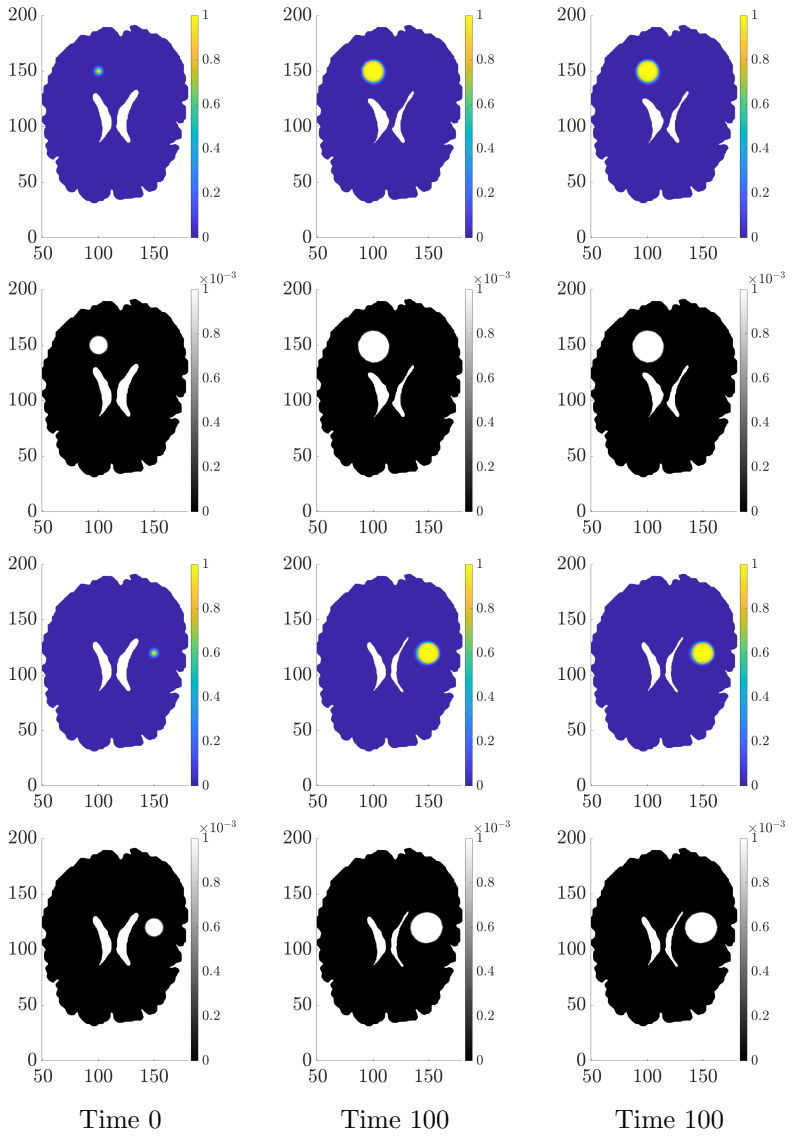

Figure 3.11: Comparison of simulations with different κ values for upper left and center right initial tumor locations where $\rho = 0.1, \lambda = 6.5, \mu = 0.7, p = 1$. *Left to right*: Initial condition, $\kappa = 10$, $\kappa = 50$.

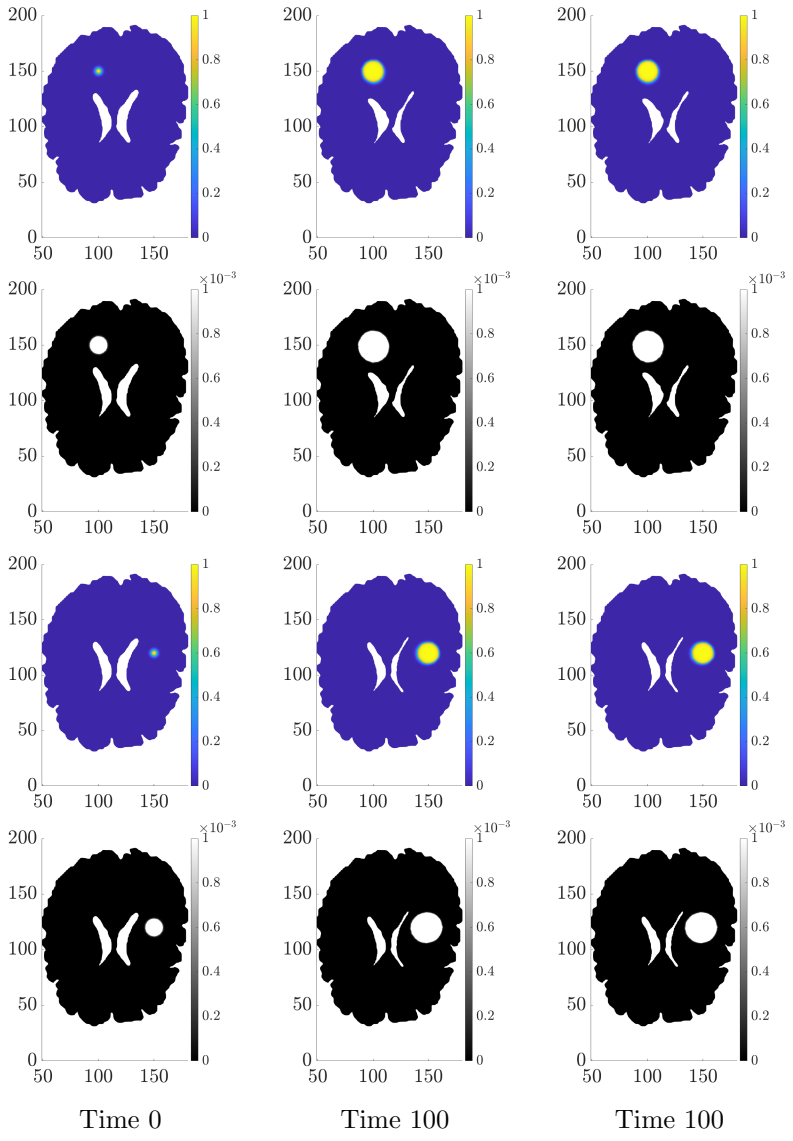

Figure 3.12: Comparison of simulations with different μ_{turn} values for upper left and center right initial tumor locations where $\rho = 0.1, \lambda = 6.5, \mu = 0.7, p = 1, \kappa = 50$. *Left to right*: Initial condition, $\mu_{\text{turn}} = 2$, $\mu_{\text{turn}} = 10$.

speed, as well as mechanical effects such as deformation and stress.

Figures 3.13 and 3.15 show the effect of changing the value of p on cell density and stress for the upper left and center right initial tumor locations, while Figures 3.14 and 3.16 show the differences in deformation for the same simulations.

As is clear in the cell density panels of Figures 3.13 and 3.15, the final tumor size at the time of ventricle closure is much larger in the low p case. Furthermore, the time to ventricle closure is much longer with low p. We can also see that the shape of the tumor is much more irregular in the low p case, with the high p case leading to a nearly spherical tumor shape. An approximately spherical tumor shape was also seen in earlier simulations which have approximately the same of even higher p.

Due to the spherical shape of the initial tumor, without any external influences, the tumor will naturally grow spherically. However, in this system there are also the effects of diffusion that can cause more asymmetrical growth, but the diffusion values used here seem to be taken over by the proliferation rate. With respect to p, an explanation for an increasing regularity in the shape of the tumor with increasing p value is that the tumor cells cause more deformation for higher values of p, resulting in less resistance to tumor spread. Without a significant resistance to deformation (i.e. high p value), the tumor is able to push the healthy tissue and grow (mostly) spherically. With an increase in resistance (i.e. low p value), the tumor cannot easily deform the surrounding tissue and spread is more affected by the other structures in the brain, such as the ventricles.

We can also see that the stress from tumor cell growth is similarly altered between high and low p. The simulations with high p reach stresses an order of magnitude higher than the low p simulations. However, corresponding to the larger tumor, the size of area experiencing significant stress is much larger with the low p value. This trend of higher magnitude but smaller region of effects with high p carries through to the deformation $\mathbf{u} = (u_x, u_y)$ (see Figures 3.14 and 3.16).

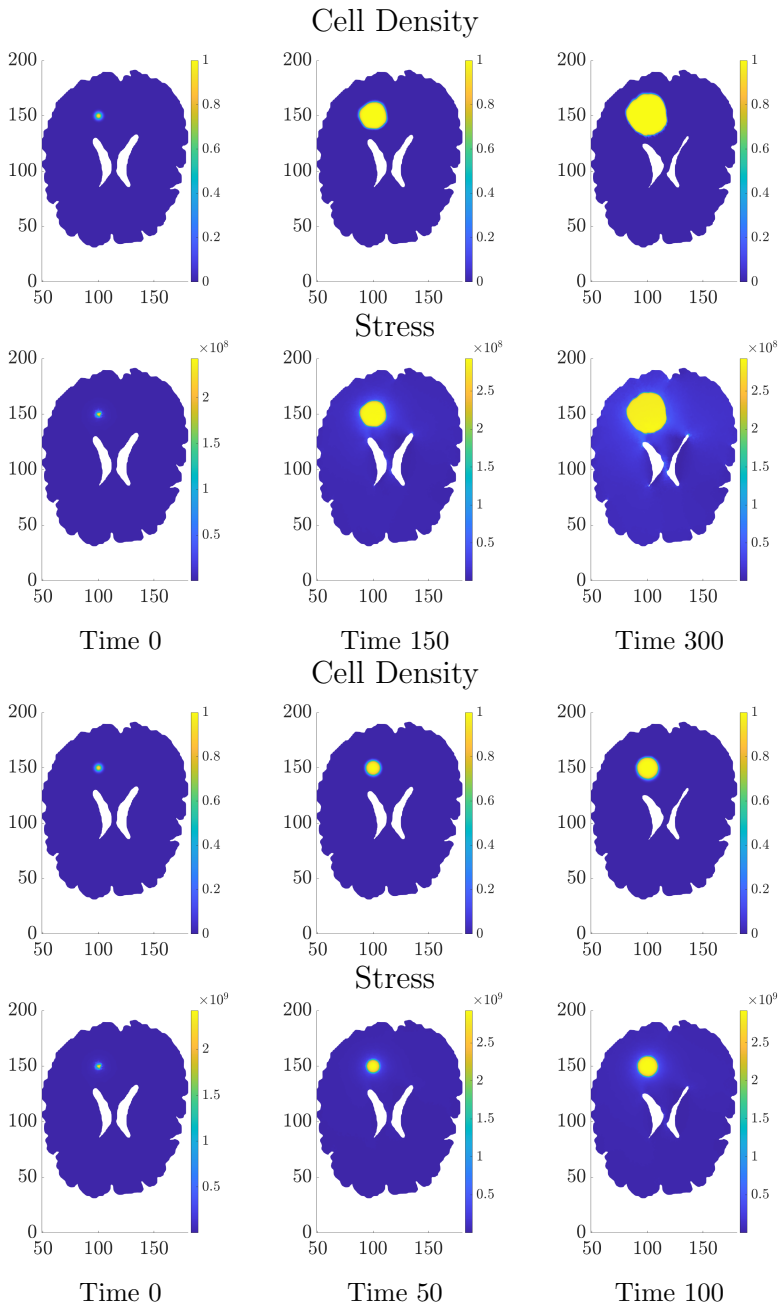

Figure 3.13: Comparison of cell density and stress for upper left initial tumor location with $p = 0.1$ (*top*) and $p = 1$ (*bottom*). For both simulations, $\lambda = 6.5$, $\mu = 0.7$, $\rho = 0.1$, $\kappa = 50$. Notice the different time and stress scales between the high and low p plots. The final time shown is the time of ventricle closure ($t = 300$ for low p, $t = 100$ for high p). The middle column shows an intermediate time step.

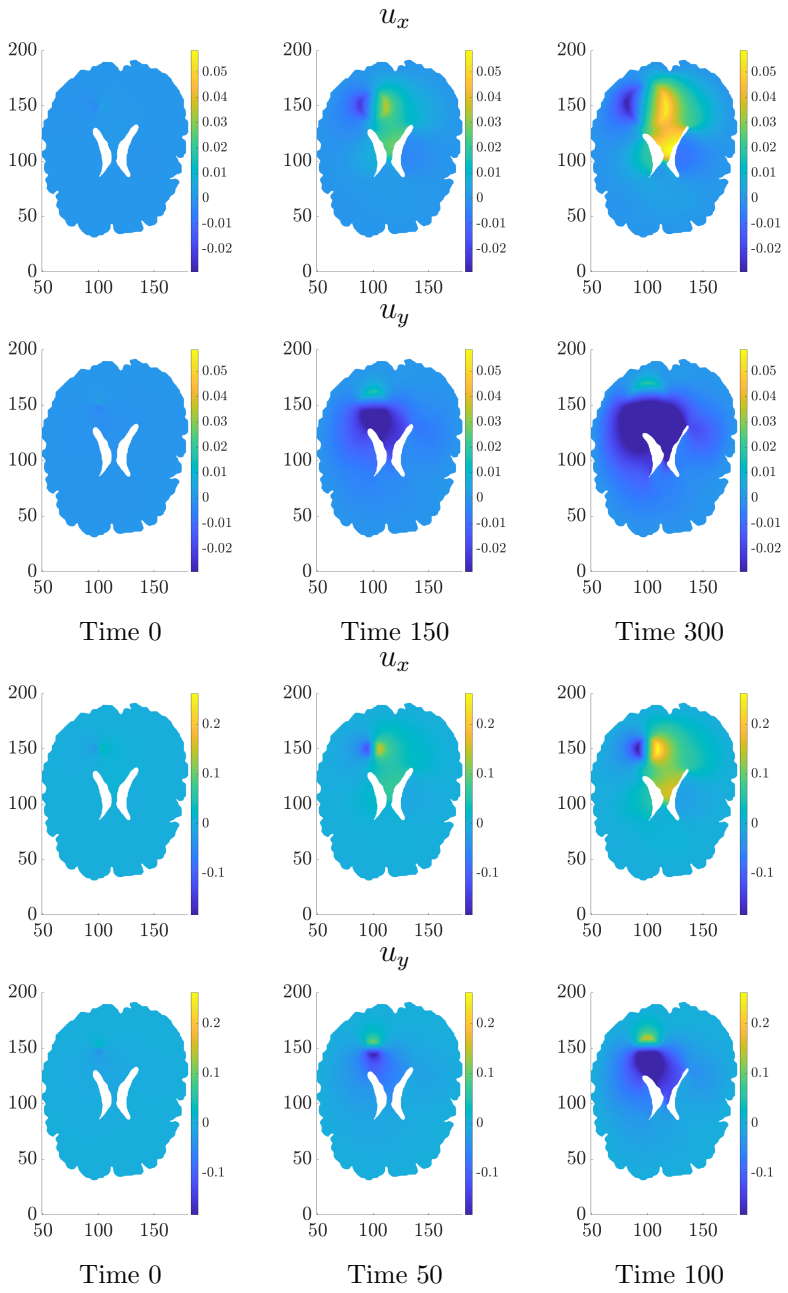

Figure 3.14: Comparison of deformation for upper left initial tumor location with $p = 0.1$ (*top*) and $p = 1$ (*bottom*). For both simulations, $\lambda = 6.5$, $\mu = 0.7$, $\rho = 0.1$, $\kappa = 50$. Notice the different time and stress scales between the high and low p plots. The final time shown is the time of ventricle closure ($t = 300$ for low p, $t = 100$ for high p). The middle column shows an intermediate time step.

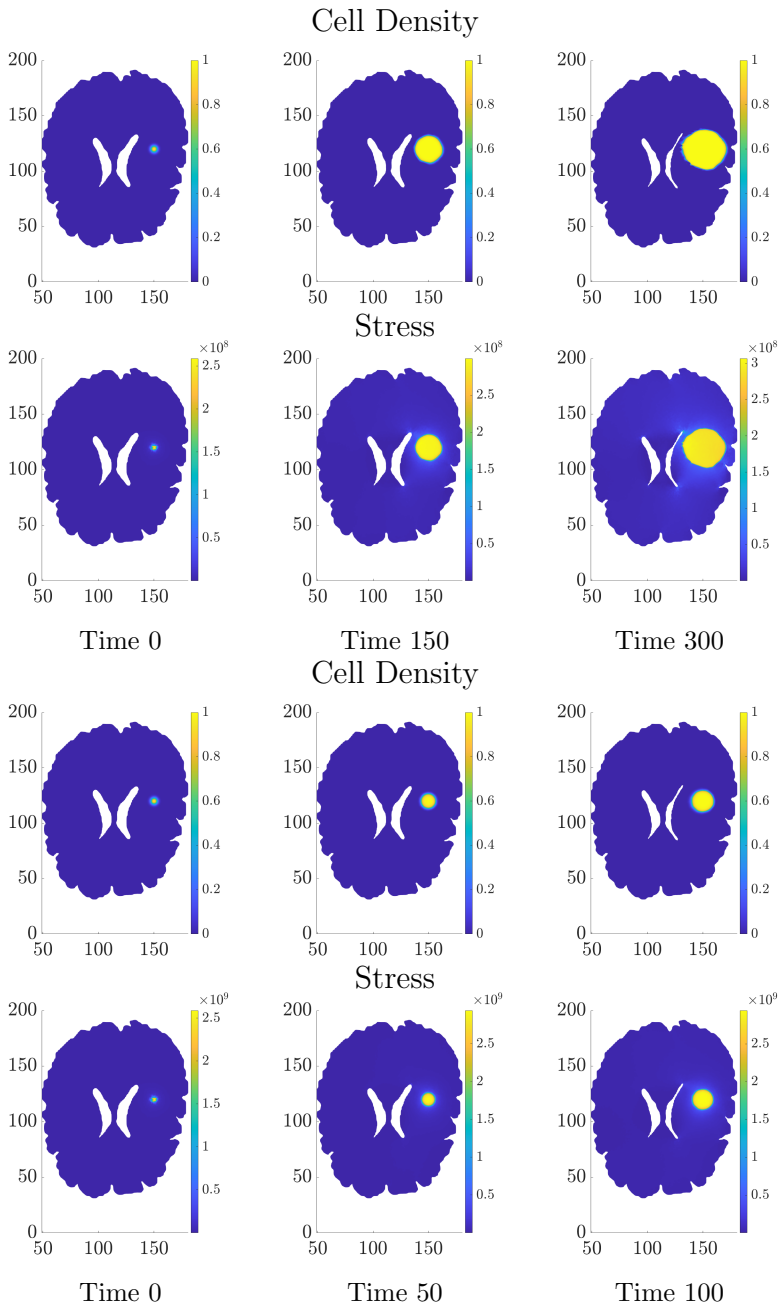

Figure 3.15: Comparison of cell density and stress for center right initial tumor location with $p = 0.1$ (*top*) and $p = 1$ (*bottom*). For both simulations, $\lambda = 6.5$, $\mu = 0.7$, $\rho = 0.1$, $\kappa = 50$. Notice the different time and stress scales between the high and low p plots. The final time shown is the time of ventricle closure ($t = 300$ for low p, $t = 100$ for high p). The middle column shows an intermediate time step.

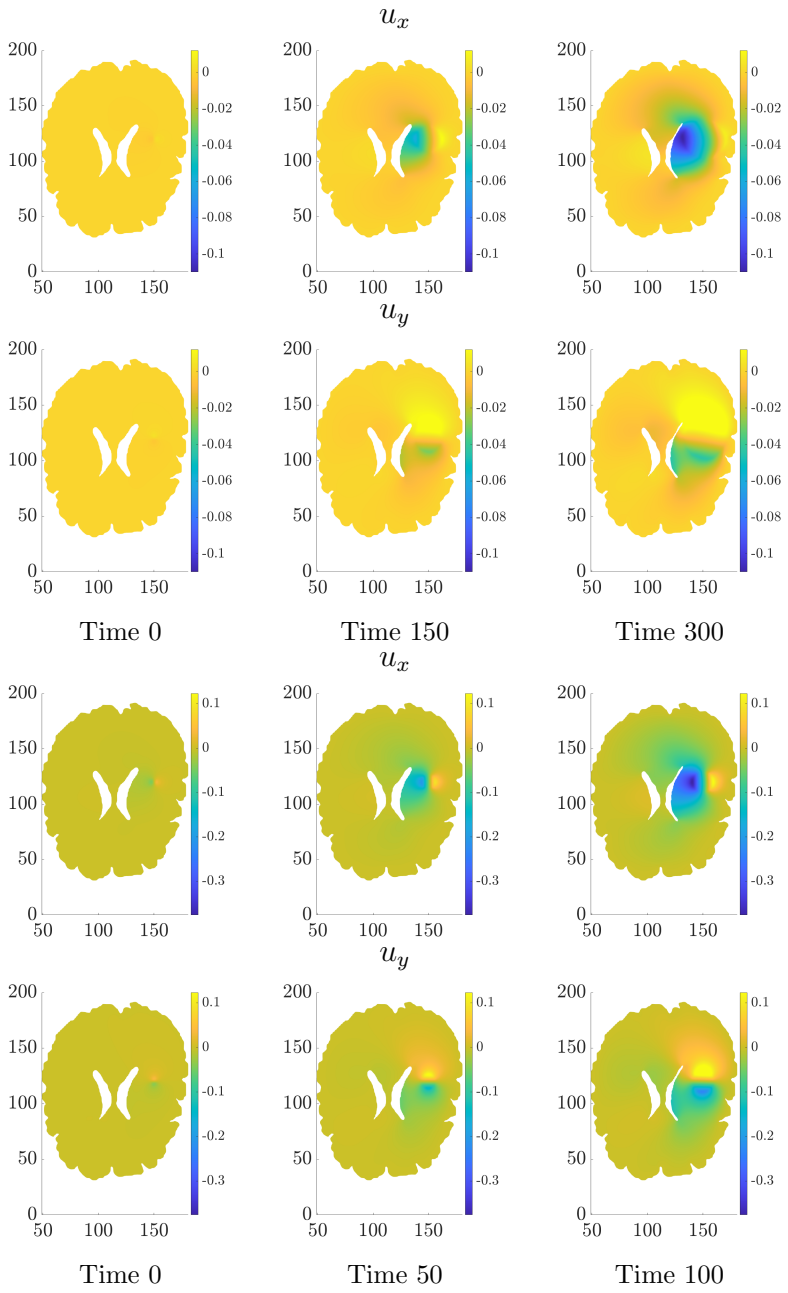

Figure 3.16: Comparison of deformation for center right initial tumor location with $p = 0.1$ (top) and $p = 1$ (bottom). For both simulations, $\lambda = 6.5$, $\mu = 0.7$, $\rho = 0.1$, $\kappa = 50$. Notice the different time and stress scales between the high and low p plots. The final time shown is the time of ventricle closure ($t = 300$ for low p, $t = 100$ for high p). The middle column shows an intermediate time step.

3.5 Conclusion

In this chapter we developed a fully anisotropic glioma spread model in 2D with brain mechanics modeled by linear elasticity. Using this model as a foundation, we can build in more realistic elasticity models, such as the Ogden model, in the future.

We have also developed a data pipeline capable of taking in medical imaging data, which is then registered, discretized, and interpolated, including the structures such as the ventricles and skull. Along with sample imaging data, we have included the most realistic parameters available from the literature.

In proof-of-concept simulations, we are able to show the model predicts reasonable outcomes, such as tumor growth and deformation, over reasonable time scales. Through these test-simulations, we have analyzed the dependence of the model on parameters. The variation of the growth rate, ρ, had the expected effect, with increasing ρ increasing the spread rate and size of the tumor. Varying either the anisotropy parameter, κ, or the turning rate, μ_{turn}, seemed to have a negligible impact on glioma spread, although this may be dependent on the full parameter set. It may be that the effects the diffusion are overtaken by the effects of the mechanics. The final parameter considered is the body force parameter, p. This parameter plays a significant role in the range, shape, and mechanical impacts of a growing glioma. With p heavily affecting the model outcomes, it is important to accurately determine what this value is in reality. More biological data is needed to estimate the size of the forces generated by a growing tumor.

As noted throughout, the imaging data used in this work was limited to a data set from ExploreDTI. A next step would be to fit this model to patient data when it becomes available. Our model is a further step to more complete, realistic glioma modelling. We will conclude our discussion of the 2D glioma model by outlining possible avenues of future work that would be beneficial to making a more accurate glioma model.

Add fluid physics to ventricles. One aspect that we had hoped to include was the addition of a physical model for the interior of the ventricles.

Currently, the dynamics of the 2D model are limited to the brain tissue. This extension should be possible by coupling the dynamics of the brain tissue with a fluid model inside the ventricles.

Extend to 3D. Another clear next step is to extend this work to 3D. Within the FreeFEM framework, this should not be too difficult. The most significant changes to the code would be altering particular macro operators used in the "Problems". Running the solvers themselves is actually quite trivial to alter to 3D. The other factor that would need to be considered when jumping to 3D is the data input. For the DTI data, it is likely there would just be another layer of interpolation needed in the added dimensions. The largest issue would likely come from the domain definition. The method used in this work identifies closed curves in a 2D image. At this point, it is not clear is there is a way of extending this to surfaces in a 3D domain. Another option could be to simply stack 2D simulations to give a quasi-3D simulation, although the dynamics would be somewhat unrealistic as the interactions in the 3rd dimensions would not be included.

Consider other elastic models. In the 2D glioma model section, we limited our results to the linear elasticity model. This was in large part due to the limitations of the finite element software. With the requirement that the momentum balance equation be formulated in the weak form, we could not find a way to employ the one-term Ogden model. It may be that FreeFEM is not the best tool for this model and other numerical methods or software, such as COMSOL, are required. The numerical schemes used in [54] include Strang operator splitting and fictitious domain methods. Similarly, [114] employed Strang operator splitting and pseudo-spectral methods on a fictitious domain. Of course, there is also the possibility of exploring other elasticity models, however, this would be ignoring the best data we have showing that the one-term Ogden model is the most appropriate model of brain tissue.

Include real patient data and quantify accuracy. As detailed in Section 3.3, we have developed a numerical work flow capable of incorporating patient-

specific data to define the simulation domain and diffusions tensors. However, at the point of simulating we did not have access to real patient data. As was carried out by [116], it would be a worthwhile step to simulate patient data and quantify the model accuracy through measures such as the Jaccard score. A further aspect that could be taken from patient-specific data is the initial tumor density. In this work we only specified initial tumor densities, but this could be fit to a patient. This has been carried out in previous works by [116].

Fit p. As discussed earlier, there is currently no reason to use a particular value of p–it is just chosen to give a reasonable level of deformation. With how significantly this parameter alters the pattern of tumor spread in this model, determining a way to fit this parameter to patient data would be a highly useful extension.

Chapter 4

Trajectory tracing in figure skating

This chapter has been published as

[103] Meghan Rhodes, Vakhtang Putkaradze, Trajectory tracing in figure skating. Nonlinear Dynamics, 2022,
https://doi.org/10.1007/s11071-022-07806-8.

Abstract

In this work, we model the movement of a figure skater gliding on ice by the Chaplygin sleigh, a classic pedagogical example of a nonholonomic mechanical system. The Chaplygin sleigh is controlled by a movable added mass, modeling the movable center of mass of the figure skater. The position and velocity of the added mass act as controls that can be used to steer the skater in order to produce prescribed patterns. For any piecewise smooth prescribed curve, this model can be used to determine the controls needed to reproduce that curve by approximating the curve with circular arcs. Tracing of the circular arcs is exact in our control procedure, so the accuracy of the method depends solely on the accuracy of approximation of a trajectory by circular arcs. To reproduce the individual elements of a pattern, we employ a control mechanism based on minimization of the energy of control mass. We conclude by reproducing

a classical "double flower" figure skating pattern and compute the resulting controls.

4.1 Introduction

Figure skating is a popular sport worldwide with competitions taking prime time television spots on major networks, with the combination of athleticism and artistic performance making the sport appealing to a broad audience. Underlying the entertaining performances are technical and complex principles from mathematics and physics. Originating in the 19th century, skating derives its name from the patterns, or "figures", carved into the ice while skating. Ice skating hobbyists would design intricate patterns and attempt to recreate them on the ice as precisely as possible. An example of such as a design is shown in Figure 4.1 [1]. As the hobby grew into a sport and ice skate technology advanced, spins and jumps were included in the broadened term of figure skating. The sport of figure skating developed, with categories being made for different forms of figure skating. The name "compulsory figures" was given to the process of tracing specific patterns on the ice. During testing and competitions, compulsory figures are judged on precision, accuracy, and edge quality (smooth sliding and no grinding), among other metrics. Until 1991, compulsory figures were a required component in competition [47]. Although compulsory figures may be less visually spectacular and less athletically challenging compared to the Olympic-style events, performing a precise and complex pattern on the ice requires significant control and technical skill. The compulsory skating was eventually excluded from the standard figure skating competitions and broke off into its own category. Competitions in compulsory figures are held independently and the athletes have their own rankings, independent of the mainstream figure skaters.

Previous mathematical models and descriptions of figure skating have followed this trend in the popularity free style skating, mainly focusing on modeling jumping [50, 58, 59, 61, 108]. Considering ice skating more generally,

[1] `https://qph.fs.quoracdn.net/main-qimg-b0f3b3d2115f1e1fa1720b7c3733e0bc`

Figure 4.1: Figure skating pattern on ice.

much attention has been dedicated to the modeling of a skate's blade gliding on ice with a focus on the friction resulting from ice melting under the blade [106, 72, 7]. In this paper, we take an idealized approach to the skating and consider an ideal blade that glides in a frictionless fashion on ice, with the gliding motion happening only along the blade's direction. Such assumptions lead to mechanical models lying in the realm of *nonholonomic mechanics* [11], utilizing mechanical models of the skater with affine (in our case, linear) constraints on velocities.

Several models of skaters have been developed in the context of nonholonomic mechanics. A large portion of the literature has been dedicated to the development of a dynamic model of a skater without control. This direction of work started with the classic development by Chaplygin [25], where a model of the *Chaplygin's sleigh*, or skate, was suggested. Chaplygin's sleigh represents a flat solid body having a certain inertia and center of mass, which is capable of the two-dimensional motion of rotating and sliding on the horizontal ice. The direction of velocity of Chaplygin's sleigh at every point in time must be parallel to a direction specified by a blade attached to the body. In the classical non-controlled Chaplygin's sleigh, the blade's position and orientation with respect to the body is fixed. Notably, the problem of the classical Chaplygin's sleigh is integrable, representing one of the very few known examples of integrability in nonholonomic mechanics [64]. While this model is certainly interesting from the mathematical point of view [11, 8], it is much too simple for a realistic description of the skater's motion, which is controlled by the complex movement of the body. For a more realistic description, there have been many generalizations of the classical Chaplygin's sleigh problem in the literature. While we try to keep the literature review relatively compact here, of particular interest to us are the extensions including a movable mass positioned on the sleigh. For the extension of the sleigh's motion without active control, we note [129, 13] which considered a movable mass on a spring connected to a given point. As it turns out, that system happens to be integrable, although without the explicit expressions of the integrals of motion allowable by the classical Chaplygin's sleigh. Another extension that has received much interest in literature consists of a sleigh with a mass that is being forced to

move in a periodic fashion [10]. Such motion leads to Fermi-like acceleration of the sleigh with unbounded energy for certain initial conditions and values of parameters. This work has been further extended in [9] with incorporation of viscous friction in the sleigh's motion, and numerical analysis of the zones of parametric resonance. Finally [45] modeled a static three dimensional figure skater with a model that includes a lean with respect to the vertical direction, but no control or relative change of mechanical properties of the skater. It was shown that for the case when the projection of the center of mass onto the skate's direction coincides with the contact point, the system is integrable, whereas for other configurations the motion is chaotic. An interesting three dimensional extension of controlled motion of Chaplygin sleigh, not related to skating, was suggested in [37], in the context of the description of hydrodynamic motion.

The question of the controls the skater utilizes to obtain desired trajectories on ice is more complicated, especially regarding the mathematical principles behind tracing a desired trajectory on ice. Of course, the detailed mathematical model of the control leading to the actual compulsory figures is currently (and, most likely, will forever be) out of reach for analytical models that are the point of this article. In practice, the skater controls their center of mass by moving the positions of arms, legs, and torso, resulting in trajectory changes. The control is produced in the body frame, while the resulting traces are in the coordinate frame fixed in space (spatial frame). The mechanisms figure skaters use to map the body frame to the spatial frame are very complex, not very well understood, and take years of practice for skaters to learn precise and accurate control. This lack of current theoretical understanding is even shown in the methods used to teach figure skating. For example, there are many different techniques for each figure skating element, with different body positions considered "optimal" in each technique. Often times, when learning a new element, the skater experiments with technique and tries to simply remember the physical feeling of a successful attempt in order to recreate the success of the trajectory on ice. The level to which a skater analyzes their movements and the resulting impact on the physical properties obviously varies skater to skater, but it is not a common practice to significantly examine

this relationship.

In this work, we focus on the controls involved in the field of compulsory figures, based on the simple example of the Chaplygin's sleigh with a moving mass. The mass is moved in such a way that the trajectory of the blade on ice is as close as possible to the desired trajectory. It seems to us that if we consider this system as a model of a human skater, one should consider the position of the center of moving mass as the controls, as opposed to the forces exerted on the mass being the controls. Indeed, in everyday life, we can move our hands and legs to the desired position relative to the torso, whereas the forces needed for this position to be obtained are calculated implicitly by the brain to achieve the desired position.

Compared to the extensive literature dedicated to the dynamics of the sleigh, there have been substantially less work in the literature on the control. In applications relevant to skating, we point out the control of the motion of Chaplygin's sleigh using impulsed force [120], modeling the push off ice. There is also the work on the control of a two-link Chaplygin sleigh similar to the control of two trajectories by changing the relative angle between the skates [34], and the work on the trajectories of the Chaplygin's sleigh forced by the periodic motion of the internal rotor [35]. The trajectory tracking using periodic application of a controlled torque for a dissipative was further developed in [36]. Interestingly, in that paper, one of the trajectories followed approximately (on average) by the controlled sleigh was a circle. We will show in this paper that the circular arcs are unique trajectories and one can design a control mechanism for following a circle exactly. The actual motion of the skater using trajectory tracing is done gliding on just one skate, with very few additional pushes allowed during the process. This is achieved by changing the position of center of mass and moments of inertia using carefully executed motion of the body. Thus, the most relevant previous work for our control procedure on trajectory tracing is [85], where Chaplygin's sleigh was steered based on the prescribed motion of a movable mass. In our work, we show how to develop an optimal control procedure that is capable of tracing a large variety of curves on the ice, possibly including cusps. A short one-page pedagogical review of this work has appeared in SIAM News [100].

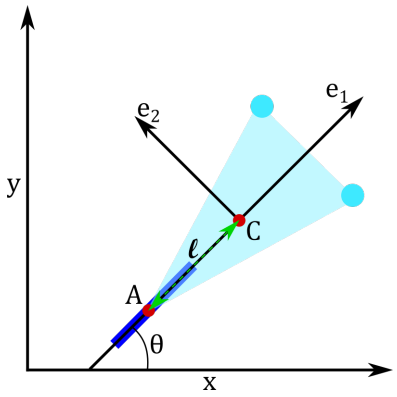

Figure 4.2: An illustration of the classical Chaplygin sleigh (top-down view). The triangular region represents the sleigh platform which is supported by two freely sliding, frictionless points which act to keep the blade upright. The solid blue line shows the blade forming the direction of the motion at each point. The point A indicates the contact point of the blade, where C is the position of the center of mass of the sleigh, and ℓ is the distance between A and C. The spatial coordinates are (x, y), while the body frame coordinates are given by (e_1, e_2).

In the following sections, we will present a mathematical description of the dynamics of a blade moving across the ice and describe how controls can be determined to produce a prescribed pattern. As an example, we present a control of the sleigh leading to tracing of a compulsory figure skating pattern illustrated in Figure 4.1.

4.2 Mathematical background: Chaplygin's sleigh

The classical Chaplygin sleigh, a model created and analyzed by Chaplygin in 1911 [26], describes a platform of mass M, with center of mass at position C, which has a knife edge with a single contact point (at A) and is supported by two frictionless points that slide freely. A schematic of this mechanical model is depicted in Figure 4.2. The frame attached to the sleigh (the body frame) is defined by the vectors $(\mathbf{e}_1, \mathbf{e}_2)$. The coordinates in the spatial frame are (x, y). The angle between the blade and the x-axis of the spatial frame is denoted by θ. The configuration manifold of the Chaplygin sleigh is thus the group of

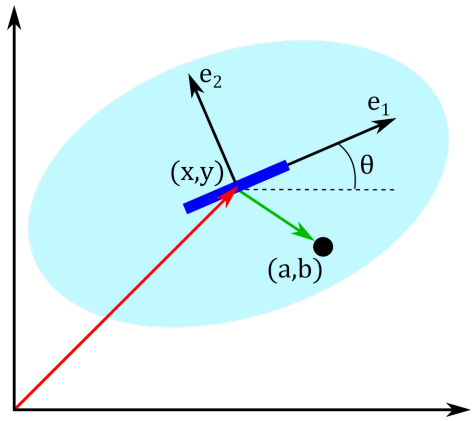

Figure 4.3: Chaplygin sleigh with added mass m positioned at the point (a, b) in the sleigh's coordinate system.

two dimensional rotations and translations $SE(2)$. In the local coordinates, that group can be described by the variables (x, y, θ). In Figure 4.2, we have chosen the coordinate system $\mathbf{e}_1$ to align with the blade in order for equations to conform with the previous literature on the subject. The Chaplygin sleigh includes a constraint that the direction of movement must be along the axis of the blade, that is, in the direction of $\mathbf{e}_1$ as seen from the spatial frame. Mathematically, this constraint is given by

$$-\dot{x}\sin\theta + \dot{y}\cos\theta = 0\,. \tag{4.1}$$

The constraint on the velocity cannot be written exclusively in terms of coordinates on the configuration manifold (x, y, θ), making the Chaplygin sleigh a nonholonomic system. The Chaplygin's sleigh has a mass M and moment of inertia with respect to the contact point I–we use that notation for the moment of inertia in order to conform to [85]. On the same figure, we present control mass m with a black dot, that has position $a\mathbf{e}_1 + b\mathbf{e}_2$ in the sleigh's coordinate system.

There have been many extensions to, and applications of, the Chaplygin sleigh of which we provide a few examples (see [16, 120, 34, 35, 65, 10, 56, 37, 13, 9]). We will employ the Chaplygin sleigh with added moving mass as the simplest model of a figure skater on the ice. The position and velocity of the

mass are the controls of the system. The specifications of the Chaplygin sleigh, along with the extension of applying an added mass, make the Chaplygin sleigh a good choice for modeling figure skating, and compulsory figures in particular. First, the controlled Chaplygin sleigh is applicable to figure skating because of the unique profile of the figure skate. Unlike hockey skate and speed skate blades, figure skate blades are curved from front to back. This curve along the length of the blade means that only a small portion of the blade contacts the ice at any given time, corresponding to the single contact point in the Chaplygin sleigh model. Of course, in the full 3D motion, the contact point will move back and forth along the blade. A good skater will minimize this contact point movement by controlling the position of the center of mass during the careful motion associated with the trajectory tracing exercise considered here. While interesting, this control of the position of the contact point is beyond the scope of this paper. In contrast, hockey and speed skate blades have large flat portions on the blade, and consequently more of the blade contacts the ice at all times. Second, the nonholonomic constraint on velocity is equivalent to the requirement of smooth gliding in compulsory figures, except for a finite set of predefined points where the skater is expected to turn. The velocity constraint clearly would not hold during other figure skating moves such as jumps where the skate leaves the ice. Finally, the mass added to the classical Chaplygin sleigh can be viewed as moving the skater's center of mass.

4.3 Control of a skater's trajectory using an added mass

4.3.1 General considerations

One of the most basic ways to control a skater's motion is to introduce an added mass m that can move in a prescribed manner with respect to the skater. In reality, a skater will use the complex motion of limbs that change both the position of the center of mass, the moment of inertia and, in addition, introduce additional forces and torques from the motion of the limbs. The controlled

motion of a single mass can be thought of as a single, two-dimensional version of a multi-limb control.

Control of nonholonomics systems using the motion of added masses has been considered before, see, for example, [96, 97] for applications to rolling ball robots. Several works address the dynamical evolution of the Chaplygin's sleigh with an added mass. In particular, we will point out a surprising result [13] that the problem of a sleigh with added mass m on a spring is integrable. The work [10] studied the motion of the Chaplygin sleigh with a prescribed, periodic motion of the added mass. The interesting part about this problem is the existence of trajectories with unlimited growth of energy, and thus unbounded acceleration, which was described as "an analog to Fermi acceleration". However, it is important to point out that not all trajectories lead to indefinite increase of energies, so the periodic motion of the added mass is not a guarantee of indefinite energy growth.

The problem of making predefined curves on ice, also known as trajectory tracking, using a movable mass has received much less attention in the literature. In [85] it was shown that it is possible to go from one straight line to another using a predefined motion of the moving mass. We are however not aware of works solving the trajectory tracing of complex trajectories as shown on Figure 4.1. This is precisely the point of this article. We shall present an algorithm that can be used to trace a large class of trajectories using suitable approximations of the curves.

4.3.2 Equations of motion

Let the angular momentum, measured relative to the contact point in the sleigh's frame, and the linear momentum, measured along the direction of the blade, also in the sleigh's frame, be denoted p_1 and p_2, respectively. The spatial coordinates of the blade contact point are given by (x, y), while θ is the angular orientation of the blade. The configuration space for this system is $SE(2)$. The position of the moving mass is (a, b) in the coordinate system of the sleigh. The Lagrangian of the system is simply the kinetic energy. It is easiest to derive the equations of motion using the framework suggested by

Hamel in 1904 [46], which is particularly useful for nonholonomic systems [14]. If the configuration manifold of the system is Q, with the local coordinates q^i, $i = 1, \dots n$, then the phase space in the Lagrangian approach consists of the coordinates q_i and velocities $\dot{q}^i$, $i = 1, \dots n$.

The idea of Hamel's method is to derive the equations of motion in the coordinates q^i and *quasivelocities* v^i, which are connected to the velocities $\dot{q}$ by the linear transformation u, *i.e.* $\dot{q}^i = u^i_j v^j$. Changing the Lagrangian to the coordinates (q, v), and using an appropriately modified variational principle, an alternative to Lagrangian mechanics can be derived. The resulting equations are called Hamel's mechanics. They reduce to familial Euler-Lagrange equations of mechanics if $\dot{q}^i = v^i$. In the case of nonholonomic systems with m constraints, the last m of quasivelocities $v^{n-m+1}, v^{n-m+2} \dots, v^n$, can be chosen in such a way that they coincide exactly with the nonholonomic constraints. Thus, only the first $n - m$ of Hamel's equations should be considered, whereas the last m equations vanish identically. Because of this reason, Hamel's method is advantageous to the standard Lagrange-d'Alembert's method for nonholonomic systems, as it does not involve Lagrange multipliers and all equations for nonholonomic systems are computed explicitly.

In terms of the controlled Chaplygin's sleigh, the nonholonomic constraint (4.1) advises the following choice of quasivelocities:

$$v^1 = \dot{\theta}, \quad v^2 = \dot{x}\cos\theta + \dot{y}\sin\theta\,, \quad v^3 = -\dot{x}\sin\theta + \dot{y}\cos\theta\,, \tag{4.2}$$

where dot notation indicates a time derivative. Note that the last equation of (4.2) coincides with the nonholonomic constraint (4.1). With the Lagrangian being just the kinetic energy, Hamel's equations for the uncontrolled sleigh with a moving mass were derived in [12, 11], and for sleigh with controlled

and moving mass in [85, 14]. These equations are written as

$$\dot{p_1} = - m\eta\xi^2 \,, \tag{4.3}$$

$$\dot{p_2} = m\eta\xi^1 \,, \tag{4.4}$$

$$\dot{\theta} = \xi^1 \,, \tag{4.5}$$

$$\dot{x} = \xi^2 \cos\theta \,, \tag{4.6}$$

$$\dot{y} = \xi^2 \sin\theta \,, \tag{4.7}$$

where

$$\xi^1 = \frac{1}{\gamma}\left((M+m)(p_1 - ma\dot{b}) + mb(p_2 + M\dot{a})\right) \,, \tag{4.8}$$

$$\xi^2 = \frac{1}{\gamma}\left(m[b(p_1 - ma\dot{b}) - (I + ma^2)\dot{a}] + [I + m(a^2+b^2)]p_2\right) \,, \tag{4.9}$$

$$\eta = \frac{1}{\gamma}\left([Mmb^2 + I(M+m)]\dot{b} + a[(M+m)p_1 + mb(p_2 + M\dot{a})]\right) \,, \tag{4.10}$$

$$\gamma = (M+m)(I+ma^2) + Mmb^2 \,. \tag{4.11}$$

For further details of the derivation of the above system, we refer the reader to [85]. Here, $p_{1,2}$ have the physical meaning of (nonholonomic) angular and linear momenta, respectively; ξ^1 and ξ^2 are the angular and linear velocities of the sleigh, θ is the angle of the blade with respect to a fixed coordinate frame. Note that the dynamic equations seemingly do not involve the accelerations of control masses, as they are formulated in terms of time derivatives of the momenta. The control variables are the position $(a(t), b(t))$ and the velocities $(\dot{a}, \dot{b})$ of the added mass m. Our goal will be to compute the motion of control masses which we will accomplish below by approximation of trajectories by circular arcs.

Suppose a trajectory on ice is given. We shall define the trajectory as a piecewise smooth curve $(X(s), Y(s))$ where s is the arc length. The curve tracing problem we are interested in does not care about the speed with which the curve is traced. We thus formulate the following general problem.

Problem 1 (General statement of control procedure)**.** *Suppose a given piecewise plane curve $x = X(s), y = Y(s)$ forms a graph G on (x, y) plane. Find*

the initial conditions and controls $(a, b, \dot{a}, \dot{b})$ *such that the graph* G_s *of the solution curve given by (4.3-4.7) minimizes the deviation from the curve in some norm.*

While Problem 1 is the closest to actual task of a figure skater performing trajectory tracing on ice, the problem as formulated above is too difficult to implement. That difficulty arises as the mapping from initial conditions and controls to the ice trajectories is highly nontrivial. Instead of solving Problem 1 directly, we separate the control procedure in two parts. First, we approximate any piecewise smooth curve using circular arcs. Second, we develop a control procedure for following the circular arcs on ice.

Circular arcs play a special role in the dynamics of the uncontrolled sleigh since they represent some of the exact solutions of the dynamics. Surprisingly, circular trajectories also play a special role in the controlled problem. More precisely, circles yield *algebraic* equations for control variables, which greatly simplifies designing the control procedure. This can be seen as follows.

Lemma 2 (On tracing of circular trajectories)**.** *A controlled solution trajectory is a circular arc of radius* r *if and only if the controls satisfy*

$$\xi^2 = r\xi^1\,, \tag{4.12}$$

where ξ^1 *and* ξ^2 *are given by* (4.8) *and* (4.9)*, respectively. In the particular case of straight lines, the controls satisfy* $\xi^1 = 0$*. Moreover, there is an additional constant of motion* P *defined as*

$$\begin{aligned} \text{arcs:} \quad & rp_2 + p_1 = P = \text{const}, \\ \text{straight lines } (r=\infty)\text{:} \quad & p_2 = \text{const}\,, \quad \xi^1 = 0. \end{aligned} \tag{4.13}$$

Proof. From (4.6) and (4.7) we obtain $\mathrm{d}s = \xi^2 \mathrm{d}t$. Additionally, from (4.5), we obtain

$$\frac{\mathrm{d}\theta}{\mathrm{d}s} = \frac{\xi^1}{\xi^2}\,. \tag{4.14}$$

A curve is a circle of radius r if and only if $\theta'(s) = 1/r$, giving exactly (4.12). In the particular case of a straight line, the limiting procedure gives $\xi^1 = 0$.

When (4.12) is valid, p_1 and p_2 are coupled as well from (4.3) and (4.4), allowing us to notice that

$$\dot{p_1} = -m\eta\xi^2 = -m\eta(r\xi^1) \quad \Longrightarrow \dot{p_1} = -r\dot{p_2} \tag{4.15}$$

and (4.13) follows.

Note that the condition for the sleigh to follow a straight line with constant velocity

$$(M+m)p_1 + mbp_2 = 0\,. \tag{4.16}$$

found in [85] follows exactly from $\xi^1 = 0$ with $\dot{a} = 0$ and $\dot{b} = 0$.

As the next step in the control procedure, we note the result by Meek and Walton [77] which presented an algorithm for finding arbitrarily close arc spline approximation of a smooth curve:

Lemma 3 (On approximating smooth curves by circular arcs)**.** *If the bounding circular arcs enclose a given spiral segment of positive curvature $Q(s)$, $s_0 \leq s \leq s_1$, and a biarc that matches the same data as the bounding circular arcs is found, then the maximum distance between the biarc and the spiral is $\mathcal{O}(h^3)$, where $h = s_1 - s_0$.*

Thus, we approximate any smooth part of the trajectory by circular arcs as in [77], and use the result of Lemma 2 to design the control procedure, outlined below. To complete the control of the trajectory in a realistic case, as illustrated on Figure 4.1, we notice that the cusps make the trajectories non-smooth. The cusps are executed by an experienced ice skater by performing a quick turn exactly at the moment when the speed of the skate with respect to the ice vanishes. At the point of the turn, the blade digs into the ice and the nonholonomic constraint no longer holds. It is only at these points the finite turn is possible. We shall note that there are also cusps which can be executed without the finite turn, when two arcs touch tangentially [45], but we do not focus on such cases here. Thus, we allow that at the points when the velocity vanishes, a finite turn can be executed, and a new arc can be started with zero velocity. The control algorithm is thus described as follows.

1. Separate the desired trajectory into smooth parts.

2. Approximate every smooth part by circular arcs.

3. Find a trajectory with control satisfying (4.12) following *exactly* the chosen circular arc. At all the cusp points, the velocity of the skate with respect to the ice must be zero.

4. Join circular arcs by allowing a finite turn at the cusp point.

Notice that the advantage of this procedure is that the difficulty of finding the controls for an arbitrary trajectory is now substituted by approximating the curve with circular arcs as in [77]. Once the approximation is found, we only need to find the controls enforcing vanishing velocity at the end points, as with the right initial conditions the solution is *guaranteed* to follow the arc. Moreover, there is an additional bonus of simplified solution due to (4.13) when using circular arcs or straight lines.

4.3.3 Chaplgyin sleigh model reduced to circular trajectories

Under the conditions that trajectories are circular arcs, the Chaplygin sleigh figure skate model is

$$\begin{aligned} \dot{p_1}(t) =& - m\eta\xi^2 \,, \\ \dot{\theta}(t) =& \xi^1 \,, \\ \dot{x}(t) =& \xi^2 \cos\theta \,, \\ \dot{y}(t) =& \xi^2 \sin\theta \,. \end{aligned} \tag{4.17}$$

with initial conditions

$$p_1(0) = \bar{p}_1 \,, \tag{4.18}$$

$$\theta(0) = \bar{\theta} \,, \tag{4.19}$$

$$x(0) = \bar{x} \,, \tag{4.20}$$

$$y(0) = \bar{y} \,, \tag{4.21}$$

with constraints (4.12) and p_2 given from the integral of motion

$$p_2 = \frac{P - p_1}{r} \,. \tag{4.22}$$

We are now ready to compute the equation for control masses. The condition $\xi^2 = r\xi^1$ gives an affine equation connecting $\dot{a}$ and $\dot{b}$:

$$\begin{aligned} & A\dot{a} + B\dot{b} = C \,, \quad \text{where} \\ & A := mMrb + m(I + ma^2) \,, \\ & B := m^2ab - (M+m)mar \,, \\ & C := p_1\left[mb - r(M+m)\right] + p_2\left[I + m(a^2+b^2) - mbr\right] \,. \end{aligned} \tag{4.23}$$

A user can choose an arbitrary second condition for $a(t)$ and/or $b(t)$ to specify the control functions. The simplest case is to specify, for example, $a(t)$ and compute $b(t)$ from (4.23), or vice versa. Unfortunately, this selection often lead to singularities. For example, if $a(t)$ is specified, then $\dot{b}(t)$ diverges whenever $a(t) = 0$, which is unphysical. That is, no practical controller can provide infinite energy to the control masses. However, there is a way to specify the equations for $(\dot{a}, \dot{b})$ without having any singularities. Namely, we choose $(\dot{a} = v_a, \dot{b} = v_b)$ according to the minimum energy of the controller:

$$(v_a, v_b) = \arg\min \frac{1}{2}(v_a^2 + v_b^2) \;\text{ s.t. } Av_a + Bv_b = C \tag{4.24}$$

with the solution

$$\dot{a} = v_a = \frac{AC}{A^2 + B^2} \,, \quad \dot{b} = v_b = \frac{BC}{A^2 + B^2} \,. \tag{4.25}$$

Note that technically speaking, the quantity $\frac{1}{2}(v_a^2 + v_b^2)$ minimized by (4.24)-(4.25) is not the actual kinetic energy of the control mass, since the kinetic energy must include the absolute velocities of the mass, not the relative veloc-

ities. One could in principle make the control procedure minimizing the true kinetic energy of the control mass, which is given by the formula (4.29) below. Since the kinetic energy of the control mass would still be a quadratic function of v_a and v_b, this problem would also lead to solutions similar to (4.25), although algebraically quite a bit more complex. We will use the formulation (4.24)-(4.25) in this paper since this formulation is algebraically simple, yields well-behaved equations for optimization, and can be used robustly in simulations. We will also refer to the quantity $\frac{1}{2}(v_a^2 + v_b^2)$ somewhat loosely as the *relative* kinetic energy, hoping that there will be no confusion with the actual value of the kinetic energy of the controller. As described in Section 4.3.1, zero speed is required at cusp points. The speed with respect to the ice $v(t)$ is given by

$$v(t) = \sqrt{(\dot{x})^2 + (\dot{y})^2} = \xi^2 \,. \tag{4.26}$$

Therefore, the requirement that the speed be zero at cusp points is equivalent to $\xi^2 = 0$ at such points.

4.3.4 Target curve parsing

As a first step in reproducing a given curve, we must define the target trajectory. This means parsing and dividing the trajectory into components of straight lines and circular arcs. In this work, this was accomplished manually with the target curves being divided into approximate curves (eg. semicircle, 3/4 circle, etc.). This process could surely be automated using techniques such as machine learning, but this is beyond of the scope of this work. We note that in the examples we present here, all the pieces of the curves are circular arcs. We thus address only the part of tracing the arcs, assuming that the pattern approximation by circular arcs has already been completed.

To reproduce a given curve component with the Chaplygin figure skate model, we use (4.25), minimizing the energy of the control mass. Given the radius of the arc, the length of the arc is matched using a root-finding procedure enforcing the arc lengths to be the same. Since two circular arcs of the same length and radius, starting at the same point and tangent to each other,

are going to be exactly identical, we achieve an exact tracing of trajectories down to desired precision.

We shall also note that when a trajectory is presented by several arcs joined smoothly, the parameters of the arcs such as radius may change abruptly between neighboring arcs. In that case, $(\dot{a}, \dot{b})$ may change discontinuously from arc to arc. It is possible that the trajectories of the control masses can be made smooth by introducing additional constraints on the variables (p_1, p_2, a, b) from arc to arc, dictated by (4.25). We have not explored such constraints in this paper, although it is interesting to consider them in future works on the subject.

4.4 Numerical methods

The simulations of the Chaplygin sleigh were carried out using the Python programming language, version 3.7.6 (Python Software Foundation, https://www.python.org/). For defined sleigh dynamic parameters M, m, I, and a given radius of the arc r, we find the trajectory following that arc as follows:

1. The system is defined according to (4.17) with the added equation for the length $\dot{L} = \xi^2$ for convenience of computations. The control functions $(\dot{a}, \dot{b})$ are defined according to (4.25). We have also chosen to bring back the equation $\dot{p}_2 = m\eta\xi^2$, to use the integral $p_1 + rp_2$, which should be a constant, as an additional measure of accuracy of calculations and the accuracy of the circle constraint (4.12). The initial conditions for the simulations are

$$\begin{aligned} &p_1(0) = p_1^0,\ p_2(0) = p_2^0,\ \theta(0) = 0, \\ &x(0) = 0,\ L(0) = 0,\ a(0) = a^0,\ b(0) = b^0 \end{aligned} \tag{4.27}$$

2. Find zero-crossing events for $\xi^2 = 0$ in simulations, $t_0, t_1, \ldots$

3. As it turns out, the solution quickly converges to a periodic motion for the essential variables p_1, a, b.

4. (Single-length matching) For the single curve matching (parts of the "leaves" for the inner pattern in the next section), we need only match one circle to the given length L_*. This is accomplished by specifying (p_2^0, a^0, b^0) and finding p_0 such that $L(t_{i+1}) - L(t_i) = L_*$ for some i.

5. (Multi-length matching) Similarly, we can also find a pattern made by several arcs (the outer three-arc part of the pattern in the next Section). We find three neighboring events (t_i, t_{i+1}, t_{i+2}) and two desired lengths L_*^1 and L_*^2 such that $L(t_{i+1}) - L(t_i) = L_*^1$, $L(t_{i+2}) - L(t_{i+1}) = L_*^2$ for some i.

6. The inner and outer solutions are then concatenated to give the full inner and outer pattern.

4.5 Simulations

As a proof of concept, we reproduce the compulsory figure shown in Figure 4.1. In order to recreate this pattern, the base components must be identified. In this case, there are two separate curves, each with repeating patterns.

Between the inner and outer patterns, the inner pattern is simpler, consisting of a single continuous arc with one direction of travel. To match the compulsory figure, this arc is taken to be slightly more than a semi-circle, which is then repeated eight times. The outermost curve can be decomposed into two different arcs: a short arc, and a longer arc that is slightly less than a semi-circle. The full outer curve can then be represented by sequentially connected triplets consisting of a long arc, followed by a short arc, completed by another long arc, and then repeating this triplet, or "leaf", eight times. The total outer pattern includes changes in the direction of travel at the cusp points where the component arcs meet. The simulation parameters for each arc are given in Table 4.1. The simulated inner and outer arcs, as well as the control functions and ξ^2 profiles, are shown in Figures 4.4 and 4.5, respectively.

As the inner arc component will be joined by finite arcs with an execution of a finite turn, there is a physical requirement that the speed, ξ^2, be zero at either end of the arc. The top right panel shows that the speed is indeed zero

Table 4.1: Values used in simulations to create inner and outer arcs. In all cases $m = 1$, $M = 2$, and $I = 3$.

Arc	Radius	Length(s), L^i_*	(p^0_1, p^0_2, a^0, b^0)
Inner	1	3.7	$(50, 60, 1.5, -0.1)$
Outer	1	$3, 0.4$	$(100, 30, 0.8, -0.1)$

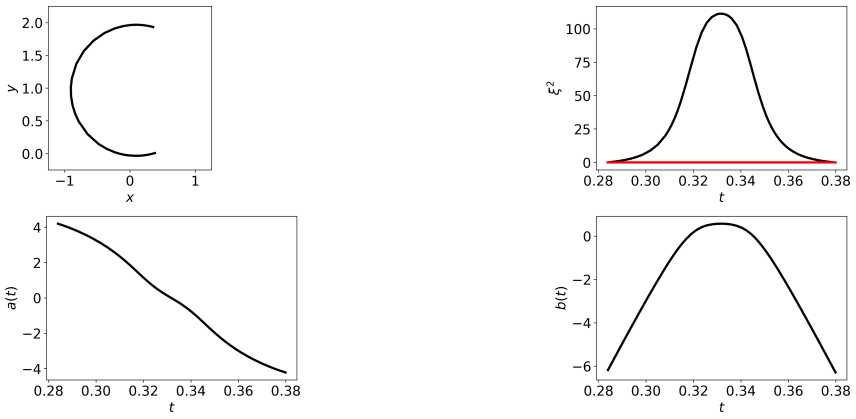

Figure 4.4: Inner pattern trajectory (*top left*), ξ^2 profile (*top right*), and optimized control functions, $a(t)$ (*bottom left*) and $b(t)$ (*bottom right*).

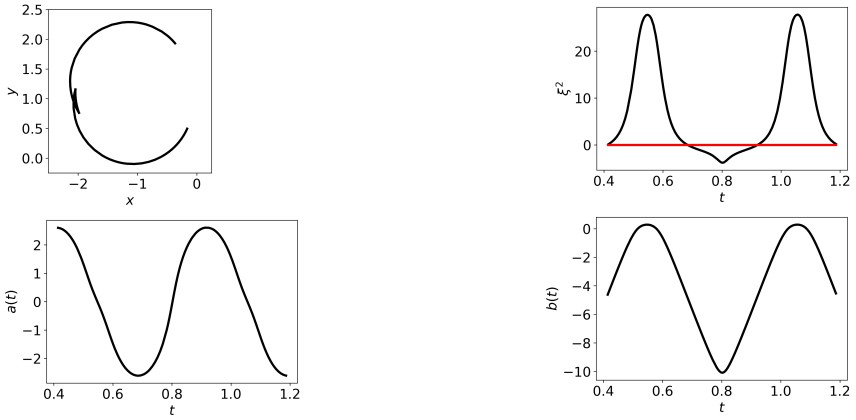

Figure 4.5: Outer pattern trajectory (*top left*), ξ^2 profile (*top right*), and optimized control functions, $a(t)$ (*bottom left*) and $b(t)$ (*bottom right*).

at either end of the arc. The optimized control functions, $a(t)$ and $b(t)$, are shown in the bottom two panels.

As noted previously, each leaf of outer pattern includes cusps. At the two cusp points where the long and short arcs meet, the speed, ξ^2, is zero, with the direction of travel changing at each cusp point. All three arcs in each leaf of the outer pattern are produced from one continuous simulation of the system, augmented by the finite turn at two points connecting smaller and larger arcs. Thus, each leaf of the outer pattern was obtained by a smooth motion of the control mass. The plot of ξ^2 in the top right panel of Figure 4.5 shows that the outer arc satisfies the requirement that ξ^2 be zero at each cusp and that the sign of velocity changes at each cusp. As with the inner arc, the outer arc also satisfies the physical requirement that ξ^2 is zero at either end of the arc as the endpoints are connected in the full outer pattern.

Because the blade digs into the ice at the point of the turn, the approximation of the nonholonomic constraint for the skate no longer holds, as the blade remains momentarily pinned to the surface. This fact allows for sudden shifts in a skater's center of mass which are compensated by the reaction force from the ice.

In order to better understand the optimized control functions, Figure 4.6 shows the trajectory of the position of the added mass m (in body frame) next to the blade trajectory (in spatial frame) for each arc, as well as the skate and mass trajectories together in the spatial frame.

It is also useful to compute the energy of the system and confirm that the total energy remains bounded. Thus, we derive the total energy for both the skate and control mass, and compute the total energy for each arc. The total energy of the skate is given by

$$KE_{\text{skate}} = \frac{1}{2}M(\xi^1)^2 + \frac{1}{2}I(\xi^2)^2\,, \tag{4.28}$$

The total energy of the control mass can be computed in a straightforward way to give:

$$KE_m = \frac{1}{2}m|\mathbf{v}|^2 = \frac{m}{2}\left[\left(\xi^2 - \xi^1 b + \dot{a}\right)^2 + \left(\xi^1 a + \dot{b}\right)^2\right] \tag{4.29}$$

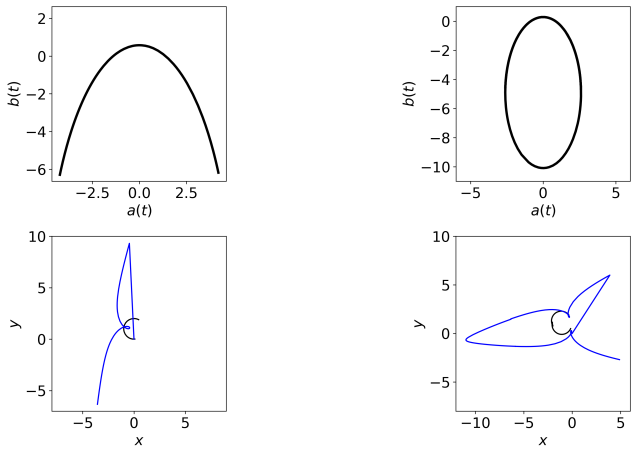

Figure 4.6: Control mass trajectories (*top*) and overlay of skate (black) and control mass (blue) trajectories in spatial frame (*bottom*) for the inner trajectories (*left*) and outer trajectories (*right*).

with $(\dot{a}, \dot{b})$ given by (4.25). As shown in Figure 4.7, the energy profiles for the optimized control mass and skate for each arc remain bounded (but non-monotonic in time) as desired. To show the accuracy and correctness of the simulations, in Figure 4.8 we present a plot of $rp_2 + p_1$ which should be an integral of motion for the circular trajectories. Indeed, this integral is conserved to within high accuracy for both inner and outer solutions.

Finally, the full pattern is produced by transforming (via rotation and translation) and repeating the optimized arcs is shown in Figure 4.9. Notice the clear resemblance of the pattern reproduced by our method to the target "double flower" pattern of Figure 4.1. In principle, we could reproduce a large class of piecewise smooth curves, where the smooth parts of the curves are approximated by circular arcs. The limitation on control is then at the points of sharp turns, where the velocity of the skate needs to vanish. Thus, a control to successfully trace trajectories is possible whenever it is possible to create the motion using the control mass while enforcing vanishing velocity at two ends for every smooth part of the curve. We believe that this control mechanism spans a large number of possible trajectories and is substantially simpler than the "brute force" trajectory tracing without specifying particular constraints on the motion of the control masses.

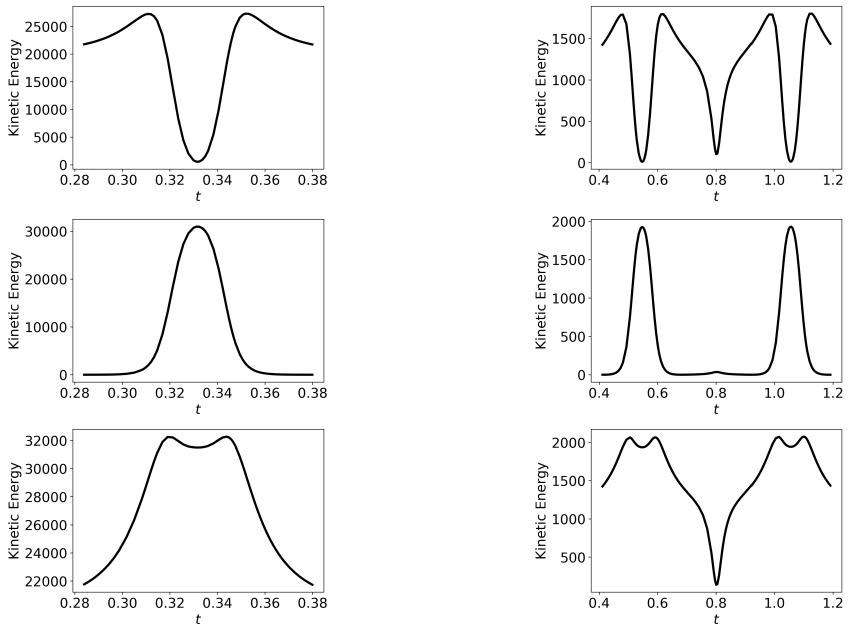

Figure 4.7: Kinetic energy of control mass (*top*), skate (*middle*), and total kinetic energy (*bottom*) for inner pattern arc (*left*) and outer pattern arc (*right*).

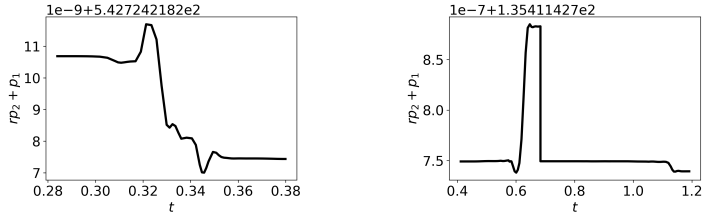

Figure 4.8: Plots of $rp_2 + p_1$ showing that the integral of motion (4.22) following from the circle constraint condition $\xi^2 = r\xi^1$ is satisfied for inner (*left*) and outer (*right*) arcs.

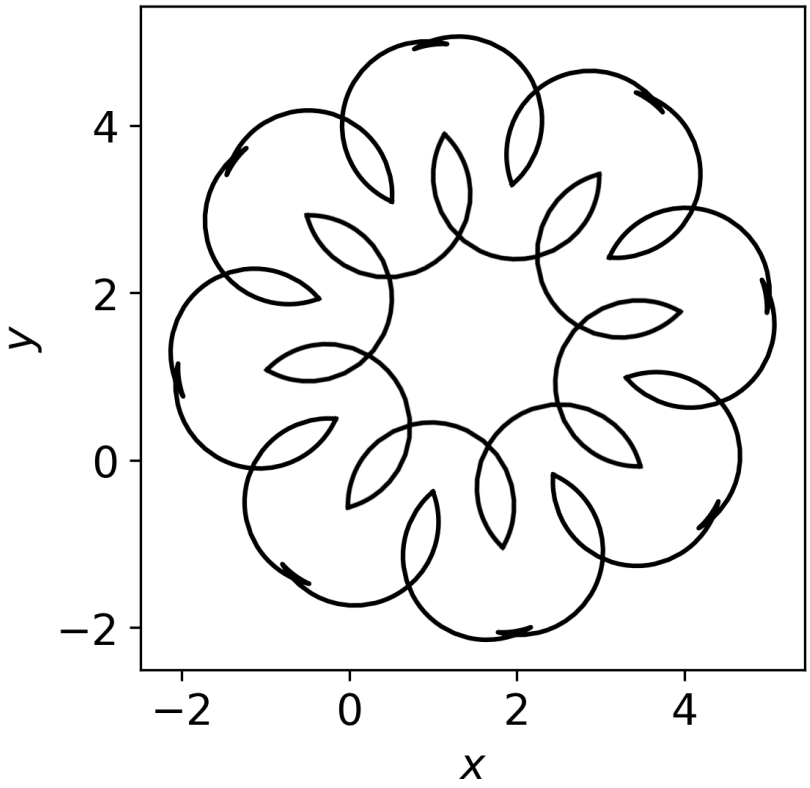

Figure 4.9: Full pattern reconstruction using the control procedure. Compare to the target Figure 4.1.

4.6 Conclusion

We have applied the control of the moving mass on a Chaplygin sleigh to model the dynamics of a figure skater tracing a prescribed pattern on the ice. With the added mass representing the controllable center of mass of the figure skater, we determined the controls needed to reproduce an example pattern, which is approximated by circular arcs. The approximation of circular arcs was chosen for the simplicity of algorithms, as in that case the equations for the control simplify considerably: the question of trajectory tracing, which is very complex, simplifies to the matching the beginning and the end of the arc, with the curvature being matched automatically. It would also be interesting to see whether the ideas developed in this paper apply to the dissipative sleigh as considered in [36] .

For a more complex trajectory tracing, a machine learning algorithm could be used. For example, deep reinforcement learning algorithms have been used with success for drone control in 3D [62]. A more realistic model of a human skater compared to Chaplygin sleigh will involve substantially more degrees of freedom than a drone, in addition to the constraints on the skate's motion. The expansion of techniques of constrained reinforcement learning [39] can prove useful here. We hope that the researchers in the field of reinforcement learning will become interested in tackling this challenging problem.

Declarations

Funding. M.R. acknowledges the Pacific Institute for the Mathematical Sciences (PIMS) MathBio Accelerator Award for partial support during this project.

Conflicts of interest/competing interests. The authors declare that they have no conflict of interest.

Availability of data and material. Not applicable.

Code availability. Code can be made available upon request.

Authors' contributions. M.R. and V.P. carried out the calculations, developed the control procedure, and implemented it in the code. M.R. produced the figures. M.R. and V.P. wrote the manuscript. M.R. and V.P. read and approved the final manuscript.

Acknowledgements

M.R. acknowledges the Pacific Institute for the Mathematical Sciences (PIMS) MathBio Accelerator Award for partial support during this project. The authors are grateful for the infinite patience of, and many discussions with, Prof. D. V. Zenkov. We are grateful to Profs. A. Bloch and D. D. Holm for their constant interest and thoughtful insights in the mechanics and control of nonholonomic systems. We are indebted to V. Gzenda for many discussions related to the mechanics of figure skating robots. We are grateful to Dr. V. Fedonyuk for pointing out some recent references in the control and dynamics of Chaplygin's sleigh. We are appreciative of the work by SIAM News staff, and in particular Lina Sorg, for their interest in showcasing this work in [100].

Chapter 5

Conclusion

The topics of glioma spread and tracing patterns in figure skating are quite distinct from one another. The through line connecting them is mechanics. Although there are many factors involved in glioma, from cellular genetics, to the immune response and beyond, mechanics is becoming increasingly recognized as a component that cannot be ignored. We hope that we have taken a further step in the ever progressing field of mathematical models of glioma.

We began the work in this thesis by analyzing and simulating a simplified 1D glioma model. We showed the existence and determined the invasion speed of travelling waves in the 1D glioma spread model for multiple versions of elasticity models. We found that travelling wave existence and speeds are maintained between elasticity models, with minimal wave speed being given by $\sigma = 2\sqrt{D\rho}$. Although the wave speed is consistent across elasticity models, the deformation and stress can differ significantly from model to model. Interestingly, the addition of viscosity did not prove to lead to any substantial differences in model dynamics. The deformation and stress results may be an important consideration when it comes to symptoms as they are largely caused by increased deformation and stress caused by the growing glioma.

Increasing the complexity of the glioma model from Chapter 2, we successfully developed and implemented a 2D glioma model with linear elasticity using finite element methods. We also developed a numeral pipeline for importing medical imaging data for the initialization of the simulation domain and diffusion tensors, allowing for the incorporation of patient specific data.

Furthermore, in the translation of DTI data to the model diffusion tensor, we utilize a previously developed method which allows for additional fitting of the anisotropy and turning rate parameters to patient data. We also show that there is another parameter that could be fit to patient data–the body force parameter. Although fitting this parameter was beyond the scope of this work, this is a critical parameter in the pattern of glioma spread and would be worth while investigating further. As mentioned, there are many avenues to continue with the 2D model and we hope to explore at least some of these in ongoing work.

The dependence of figure skating is perhaps more intuitively mechanical compared to glioma. In the last portion of this thesis, we explored a mechanical model of a figure skater using the Chaplygin sleigh with an added mass. There have been previous works examining the mechanics of some of the more "exciting" elements such as jumping and the extreme forces involved, but few, if any, have studied the controls associated with gliding on ice. Employing previous results for the approximation of curves and some simplifications of movement, we developed a control algorithm capable of reproducing any target curve. By developing a control algorithm that can be used to reproduce any curve, we hope that we have shed some light on the physical basis behind the sport of figure skating.

Bibliography

[1] Daniel Abler and Philippe Büchler. Evaluation of a mechanically coupled reaction–diffusion model for macroscopic brain tumor growth. In Amit Gefen and Daphne Weihs, editors, *Computer Methods in Biomechanics and Biomedical Engineering*, pages 57–64, Cham, 2018. Springer International Publishing.

[2] Sandra Ackerman et al. Discovering the brain. 1992.

[3] Andrew L Alexander, Jee Eun Lee, Mariana Lazar, and Aaron S Field. Diffusion tensor imaging of the brain. *Neurotherapeutics*, 4(3):316–329, 2007.

[4] D Ambrosi and F Mollica. On the mechanics of a growing tumor. *International Journal of Engineering Science*, 40:1297–1316, 2002.

[5] Stelios Angeli, Kyrre E Emblem, Paulina Due-Tonnessen, and Triantafyllos Stylianopoulos. Towards patient-specific modeling of brain tumor growth and formation of secondary nodes guided by DTI-MRI. *NeuroImage: Clinical*, 20:664–673, 2018.

[6] Stelios Angeli and Triantafyllos Stylianopoulos. Biphasic modeling of brain tumor biomechanics and response to radiation treatment. *Journal of Biomechanics*, 49(9):1524–1531, 2016.

[7] M. Le Berre and Y. Pomeau. Theory of ice-skating. *International Journal of Non-Linear Mechanics*, 75:77–86, 2015.

[8] I. A. Bizyaev, A. V. Borisov, V. V. Kozlov, and I. S. Mamaev. Fermi-like acceleration and power-law energy growth in nonholonomic systems. *Nonlinearity (under consideration)*, 2018.

[9] I.A. Bizyaev, A.V. Borisov, and S.P. Kuznetsov. The Chaplygin sleigh with friction moving due to periodic oscillations of an internal mass. *Nonlinear Dynamics*, 95(1):699–714, 2019.

[10] I.A. Bizyaev, A.V. Borisov, and I.S. Mamaev. The Chaplygin sleigh with parametric excitation: chaotic dynamics and nonholonomic acceleration. *Regular and Chaotic Dynamics*, 22(8):955–975, 2017.

[11] A. M Bloch. *Nonholonomic mechanics and control*, volume 24. Springer Science & Business Media, 2003.

[12] A. M. Bloch, P. S. Krishnaprasad, J. E. Marsden, and R. M. Murray. Nonholonomic mechanical systems with symmetry. *Archive for Rational Mechanics and Analysis*, 136:21–99, 1996.

[13] A. M. Bloch, J.E. Marsden, and D.V. Zenkov. Quasivelocities and symmetries in nonholonomic systems. *Dynamical Systems*, 24:187–222, 2009.

[14] Anthony M Bloch, Jerrold E Marsden, and Dmitry V Zenkov. Quasivelocities and symmetries in non-holonomic systems. *Dynamical Systems*, 24(2):187–222, 2009.

[15] Pierre-Yves Bondiau, Olivier Clatz, Maxime Sermesant, Pierre-Yves Marcy, Herve Delingette, Marc Frenay, and Nicholas Ayache. Biocomputing: numerical simulation of glioblastoma growth using diffusion tensor imaging. *Physics in Medicine & Biology*, 53(4):879, 2008.

[16] A.V. Borisov and S.P. Kuznetsov. Regular and chaotic motions of a Chaplygin sleigh under periodic pulsed torque impacts. *Regular and Chaotic Dynamics*, 21(7):792–803, 2016.

[17] D. Bresch, T. Colin, E. Grenier, B Ribba, and O. Saut. A viscoelastic model for avascular tumor growth. *Research Report*, pages inria–00267292v4, 2009.

[18] S Budday, Gerhard Sommer, C Birkl, C Langkammer, J Haybaeck, J Kohnert, M Bauer, F Paulsen, P Steinmann, E Kuhl, et al. Mechanical characterization of human brain tissue. *Acta Biomaterialia*, 48:319–340, 2017.

[19] Silvia Budday, Timothy C Ovaert, Gerhard A Holzapfel, Paul Steinmann, and Ellen Kuhl. Fifty shades of brain: a review on the mechanical testing and modeling of brain tissue. *Archives of Computational Methods in Engineering*, 27(4):1187–1230, 2020.

[20] Silvia Budday, Gerhard Sommer, Johannes Haybaeck, Paul Steinmann, Gerhard A Holzapfel, and Ellen Kuhl. Rheological characterization of human brain tissue. *Acta Biomaterialia*, 60:315–329, 2017.

[21] Silvia Budday, Gerhard Sommer, GA Holzapfel, Paul Steinmann, and Ellen Kuhl. Viscoelastic parameter identification of human brain tissue. *Journal of the Mechanical Behavior of Biomedical Materials*, 74:463–476, 2017.

[22] Patricia K Burgess, Paul M Kulesa, James D Murray, and Ellsworth C Alvord Jr. The interaction of growth rates and diffusion coefficients in a three-dimensional mathematical model of gliomas. *Journal of Neuropathology & Experimental Neurology*, 56(6):704–713, 1997.

[23] Neil G Burnet, Simon J Thomas, Kate E Burton, and Sarah J Jefferies. Defining the tumour and target volumes for radiotherapy. *Cancer Imaging*, 4(2):153, 2004.

[24] Helen Byrne and Luigi Preziosi. Modelling solid tumour growth using the theory of mixtures. *Mathematical Medicine and Biology*, 20:341–366, 2003.

[25] S.A. Chaplygin. On the theory of the motion of nonholonomic systems. theorem on the reducing factor. *Matematicheskii Sbornik*, 28(2):303–314, 1911.

[26] S.A. Chaplygin. On the theory of motion of nonholonomic systems. the reducing-multiplier theorem. *Regular and Chaotic Dynamics*, 13(4):369–376, 2008.

[27] Simon Chatelin, André Constantinesco, and Rémy Willinger. Fifty years of brain tissue mechanical testing: from in vitro to in vivo investigations. *Biorheology*, 47(5-6):255–276, 2010.

[28] Olivier Clatz, Maxime Sermesant, Pierre-yves Bondiau, Hervé Delingette, Simon K Warfield, Grégoire Malandain, and Nicholas Ayache. Realistic simulation of the 3-D growth of brain tumors in MR images coupling diffusion with biomechanical deformation. *IEEE Transactions on Medical Imaging*, 24(10):1334–1346, 2005.

[29] Gerhard C Cruywagen, Diana E Woodward, Philippe Tracqui, Grace T Bartoo, JD Murray, and Ellsworth C Alvord. The modelling of diffusive tumours. *Journal of Biological Systems*, 3(04):937–945, 1995.

[30] Gerda De Vries, Thomas Hillen, Mark Lewis, Johannes Müller, and Birgitt Schönfisch. *A course in mathematical biology: quantitative modeling with mathematical and computational methods*. SIAM, 2006.

[31] Leah Edelstein-Keshet. *Mathematical models in biology*. SIAM, 2005.

[32] C. Engwer, T. Hillen, M. Knappitsch, and C. Surulescu. Glioma follow white matter tracts: a multiscale DTI-based model. *Journal of Mathematical Biology*, 71(3):551–582, 2015.

[33] Alexandre Ern and Jean-Luc Guermond. Discontinuous Galerkin methods for Friedrichs' systems. I. General theory. *SIAM Journal on Numerical Analysis*, 44(2):753–778, 2006.

[34] V. Fedonyuk and P. Tallapragada. The dynamics of a two link Chaplygin sleigh driven by an internal momentum wheel. In *2017 American Control Conference (ACC)*, pages 2171–2175. IEEE, 2017.

[35] V. Fedonyuk and P. Tallapragada. Sinusoidal control and limit cycle analysis of the dissipative Chaplygin sleigh. *Nonlinear Dynamics*, 93(2):835–846, 2018.

[36] Vitaliy Fedonyuk and Phanindra Tallapragada. Path tracking for the dissipative Chaplygin sleigh. In *2020 American Control Conference (ACC)*, pages 5256–5261. IEEE, 2020.

[37] Y.N. Fedorov and L.C. García-Naranjo. The hydrodynamic Chaplygin sleigh. *Journal of Physics A: Mathematical and Theoretical*, 43(43):434013, 2010.

[38] Ronald Aylmer Fisher. The wave of advance of advantageous genes. *Annals of Eugenics*, 7(4):355–369, 1937.

[39] Peter Geibel and Fritz Wysotzki. Risk-sensitive reinforcement learning applied to control under constraints. *Journal of Artificial Intelligence Research*, 24:81–108, 2005.

[40] Philip Gerlee and Sven Nelander. The impact of phenotypic switching on glioblastoma growth and invasion. *PLoS Computational Biology*, 8(6), 2012.

[41] Philip Gerlee and Sven Nelander. Travelling wave analysis of a mathematical model of glioblastoma growth. *Mathematical Biosciences*, 276:75–81, 2016.

[42] Amir Gholami, Andreas Mang, and George Biros. An inverse problem formulation for parameter estimation of a reaction–diffusion model of low grade gliomas. *Journal of Mathematical Biology*, 72(1):409–433, 2016.

[43] A Giese, R Bjerkvig, ME Berens, and M Westphal. Cost of migration: invasion of malignant gliomas and implications for treatment. *Journal of Clinical Oncology*, 21(8):1624–1636, 2003.

[44] Ali Gooya, Kilian M Pohl, Michel Bilello, Luigi Cirillo, George Biros, Elias R Melhem, and Christos Davatzikos. GLISTR: glioma image segmentation and registration. *IEEE Transactions on Medical Imaging*, 31(10):1941–1954, 2012.

[45] V. Gzenda and V. Putkaradze. Integrability and chaos in figure skating. *Journal of Nonlinear Science*, pages 1–20, 2019.

[46] G. Hamel. Die Lagrange–Eulersche Gleichungen der Mechanik. *Z. Math. Phys.*, pages 1–57, 1904.

[47] S. Hamilton. Figure skating. *Encyclopædia Britannica*, May 2019. `https://www.britannica.com/sports/figure-skating`, Accessed: 2021-03-04.

[48] Farina Hanif, Kanza Muzaffar, Kahkashan Perveen, Saima M Malhi, and Shabana U Simjee. Glioblastoma multiforme: a review of its epidemiology and pathogenesis through clinical presentation and treatment. *Asian Pacific Journal of Cancer Prevention: APJCP*, 18(1):3, 2017.

[49] Tiberiu Harko and Man Kwong Mak. Travelling wave solutions of the reaction-diffusion mathematical model of glioblastoma growth: An Abel equation based approach. *arXiv preprint arXiv:1409.0605*, 2014.

[50] T. Härtel, F. Hildebrand, and K. Knoll. Methods of simulation and manipulation for the evaluation of figure skating jumps. In *The Engineering of Sport 6*, pages 179–184. Springer, 2006.

[51] F. Hecht. New development in FreeFem++. *Journal of Numerical Mathematics*, 20(3-4):251–265, 2012.

[52] T. Hillen. M^5 mesoscopic and macroscopic models for mesenchymal motion. *Journal of Mathematical Biology*, 53(4):585–616, 2006.

[53] Lucy V Hiscox, Curtis L Johnson, Eric Barnhill, Matt DJ McGarry, John Huston 3rd, Edwin JR Van Beek, John M Starr, and Neil Roberts. Magnetic resonance elastography (MRE) of the human brain: technique, findings and clinical applications. *Physics in Medicine & Biology*, 61(24):R401, 2016.

[54] Cosmina Hogea, Christos Davatzikos, and George Biros. An image-driven parameter estimation problem for a reaction-diffusion glioma growth model with mass effects. *Journal of Mathematical Biology*, 56:793–825, 2008.

[55] Saâd Jbabdi, Emmanuel Mandonnet, Hugues Duffau, Laurent Capelle, Kristin Rae Swanson, Mélanie Pélégrini-Issac, Rémy Guillevin, and Habib Benali. Simulation of anisotropic growth of low-grade gliomas using diffusion tensor imaging. *Magnetic Resonance in Medicine: An Official Journal of the International Society for Magnetic Resonance in Medicine*, 54(3):616–624, 2005.

[56] P. Jung, G. Marchegiani, and F. Marchesoni. Nonholonomic diffusion of a stochastic sled. *Physical Review E*, 93(1):012606, 2016.

[57] A Källen, P Arcuri, and JD Murray. A simple model for the spatial spread and control of rabies. *Journal of Theoretical Biology*, 116(3):377–393, 1985.

[58] D. King. Generation of vertical velocity in toe-pick figure skating jumps. In *ISBS-Conference Proceedings Archive*, 2001.

[59] D. King. Performing triple and quadruple figure skating jumps: implications for training. *Canadian Journal of Applied Physiology*, 30(6):743–753, 2005.

[60] Peter B Kingsley. Introduction to diffusion tensor imaging mathematics: Part II. anisotropy, diffusion-weighting factors, and gradient encoding schemes. *Concepts in Magnetic Resonance Part A*, 28(2):123–154, 2006.

[61] K. Knoll and T. Härtel. Biomechanical conditions for stabilizing quadruple figure skating jumps as a process of optimization. In *ISBS-Conference Proceedings Archive*, 2005.

[62] William Frederick Koch III. *Flight controller synthesis via deep reinforcement learning*. PhD thesis, Boston University, 2019.

[63] Ender Konukoglu, Olivier Clatz, Pierre-Yves Bondiau, Herve Delingette, and Nicholas Ayache. Extrapolating glioma invasion margin in brain magnetic resonance images: Suggesting new irradiation margins. *Medical Image Analysis*, 14(2):111–125, 2010.

[64] V. V. Kozlov. On the integration theory of the equations in nonholonomic mechanics. *Advances in Mechanics*, 8:86–107, 1985.

[65] S.P. Kuznetsov. Regular and chaotic dynamics of a Chaplygin sleigh due to periodic switch of the nonholonomic constraint. *Regular and Chaotic Dynamics*, 23(2):178–192, 2018.

[66] Stelios K Kyriacou and Christos Davatzikos. A biomechanical model of soft tissue deformation, with applications to non-rigid registration of brain images with tumor pathology. In *International Conference on Medical Image Computing and Computer-Assisted Intervention*, pages 531–538. Springer, 1998.

[67] Denis Le Bihan, Jean-François Mangin, Cyril Poupon, Chris A Clark, Sabina Pappata, Nicolas Molko, and Hughes Chabriat. Diffusion tensor imaging: concepts and applications. *Journal of Magnetic Resonance Imaging: An Official Journal of the International Society for Magnetic Resonance in Medicine*, 13(4):534–546, 2001.

[68] JM Lee, T Hillen, and MA Lewis. Continuous traveling waves for prey-taxis. *Bulletin of Mathematical Biology*, 70(3):654–676, 2008.

[69] AJBSJJDK Leemans, Ben Jeurissen, Jan Sijbers, and Derek K Jones. ExploreDTI: a graphical toolbox for processing, analyzing, and visualizing diffusion mr data. In *Proceedings of the International Society for Magnetic Resonance in Medicine*, volume 17, page 3537, 2009.

[70] Jean Lemaitre. Introduction to elasticity and viscoelasticity. In Jean Lemaitre, editor, *Handbook of Materials Behavior Models*, pages 71–74. Academic Press, Burlington, 2001.

[71] J. Lowengrub, E. Titi, and K. Zhao. Analysis of a mixture model of tumor growth. *European Journal of Applied Mathematics*, 24:691–734, 2003.

[72] E. Lozowski, K. Szilder, and S. Maw. A model of ice friction for a speed skate blade. *Sports Engineering*, 16:239–253, 2013.

[73] Paul Macklin and John Lowengrub. Nonlinear simulation of the effect of microenvironment on tumor growth. *Journal of Theoretical Biology*, 245:677–704, 2007.

[74] David B MacManus, Baptiste Pierrat, Jeremiah G Murphy, and Michael D Gilchrist. Region and species dependent mechanical properties of adolescent and young adult brain tissue. *Scientific Reports*, 7(1):1–12, 2017.

[75] Yogesh K Mariappan, Kevin J Glaser, and Richard L Ehman. Magnetic resonance elastography: a review. *Clinical Anatomy*, 23(5):497–511, 2010.

[76] Jerrold E Marsden and Thomas JR Hughes. *Mathematical foundations of elasticity*. Courier Corporation, 1994.

[77] D.S. Meek and D.J. Walton. Approximating smooth planar curves by arc splines. *Journal of Computational and Applied Mathematics*, 59(2):221–231, 1995.

[78] Alexander Mielke and Tomáš Roubíček. Thermoviscoelasticity in Kelvin–Voigt rheology at large strains. *Archive for Rational Mechanics and Analysis*, 238(1):1–45, 2020.

[79] L Angela Mihai, Silvia Budday, Gerhard A Holzapfel, Ellen Kuhl, and Alain Goriely. A family of hyperelastic models for human brain tissue. *Journal of the Mechanics and Physics of Solids*, 106:60–79, 2017.

[80] L Angela Mihai, LiKang Chin, Paul A Janmey, and Alain Goriely. A comparison of hyperelastic constitutive models applicable to brain and fat tissues. *Journal of The Royal Society Interface*, 12(110):20150486, 2015.

[81] Karol Miller and Kiyoyuki Chinzei. Mechanical properties of brain tissue in tension. *Journal of Biomechanics*, 35(4):483–490, 2002.

[82] Yekaterina A Miroshnikova, Janna K Mouw, J Matthew Barnes, Michael W Pickup, Johnathan N Lakins, Youngmi Kim, Khadjia Lobo, Anders I Persson, Gerald F Reis, Tracy R McKnight, et al. Tissue mechanics promote IDH1-dependent HIF1α–tenascin C feedback to regulate glioblastoma aggression. *Nature Cell Biology*, 18(12):1336–1345, 2016.

[83] Parisa Mosayebi, Dana Cobzas, Albert Murtha, and Martin Jagersand. Tumor invasion margin on the Riemannian space of brain fibers. *Medical Image Analysis*, 16(2):361–373, 2012.

[84] Raymond William Ogden. Large deformation isotropic elasticity–on the correlation of theory and experiment for incompressible rubberlike solids. *Proceedings of the Royal Society of London. A. Mathematical and Physical Sciences*, 326(1567):565–584, 1972.

[85] J.M. Osborne and D.V. Zenkov. Steering the Chaplygin sleigh by a moving mass. In *Proceedings of the 44th IEEE Conference on Decision and Control*, pages 1114–1118. IEEE, 2005.

[86] K.J. Painter. Modelling migration strategies in the extracellular matrix. *Journal of Mathematical Biology*, 58:511–543, 2009.

[87] KJ Painter and Thomas Hillen. Mathematical modelling of glioma growth: the use of diffusion tensor imaging (DTI) data to predict the anisotropic pathways of cancer invasion. *Journal of Theoretical Biology*, 323:25–39, 2013.

[88] Kay M Pepin and Kiaran P McGee. Quantifying tumor stiffness with magnetic resonance elastography: The role of mechanical properties for detection, characterization, and treatment stratification in oncology. *Topics in Magnetic Resonance Imaging*, 27(5):353–362, 2018.

[89] Kay M Pepin, Kiaran Patrick McGee, Arvin Arani, David S Lake, Kevin J Glaser, Armando Manduca, Ian F Parney, Richard Lorne Ehman, and John Huston. MR elastography analysis of glioma stiffness and IDH1-mutation status. *American Journal of Neuroradiology*, 39(1):31–36, 2018.

[90] Katarzyna Pogoda, LiKang Chin, Penelope C Georges, FitzRoy J Byfield, Robert Bucki, Richard Kim, Michael Weaver, Rebecca G Wells, Cezary Marcinkiewicz, and Paul A Janmey. Compression stiffening of brain and its effect on mechanosensing by glioma cells. *New Journal of Physics*, 16(7):075002, 2014.

[91] Whitney B Pope and Garth Brandal. Conventional and advanced magnetic resonance imaging in patients with high-grade glioma. *The Quarterly Journal of Nuclear Medicine and Molecular Imaging*, 62(3):239, 2018.

[92] JP Posti, M Bori, T Kauko, M Sankinen, J Nordberg, M Rahi, J Frantzén, V Vuorinen, and JOT Sipilä. Presenting symptoms of glioma in adults. *Acta Neurologica Scandinavica*, 131(2):88–93, 2015.

[93] Michael T Prange and Susan S Margulies. Regional, directional, and age-dependent properties of the brain undergoing large deformation. *Journal of Biomechanical Engineering*, 124(2):244–252, 2002.

[94] Luigi Preziosi and Andrea Tosin. Multiphase modelling of tumour growth and extracellular matrix interaction: mathematical tools and applications. *Journal of Mathematical Biology*, 58:625–656, 2009.

[95] SJ Price, NG Burnet, Tim Donovan, HAL Green, Alonso Pena, NM Antoun, John D Pickard, T Adrian Carpenter, and JH Gillard. Diffusion tensor imaging of brain tumours at 3 T: a potential tool for assessing white matter tract invasion? *Clinical Radiology*, 58(6):455–462, 2003.

[96] Vakhtang Putkaradze and Stuart Rogers. On the dynamics of a rolling ball actuated by internal point masses. *Meccanica*, 53(15):3839–3868, 2018.

[97] Vakhtang Putkaradze and Stuart Rogers. On the optimal control of a rolling ball robot actuated by internal point masses. *Journal of Dynamic Systems, Measurement, and Control*, 142(5):051002, 2020.

[98] Daniela F Quail and Johanna A Joyce. The microenvironmental landscape of brain tumors. *Cancer Cell*, 31(3):326–341, 2017.

[99] Margarita Reséndiz. Towards a mechanical model for anisotropic glioma spread using Darcy's law. *bioRxiv*, 2021.

[100] M. Rhodes, V. Gzenda, and V. Putkaradze. Control and integrability in figure skating. *SIAM News*, 54(3), 2021.

[101] Meghan Rhodes. *Mechanical modelling of living systems: from cancer modelling to control in sports.* PhD thesis, University of Alberta, 2022.

[102] Meghan E Rhodes, Thomas Hillen, and Vakhtang Putkaradze. Comparing the effects of linear and one-term ogden elasticity in a model of glioblastoma invasion. *Brain Multiphysics*, page 100050, 2022.

[103] Meghan E Rhodes and Vakhtang Putkaradze. *Trajectory tracing in figure skating [Manuscript submitted for publication].* PhD thesis, University of Alberta, Edmonton AB, 2022.

[104] H. Risken. *The Fokker-Planck Equation, Methods of solution and Applications*. Springer-Verlag, Berlin, 1996.

[105] R. Rockne, J.K. Rockhill, M. Mrugala, A.M. Spence, I. Kalet, K. Hendrickson, A. Lai, T. Cloughesy, E.C. Alvord Jr, and K. Swanson. Predicting the efficacy of radiotherapy in individual glioblastoma patients *in vivo*: a mathematical modelling approach. *Physics in Medicine and Biology*, 55:3271–3285, 2010.

[106] R. Rosenberg. Why is ice so slippery. *Physics Today*, pages 50–55, 2005.

[107] Wojciech Sas, Katarzyna Gabryś, Alojzy Szymański, et al. Determination of Poisson's ratio by means of resonant column tests. *Electron. J. Pol. Agricu. Univ. EJPAU*, 16(03), 2013.

[108] K. Schaefer, N. Brown, and W. Alt. Mlssle-a new method to analyse performance parameters of figure skating jumps. In *ISBS-Conference Proceedings Archive*, 2016.

[109] Artemiy S Silantyev, Luca Falzone, Massimo Libra, Olga I Gurina, Karina Sh Kardashova, Taxiarchis K Nikolouzakis, Alexander E Nosyrev, Christopher W Sutton, Panayiotis D Mitsias, and Aristides Tsatsakis. Current and future trends on diagnosis and prognosis of glioblastoma: from molecular biology to proteomics. *Cells*, 8(8):863, 2019.

[110] M Simon, J Guo, S Papazoglou, H Scholand-Engler, C Erdmann, U Melchert, M Bonsanto, J Braun, D Petersen, I Sack, et al. Noninvasive characterization of intracranial tumors by magnetic resonance elastography. *New Journal of Physics*, 15(8):085024, 2013.

[111] José M Soares, Paulo Marques, Victor Alves, and Nuno Sousa. A hitchhiker's guide to diffusion tensor imaging. *Frontiers in Neuroscience*, 7:31, 2013.

[112] Magdalena A Stolarska, Yangjin Kim, and Hans G Othmer. Multiscale models of cell and tissue dynamics. *Philosophical Transactions of the Royal Society A: Mathematical, Physical and Engineering Sciences*, 367(1902):3525–3553, 2009.

[113] Kaspar-Josche Streitberger, Martin Reiss-Zimmermann, Florian Baptist Freimann, Simon Bayerl, Jing Guo, Felix Arlt, Jens Wuerfel, Jürgen Braun, Karl-Titus Hoffmann, and Ingolf Sack. High-resolution mechanical imaging of glioblastoma by multifrequency magnetic resonance elastography. *PloS ONE*, 9(10), 2014.

[114] Shashank Subramanian, Amir Gholami, and George Biros. Simulation of glioblastoma growth using a 3d multispecies tumor model with mass effect. *Journal of Mathematical Biology*, 79(3):941–967, 2019.

[115] Amanda Swan. *An Anisotropic Diffusion Model for Brain Tumour Spread*. PhD thesis, University of Alberta, Edmonton AB, 2016.

[116] Amanda Swan, Thomas Hillen, John C Bowman, and Albert D Murtha. A patient-specific anisotropic diffusion model for brain tumour spread. *Bulletin of Mathematical Biology*, 80(5):1259–1291, 2018.

[117] K.R. Swanson, C. Bridge, J.D. Murray, and E.C. Jr Alvord. Virtual and real brain tumors: using mathematical modeling to quantify glioma growth and invasion. *Journal of the Neurological Sciences*, 216:1–10, 2003.

[118] KR Swanson, RC Rostomily, and EC Alvord Jr. A mathematical modelling tool for predicting survival of individual patients following resection of glioblastoma: a proof of principle. *British Journal of Cancer*, 98(1):113–119, 2008.

[119] Kristin R Swanson, Ellsworth C Alvord Jr, and JD Murray. A quantitative model for differential motility of gliomas in grey and white matter. *Cell Proliferation*, 33(5):317–329, 2000.

[120] P. Tallapragada and V. Fedonyuk. Steering a Chaplygin sleigh using periodic impulses. *Journal of Computational and Nonlinear Dynamics*, 12(5), 2017.

[121] P Tracqui, GC Cruywagen, DE Woodward, GT Bartoo, JD Murray, and EC Alvord Jr. A mathematical model of glioma growth: the effect of chemotherapy on spatio-temporal growth. *Cell Proliferation*, 28(1):17–31, 1995.

[122] Theresa A Ulrich, Elena M de Juan Pardo, and Sanjay Kumar. The mechanical rigidity of the extracellular matrix regulates the structure, motility, and proliferation of glioma cells. *Cancer Research*, 69(10):4167–4174, 2009.

[123] JAW Van Dommelen, M Hrapko, and GWM Peters. Mechanical properties of brain tissue: characterisation and constitutive modelling. In *Mechanosensitivity of the Nervous System*, pages 249–279. Springer, 2009.

[124] Chrysovalantis Voutouri, Fotios Mpekris, Panagiotis Papageorgis, Andreani D Odysseos, and Triantafyllos Stylianopoulos. Role of constitutive behavior and tumor-host mechanical interactions in the state of stress and growth of solid tumors. *PLoS ONE*, 9(8):e104717, 2014.

[125] Xiang-Sheng Wang, Haiyan Wang, and Jianhong Wu. Traveling waves of diffusive predator-prey systems: disease outbreak propagation. *Discrete & Continuous Dynamical Systems-A*, 32(9):3303–3324, 2012.

[126] DE Woodward, J Cook, P Tracqui, GC Cruywagen, JD Murray, and EC Alvord Jr. A mathematical model of glioma growth: the effect of extent of surgical resection. *Cell Proliferation*, 29(6):269–288, 1996.

[127] Qian Xie, Sandeep Mittal, and Michael E Berens. Targeting adaptive glioblastoma: an overview of proliferation and invasion. *Neuro-oncology*, 16(12):1575–1584, 2014.

[128] H Youssefpour, X Li, A D Lander, and J S Lowengrub. Multispecies model of cell lineages and feedback control in solid tumors. *Journal of Theoretical Biology*, 304:39–59, 2012.

[129] D. V. Zenkov. Linear conservation laws of nonholonomic systems with symmetry. *Discrete and Continuous Dynamical Systems (extended volume)*, pages 963–972, 2003.